Author: Pedro Martín Mateos
Supervisor: Pablo Acedo Gallardo

New Spectroscopic Techniques and Architectures for Environmental and Biomedical Applications

PhD Dissertation

Universidad Carlos III de Madrid
September 2015

UNIVERSIDAD CARLOS III DE MADRID

Departamento de Tecnología Electrónica

TESIS DOCTORAL

NEW SPECTROSCOPIC TECHNIQUES AND ARCHITECTURES FOR ENVIRONMENTAL AND BIOMEDICAL APPLICATIONS

Autor: PEDRO MARTÍN MATEOS

Director: PABLO ACEDO GALLARDO

Leganés, Septiembre 2015

NEW SPECTROSCOPIC TECHNIQUES AND ARCHITECTURES FOR ENVIRONMENTAL AND BIOMEDICAL APPLICATIONS

Autor: PEDRO MARTÍN MATEOS

Director: PABLO ACEDO GALLARDO

Firma del Tribunal Calificador:

Firma

Presidente:

Vocal:

Secretario:

Calificación:

Leganés, de de

CONTENTS

ABSTRACT

The range of application of spectroscopic instruments is so broad nowadays that encompasses various areas of engineering, industry and scientific research. Consequently, different techniques and spectral analysis methods have been developed for the characterization of the numerous samples regularly targeted by spectroscopic sensors. In this doctoral dissertation, contributions have been made to virtually all of the main components that make up spectroscopic systems.

Different methods, architectures and spectral data analysis algorithms have been proposed for environmental and biomedical applications particularly. In this way, novel techniques and architectures for molecular spectroscopy based on the measurement of optical dispersion have been presented (unlike most of the current methods that are based on the measurement of absorption). This approach, whereas maintain a reasonably low level of complexity, overcomes most of the limitations associated to absorption-based methods, providing an improved performance in some areas of the analyzers. Even though two of the proposed architectures for the estimation of gas concentration are based on the use of tunable lasers for the characterization of the spectral profile of the sample in the vicinity of an absorption feature, the best performances have been obtained using a dual-comb source. In fact, the development of new robust architectures for dual-comb spectrometers based on combs synthetized by the modulation of continuous wave lasers has been one of the main lines of work of this thesis. Although having a narrower spectral coverage than traditional combs, these sources provide far lower costs and complexity and the robustness of the generators is far higher. Most of the efforts have been made towards the developments of the new dual-comb architectures that allow to take advantage of the use comb-based systems out of the metrology laboratory. Finally, contributions on the integration of complete spectroscopic instrumentation systems, including spectral analysis techniques based on Blind Signal Separation have been made. For that, a non-invasive biomedical spectroscopic instrument has been developed and used as a benchmark to study the viability of diffuse spectroscopic methods and spectral data classification techniques in the monitoring of the state of angiogenesis of a bioengineered skin substitute.

RESUMEN

El ámbito de aplicación de la instrumentación basada en espectroscopía es tan amplio que abarca áreas de ingeniería, de la industrial y de investigación científica. De este modo, diferentes técnicas espectroscópicas y de análisis espectral han sido desarrolladas para la caracterización y medida de los numerosos objetivos que son habitualmente estudiados por sensores espectroscópicos. En esta tesis doctoral, se han realizado contribuciones en, prácticamente, todos los bloques constituyentes de un sistema de espectroscopía.

Distintas técnicas, arquitecturas y algoritmos de análisis espectral han sido propuestos, principalmente, para aplicaciones ambientales y biomédicas. Han sido presentadas nuevas técnicas y arquitecturas para espectroscopía molecular basadas en la medida de la dispersión óptica, a diferencia de la gran mayoría de los sensores actuales que basan su funcionamiento en la medida de absorción. Esta aproximación mantiene unos niveles de complejidad de implementación razonablemente reducidos; a la vez que, soluciona la mayoría de limitaciones asociadas con los métodos basados en absorción óptica; proporcionando, además, mejores prestaciones en muchas de las áreas de funcionamiento de los analizadores moleculares. Aunque algunas de las arquitecturas que se proponen en esta tesis están basadas en la utilización de diodos sintonizables en frecuencia para la caracterización del perfil espectral de gases en las inmediaciones de transiciones moleculares, los mejores resultados se han obtenido con la utilización de fuentes duales de peines de frecuencias ópticas (dual-OFCs). De hecho, el desarrollo de arquitecturas robustas para espectrómetros basados en dual-OFCs, generados a partir de la modulación de un láser de onda continua ha sido una de las líneas principales de investigación de esta tesis. Aunque presentan una menor cobertura espectral, estas fuentes ópticas poseen niveles mucho más reducidos de coste y complejidad que los esquemas clásicos, proporcionando una gran robustez. Los principales esfuerzos de este trabajo se han dirigido a aprovechar dicha robustez para el desarrollo de nuevas arquitecturas, que permitan aprovechar las características de los peines de frecuencias ópticas en sensores desplegables fuera de un laboratorio de metrología. Del mismo modo, se han realizado contribuciones en la integración de sistemas de instrumentación espectroscópica, incluyendo técnicas de análisis espectral basadas en Separación Ciega de Fuentes. Por ello, un instrumento espectroscópico no invasivo ha sido desarrollado para ser utilizado como banco de pruebas en un estudio de la viabilidad de la utilización de métodos de espectroscopía

difusa y de clasificación de datos espectrales para la monitorización del estado de angiogénesis de injertos de piel artificial.

LIST OF CONTRIBUTIONS

PAPER [A]: **P. Martín-Mateos** and P. Acedo, "Heterodyne phase-sensitive detection for calibration-free molecular dispersion spectroscopy," Opt. Express **22**(12), 15143–15153 (2014).

PAPER [B]: **P. Martín-Mateos**, B. Jerez, and P. Acedo, "Heterodyne architecture for tunable laser chirped dispersion spectroscopy using optical processing," Opt. Lett. **39**(10), 2611–2613 (2014).

PAPER [C]: **P. Martín-Mateos**, B. Jerez, and P. Acedo, "Dual electro-optic optical frequency combs for multiheterodyne molecular dispersion spectroscopy," Opt. Express **23**(16), 21149-21158 (2015).

PAPER [D]: **P. Martin-Mateos**, M. Ruiz-Llata, J. Posada-Roman, and P. Acedo, "Dual Comb Architecture for Fast Spectroscopic Measurements and Spectral Characterization," IEEE Photonics Technol. Lett. **27**(12), 1309–1312 (2015).

PAPER [E]: **P. Martín-Mateos**, S. Crespo-Garcia, M. Ruiz-Llata, J. R. Lopez-Fernandez, J. L. Jorcano, M. Del Rio, F. Larcher, and P. Acedo, "Remote diffuse reflectance spectroscopy sensor for tissue engineering monitoring based on blind signal separation," Biomed. Opt. Express **5**(9), 3231-3237 (2014).

OTHER CONTRIBUTIONS

JOURNAL PAPERS

1. M. Ruiz-Llata, **P. Martín-Mateos**, J. R. López, and P. Acedo, "Remote optical sensor for real-time residual salt monitoring on road surfaces," Sensors Actuators B Chem. **191**, 371–376 (2014).

CONFERENCE CONTRIBUTIONS

2. **P. Martín-Mateos**, S. Crespo-Garcia, M. Ruiz-Llata, J. R. Lopez-Fernandez, J. L. Jorcano, M. Del Rio, F. Larcher, and P. Acedo, "Portable, Non-contact, Diffuse Reflectance Spectroscopy System for Early Skin Implants Assessment," in Biomedical Optics 2014, OSA Technical Digest (online) (Optical Society of America, 2014), paper BS3A.40.

3. D. Duda, **P. Martin-Mateos**, B. Jerez, M. Ruiz-Llata, and P. Acedo, "Optical gas sensor based on an Android application for real-time, reconfigurable spectroscopic data analysis," in IEEE SENSORS 2014 Proceedings, 1054–1056 (2014).

4. J. A. Garcia-Souto, **P. Martin-Mateos**, J. E. Posada, P. Acedo, and D. A. Jackson, "Evaluation of a 1540nm VCSEL for fibre Bragg gratings interrogation in dynamic measurement applications," in OFS2014 23rd International Conference on Optical Fiber Sensors, 91573A (2014).

5. O. E. Bonilla-Manrique, J. A. Garcia-Souto, **P. Martín-Mateos**, B. Jerez and P. Acedo, "Fast Interrogation of Fiber Bragg Grating Sensors using Electro-optic Dual Optical Frequency Combs" in OFS2015 24rd International Conference on Optical Fiber Sensors, (2015).

LIST OF ACRONYMS

ADC	Analog to Digital Converter
BSS	Blind Signal Separation
CLaDS	Chirped Laser Dispersion Spectroscopy
CORDIC	Coordinate Rotation Digital Computer
DAC	Digital to Analog Converter
DDS	Direct Digital Synthesizer
DLAS	Direct Laser Absorption Spectroscopy
DRS	Diffuse Reflectance Spectroscopy
DSP	Digital Signal Processors
DUT	Device Under Test
FM	Frequency Modulation
FMS	Frequency Modulation Spectroscopy
FPGA	Field Programmable Gate Array
FT-IR	Fourier Transform Infrared spectroscopy
FWHM	Full Width at Half Maximum
GUI	Graphic Unit Interface
HITRAN	High-Resolution Transmission molecular absorption database
HMI	Human Machine Interface
HPSDS	Heterodyne Phase-Sensitive Dispersion Spectroscopy

ICA	Independent Component Analysis
LED	Light Emitting Diode
MC	Monte-Carlo
NICE-OHMS	Noise-Inmune Cavity-Enhanced Optical Heterodyne Molecular Spectroscopy
NIR	Near-Infrared
OFC	Optical Frequency Comb
OFCG	Optical Frequency Comb Generator
PCA	Principal Component Analysis
PCB	Printed Circuit Board
PDE	Photon Diffusion Equation
PLS	Partial Least Square
RTE	Radiation Transport Equation
SNR	Signal-to- Noise Ratio
TDLS	Tunable Diode Laser Spectroscopy
TT-FMS	Two-Tone Frequency Modulation Spectroscopy
VCSEL	Vertical-Cavity Surface-Emitting Laser
VEGF	Vascular Endothelial Growth Factor
WMS	Wavelength Modulation Spectroscopy

1. Introduction

1.1 OPTICAL SPECTROSCOPIC SYSTEMS

Optical spectroscopy studies the dependency with the wavelength of various phenomena associated to the interaction between matter and light (like absorption, dispersion or scattering). Even though other schemes have been presented, this dissertation is focused on the study of active spectroscopic techniques for spectral interrogation in which the light source is a part of the spectroscopic system. Thus, these instruments measure the optical spectrum resulting from the propagation (or the reflection) of the light emitted by an optical source through an optical medium. Nevertheless, the desired result of the system is not generally the spectral data themselves, but the composition or the concentration of constituents in the medium and, therefore, further processing, modelling, calibration or classification methods have to be used in order to obtain a final instrument.

There are numerous spectroscopic techniques, some better suited than others, for targeting particular components and optical media. Therefore, illumination and detection schemes vary accordingly from the simplest spectroscopic architectures for directly measuring the fraction of optical intensity reflected from a surface or transmitted through a medium, to the more complex approaches based on modulated optical sources or Raman detection. The basic block diagram of an active spectroscopic system is shown in Fig. 1-1 in which a differentiation is made between the spectroscopic technique and the methods for signal processing, spectral analysis and information extraction.

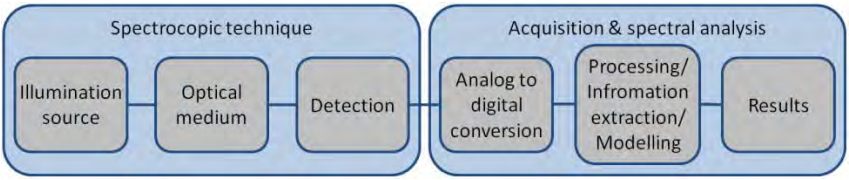

Fig. 1-1. Basic block diagram of a spectroscopic system.

There exist different options in terms of the sources to use in an optical system, from the narrow lines of lasers to broadband emitters like the classical Tungsten-Halogen lamps or solid state Light Emitting Diodes (LED). While the first ones stand out by its high spectral intensity densities and extremely small bandwidths, broadband optical sources have a broad spectrum that allows to measure the optical characteristics of a medium in a wide range of frequencies simultaneously. A different broadband emitter is the recently emerged Optical Frequency Comb (OFC) that provides an optical spectrum which (in some implementations) has thousands of equidistant narrow linewidth tones spread over a range wider than an octave [1,2]. Even though an OFC is an optical source that combines the positive features of both lasers and broadband emitters, the complexity of implementation and cost of these sources is nowadays far higher than those of other emitters, and its use out of the metrology laboratory is still very challenging.

Even though multi-source laser spectroscopic sensors can characterize different spectral points in a range only restricted by the complexity of the sensor and the wavelengths of emission of the devices, lasers are more often employed in the measurement of narrow spectral features in which their tunability possibilities are exploited (as presented in section 1.3). In this way, the frequency of the source is swept over the spectral range of interest while a photodetector measures the wavelength dependent optical intensity or phase shift. On the other hand, broadband emitters are the preferred option for instruments that must cover a wide spectral range; these sources nonetheless need a spectral detection method to separate the different frequency components of the optical signal. These methods will be also covered in section 1.3.

The spectroscopic technique (Fig. 1-1) provides therefore a measurement of the optical spectrum that has been influenced by the optical medium. Nonetheless, this measurement must be further processed to extract the information of interest for the instrument (concentration of analytes in the medium for example). The first step of this procedure is the acquisition (digitization) of the signal that is made by an analog to digital converter. The subsequent digital processing is tightly related to the spectroscopic method employed. Therefore, for certain architectures it is necessary to identify the absorption peak, while in others systems a Fourier transformation or a synchronous detection must be performed. The spectral measurement is also generally affected by problems like the baseline, variations in the optical intensity of the source, or ethalon fringes that must

be addressed. The last step in the process is known as calibration and consists on providing an assessment of the concentration of analytes. This task is reasonably simple in the case of targeting single species, but becomes more and more complex with the increasing amount of analytes in multi-species scenarios. The performance yielded in this situation by classical information extraction or light propagation modeling methods is very often limited by the complexity of the optical media, and therefore data classification algorithms are usually employed. These classification methods have been developed for the identification and quantification of the contributions of the analytes that are present in the medium and are reviewed in more depth in chapter 4.

The results obtained by the procedures described in the previous paragraphs are the final output of the spectroscopic instrument. This output is usually the concentration or identification of spectral contributors in the medium, but it can also be the temperature, the pressure, the rate of movement or any other parameter of the target. Even though this set of procedures can be "manually" performed in the first demonstrations of a technique or a spectroscopic architecture, the obtaining of a deployable self-contained spectroscopic instrument requires incorporating all of the tasks associated to the different steps during the integration phase. These tasks go from the control of the spectroscopic sensor by a processor, to the acquisition and digital processing of the optical spectrum, the visualization of results or the implementation of the user interface.

Complementing the information given in Fig. 1-1, in the next sections different aspects of a spectroscopic system will be reviewed in more depth. This analysis starts with a description of the properties of optical media in which differentiation is made between non-scattering and scattering optical media. Then, several spectroscopic techniques classified as a function of the width of the spectral feature that are designed to target are presented. As it was previously said, the end result of spectroscopic instrument is not generally the optical spectrum, but the composition or the concentration of constituents in the medium, thus in section 1.4 the main consideration and procedures for spectral analysis are presented. After detailing the different components of the sensor, several aspects of system integration for spectroscopic instruments are covered. Finally, the objectives and organization of this PhD dissertation are presented.

1.2 CHARACTERISTICS OF OPTICAL MEDIA

1.2.1 Non-scattering optical media

In any optical medium in which propagation is mainly determined by absorption and the optical intensity is small enough to not introduce non-linear behaviors, the propagation of light is well determined by the complex index of refraction. An optical signal can be represented as:

$$E = E_0 e^{i(\omega t - kz)} \tag{1-1}$$

where E is the optical electric field, E_0 the amplitude, ω is the angular frequency, t the time, k the wavenumber and z the direction of propagation. When this electro-magnetic wave travels through an optical medium with a complex refractive index given by:

$$n = n' - i\frac{\alpha}{2k_0} \tag{1-2}$$

the amplitude of the resulting optical wave is attenuated (α is the absorption coefficient) and its wavenumber increased ($n' \geq 1$):

$$E = E_0 e^{-\frac{\alpha}{2}z} e^{i(\omega t - n'kz)} \tag{1-3}$$

The wavelength λ ($k = 2\pi/\lambda$) is therefore reduced and so it is the speed of propagation (phase velocity) of the signal. Moreover, both the real and imaginary parts of the complex refractive index are frequency dependent and therefore absorption as well as the speed of propagation are a function of the frequency of the optical signal travelling through the medium.

It is possible to analytically obtain the complex index of refraction of a spectral line of a gaseous media at sufficiently low pressure (considering the interaction between molecules negligible) assuming that the model of a damped oscillator represents the behavior of isolated atoms and molecules. The expressions obtained in this way for the real and complex parts of the index of refraction are known as the Kramers-Kronig equations [3,4]. These relations, that are given in Eq. (1-4) and (1-5), were derived independently

by Hendrik Anthony Kramers and Ralph de Laer Kronig in 1926 and 1927 respectively and allow to obtain the refractive index profile from the wavelength dependent absorption coefficient and vice versa.

$$n'(\omega) = 1 + \frac{Nq^2}{2\epsilon_0 m} \frac{\omega_0^2 - \omega^2}{(\omega_0^2 - \omega^2)^2 - \omega^2\gamma^2} \tag{1-4}$$

$$\alpha(\omega) = \frac{Nq^2\omega_0}{c\epsilon_0 m} \frac{\omega\gamma}{(\omega_0^2 - \omega^2)^2 - \omega^2\gamma^2} \tag{1-5}$$

where N is the number of oscillators (molecules) per unit volume, q the charge under the influence of the electric field of the optical wave, ω_0 the resonant frequency of the oscillator and γ the oscillator linewidth. As shown then by the Kramers-Kronig relations, frequency dependent refractive index variations are as inherent to molecular or atomic absorption lines as absorption itself. As a reference, the profiles of the absorption coefficient and the refractive index of a gaseous medium in the vicinity of a molecular transition of center λ_c are plotted in Fig. 1-2.

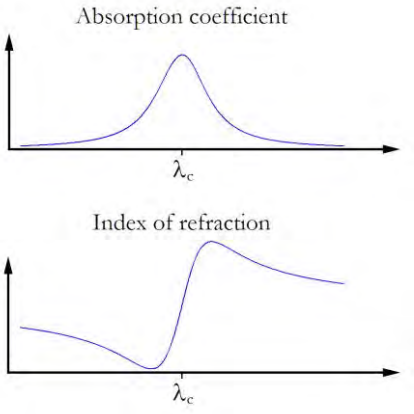

Fig. 1-2. Profiles of the absorption coefficient and the index of refraction in the vicinity of a molecular transition with center λ_c.

It is well known that molecules have multiple resonances that are related to vibrational and rotational modes (in the NIR) with particular fixed frequencies that are characteristics of the structure of the molecule. As an example, the frequency dependent absorption coefficient of ammonia is shown in Fig. 1-3. The absorption profile is the result of the contribution of the overlapping of the different resonances of the molecule. This frequency dependency of the absorption and dispersion spectrum of gases allows spectroscopic instruments to perform species identification. In the same way, as shown by Eqs. (1-4) and (1-5), both absorption and dispersion are related to the concentration of molecules (oscillators) per volume area and this enables the estimation of concentration.

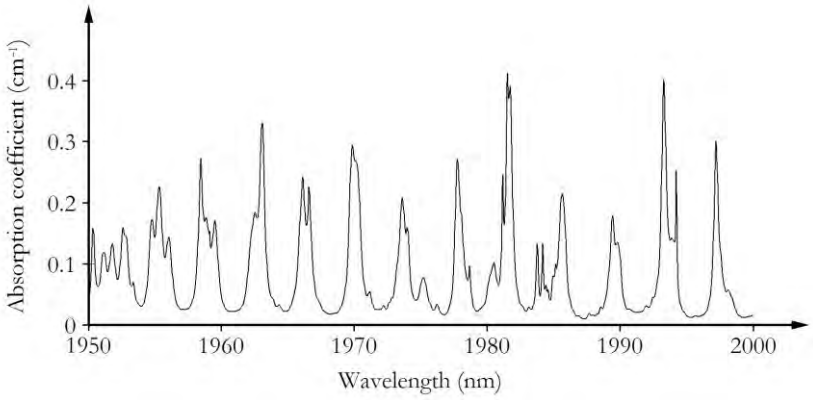

Fig. 1-3. Absorption coefficient of ammonia as a function of the wavelength. [5]

The absorption and dispersion spectra of gases are reasonably simple, being composed of several groups of spectral features that overlap forming lines of absorption and dispersion. The position of these lines is characteristic of the molecule under study, and the amount of attenuation or optical dispersion is directly related to the concentration of gas. It must be noted that the relationship between the attenuation and the concentration is exponential (Beer-Lambert law) whereas dispersion and concentration are linearly related.

As a difference with gases, the much narrower distances between atoms or molecules in solid and liquids induce stronger interactions that results in the broadening of the spectral features. Whereas the transitions of

the molecules in liquid or solid phase form wide spectral features of tens of nanometers in width, the widths of the absorptions lines of molecules in gaseous state are three orders of magnitude narrower, in the region of a few tens of picometers (several GHz). A comparison between the spectral characteristics of liquid water and water vapor is shown in Fig. 1-4 for reference. The broadening of the spectral features and the effects of inter-molecule interactions are evident. It is worthwhile to note that the absorption coefficient of water vapor has been multiplied by 100 for viewing purposes.

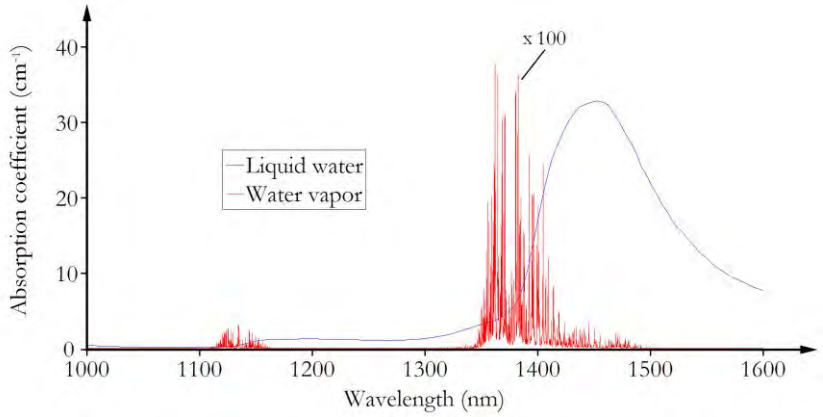

Fig. 1-4. Absorption coefficient of liquid water and water vapor [5] in the 1000 nm to 1600 nm range. The absorption coefficient of water vapor has been zoomed in 100 times.

As it has been previously said, and as happens with the absorption coefficient, the index of refraction of a liquid or solid sample is also (as implied by the Kramers-Kronig relations) frequency dependent, and this causes electro-magnetic waves to travel at different speeds though the medium. One of the most representative examples of the effects of dispersion in solid optical media is the behavior of optical fibers. For illustration purposes, the absorption spectrum of an optical fiber is shown in Fig. 1-5 (where the attenuation profile is given by factors like light scattering on material inhomogeneities or losses due to hydroxyl ions) and the dispersion profile is shown in Fig. 1-6.

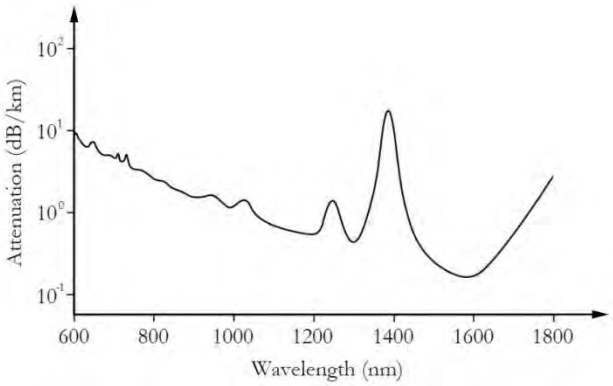

Fig. 1-5. Attenuation of an optical fiber as a function of the wavelength.

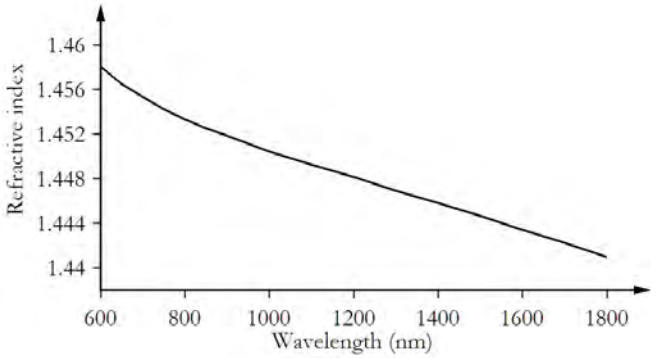

Fig. 1-6. Refractive index profile of and optical fiber as a function of the wavelength.

Getting back to the block diagram of Fig. 1-1, it now becomes clear why broadband emitters or multiple sources are normally chosen for the characterization of the wider spectral components of liquids and solids, and tunable lasers are usually used for gas analysis and monitoring. The differences between the optical sources make mandatory the use of different detection schemes. For example, while a simple measurement of intensity can be used for the detection of a tunable laser, some type of spectral interrogation method (like a spectrometer) must be employed to analyze the optical spectrum of a broadband emitter. These different illumination and detection approaches are reviewed in section 1.3

The spectral features and spectroscopic methods have also an influence in the spectral analysis to perform for the extraction of information. The wider spectral features of liquids and solids make more complex the identification of the analyte because of the stronger similarities between different components. In these media, instead of the narrow spectral features concentrated around rotational transitions of the molecules of gases, there is a continuum level of absorption with much wider peaks. This is reflected in the difficulties to separate the contribution of different molecules in the common situation of complex optical media with multiple components. Therefore, this task is very often accomplished by taking advantage of data classification algorithms.

1.2.2 Scattering optical media

As a difference with the absorption limited propagation of light in molecular samples (and in non-scattering samples in general), the propagation of light in what are known as turbid media is mainly defined by scattering. Typical examples of turbid media are biological tissues, that will be the target of the spectroscopic instrument and the spectral processing techniques presented in the fourth chapter of this dissertation. Therefore, even though absorption is strongly present in biological samples, the propagation of light in tissues is mainly determined by scattering events. The particularities of this type of propagation and its influence on spectroscopic techniques are reviewed in this section.

The propagation of light in turbid media is determined by two wavelength dependent parameters, the absorption and the scattering coefficients. The absorption coefficient $\mu_a(\lambda)$ is defined here as the inverse of the average distance travelled by a photon through the medium before it gets absorbed (absorption length). In the same way, the scattering coefficient $\mu_s(\lambda)$ is the inverse of the average distance travelled by a photon through the tissue before it is scattered, that is equal to the inverse of the scattering length. Nevertheless, the scattering coefficient is corrected depending on the average angular distribution of the scattering events resulting in the reduced scattering coefficient $\mu_s'(\lambda)$:

$$\mu_s'(\lambda) = (1 - g)\,\mu_s(\lambda) \tag{1-6}$$

where g is the anisotropy factor that is equal to the average of the cosine of the scattering angle.

Then, it is possible to define the transport coefficient $\mu_t'(\lambda)$

$$\mu_t'(\lambda) = \mu_s'(\lambda) + \mu_a(\lambda) \tag{1-7}$$

that is equal to the inverse of the transport mean free path, defined as the average distance travelled by a photon through the turbid medium before its direction is randomized.

In the example of biological tissues, cells, cell organelles and collagen are responsible for scattering, whereas hemoglobin, melanin, lipid and water are responsible for absorption. Given that the absorption spectrum of these chromophores is well-known, if the effects of absorption and scattering in the back reflected optical spectrum are separated, it is possible to assess the concentrations of each one of the tissue components [6]. As an example, in Fig. 1-7 the absorption spectrum of fully oxygenated and fully deoxygenated blood is shown.

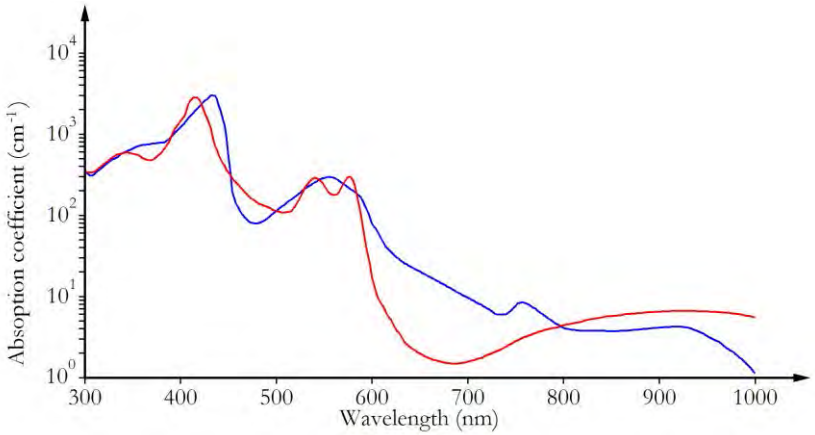

Fig. 1-7. Absorption coefficient as a function of the wavelength of fully oxygenated (red) and fully deoxygenated (blue) blood.

From the analytical point of view, the separation between of absorption and scattering can be performed by the diffusion transport model. Even though the Radiation Transport Equation (RTE) [7] provides the basis for the separation, the complexity of this identity makes that a solution can only be numerically computed (with the exception of extraordinarily simple examples). Nevertheless, it is possible to derive the much simpler Photon Diffusion Equation (PDE) from the RTE taking advantage of several assumptions. For the PDE to accurately approximate the RTE, $\mu_s'(\lambda)$ must be much higher than μ_a and the distance travelled by photons in the tissue much larger than the transport mean free path previously defined. A generally accepted limit is that the distance travelled by the photon must be at least ten times larger than the transport mean free path. There are different reviews and texts in which these analytical models and the different procedures to derive the PDE are covered [6,8].

The PDE sets the mathematical means for the description of the propagation of light as a function of the optical properties of the turbid medium. Thus, in a medium with well characterized optical coefficients, the PDE can be solved for certain boundary conditions to yield the intensity of light diffusely back reflected from the tissue as a function of the wavelength. These results are known as the solution to the forward problem, i.e. the obtaining of the back scattered spectrum from the optical characteristics (μ_s' and μ_a) of the sample.

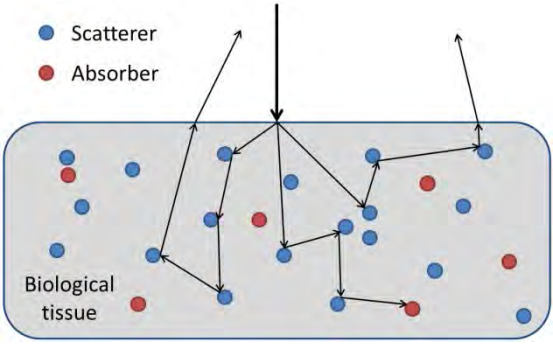

Fig. 1-8. Representation of the propagation of photons in biological tissues.

If the conditions for the accurate approximation of the RTE are fulfilled, the analysis of the physical meaning of the PDE provides a very descriptive picture of the propagation of light in biological tissues that is represented in Fig. 1-8. Photons travel through tissues in straight line

segments of an average length equal to the transport mean free path. After one segment is completed, the photon is either absorbed, and the energy thermally dissipated, or scattered with random direction. This process is repeated over and over again until the photon escapes from the tissue or it is absorbed by a chromophore.

As happened in the case of the analysis of non-scattering liquid and solid media, there is an overlapping between the wide spectral features of the components of biological tissues (clearly shown in Fig. 1-7). Therefore, the estimation of the concentration of a certain analyte is very often so complex that there are no analytical expressions or modeling methods capable of performing this assessment with high accuracy. Therefore, this task must be accomplished by taking advantage of data classifications algorithms that quantify the contributions of the various components of the tissue. As it was previously said, these spectral analysis techniques are reviewed in more depth in section 1.4.

1.3 INTRODUCTION TO SPECTROSCOPIC TECHNIQUES

In an active spectroscopic instrument it is possible to distinguish between the illumination scheme (associated to an optical source) and the detection technique. Many spectroscopic measurement approaches have been proposed and developed over the years to address different problems, and some of the most widely extended techniques are presented in this section. A differentiation is made between methods developed to target narrow spectral features and those devised for wide range spectral characterization.

1.3.1 Narrow-band spectroscopic methods

The development of narrow-band spectroscopic methods is tied closely to the evolution of molecular gas analyzers. Since the main characteristic of a molecular transition line is its narrow width (tens of pm), different architectures designed to optimize the measurement of these features have been proposed. As could not be otherwise given the high

density of power of near-monochromatic sources in comparison with broadband emitters, tunable lasers (especially diode lasers) are the light source in which these techniques are based on. These methods can be group together in what it is known as Tunable Diode Laser Spectroscopy (TDLS) techniques. The tunability of diode lasers allows to sweep the spectral feature of interest by controlling the temperature of operation and/or the injection current, whereas the high intensity increase the sensitivity of the sensor in relation to other light sources. For illustration, the tunability characteristics of a Vertical-Cavity Surface-Emitting Laser (VCSEL) are shown in Fig. 1-9 for different forward currents [9]. Moreover, new architectures are being developed with tuning ranges of more than 100 nm [10].

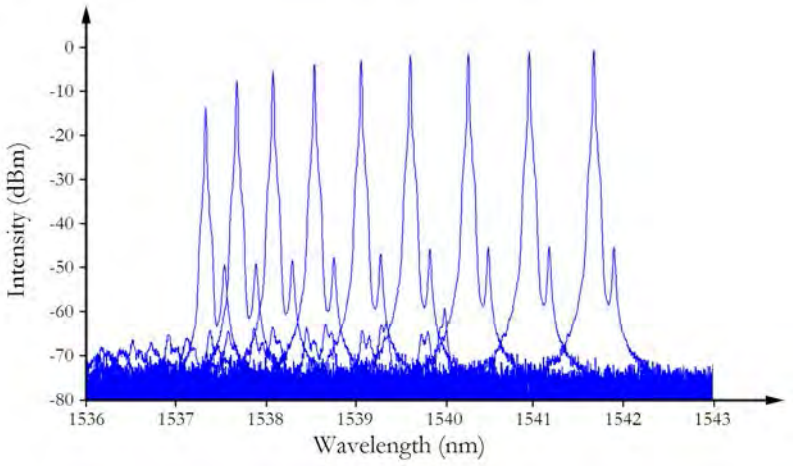

Fig. 1-9. Optical spectrum of a VCSEL for different injection currents [9].

TDLS methods are presented in the next paragraphs starting with absorption based approaches and then presenting molecular dispersion spectroscopic methods.

The most basic TDLS technique is known as Direct Laser Absorption Spectroscopy (DLAS) [11–13]. The power transmitted through a medium is measured while the laser is swept over a spectral feature to calculate the absorbance of the medium. In this way it is possible to estimate the concentration of a gas from the absorption coefficient. Multi-species

detection is viable if absorption features of different molecules are swept. Nevertheless, DLAS present several limiting issues. The first one is that the sensitivity of the sensor is highly limited by a high DC level, what it is known as the baseline problem. In absence of absorbing molecules, the power transmitted through the gas sample is maximum, and increasing analytes concentrations exponentially decrease this maximum level. The difficulty to measure small signal variations over high DC levels limits the sensitivity of the systems and, on top of that, this sensitivity is also deteriorated by the influence of Flicker and shot noise [14]. Besides this, the level of signal reaching the photodiode out of the spectral line needs to be accurately measured to be used as a normalization factor of the decrease in power produced by the gas molecules. This is essential to obtain an estimation of the concentration that is immune to fluctuations in the transmitted power that can be produced by many factors, from pointing instabilities, to atmospheric turbulences and weather phenomena. The sensitivity problem of DLAS can be mitigated using techniques based on modulation methods, greatly improving the sensitivity of gas detectors.

Wavelength Modulation Spectroscopy (WMS) [15,16] takes advantage of the slow modulation of the wavelength of emission of a laser. In the widely extended case of using laser diodes for WMS systems (and even though it brings associated also the modulation of the output power) the wavelength modulation is generated by modulating the injection current of the laser. It is important to note that there is an optimum wavelength modulation amplitude that maximizes the output signal [17], this point is mainly dependent on the linewidth, but also on the line shape. At atmospheric pressure, collisions between molecules broaden the otherwise Doppler profile of spectral lines in what is known as collisional or pressure broadening. In this situation, the line shape profile is generally accepted as Lorentzian [18]. Then, for Lorentzian spectral lines the optimum modulation wavelength amplitude is equal to 2.2 times the linewidth of the spectral feature, and in the case of Doppler profiles the optimum point becomes 2.1 times. These figures are given for what is known as 2f detection operation, in which the power transmitted through the sample is detected at the second harmonic of the wavelength modulation frequency. Hence, the output signal (the amplitude of the 2f harmonic) is only different from cero when a spectral feature distorts the wavelength modulated monochromatic light. Therefore, this approach provides the benefit of eliminating the baseline problem, one of the main issues of DLAS. Apart from that, since the signal is shifted to a relatively high frequency, the signal to noise ratio is in the same way improved (an interesting study related to

this point can be found in Ref. [14]). Nevertheless, WMS do not solve the problem of power normalization and hence, the output signal will get bigger in value if the power transmitted through the gas gets bigger and vice versa.

A good comparison between DLAS and WMS is made in a recent optical gas sensing review article by Hodgkinson and Tatam [19]. One of the illustrations of this paper (Fig. 33) is reproduced in Fig. 1-10 in which the differences between the implementations of both techniques are shown. The baseline problem of DLAS is well represented in the output signal of Fig. 1-10 (a) being possible to see the DC level that must be compensated for the estimation of concentration. WMS (Fig. 1-10 (b)) solve this problem by modulating the wavelength of the laser and detecting at the second harmonic of the modulation frequency; therefore, the 2f-WMS output signal has the shape of the derivative of the absorption line and presents no baseline.

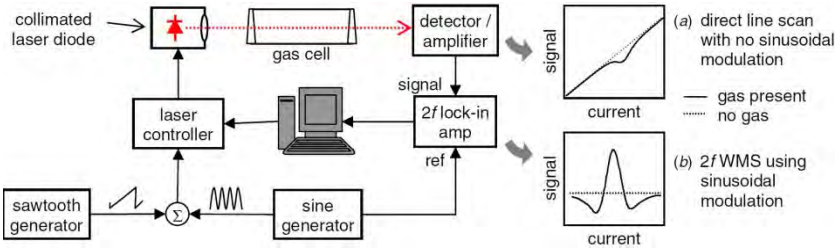

Fig. 1-10. Comparison between the conventional setups of DLAS and WMS. The output signals of (a) DLAS and (b) 2f-WMS are also shown. Figure has been extracted from Ref. [19].

On a very similar modulation oriented concept to that of WMS, Frequency Modulation Spectroscopy (FMS) [20–23] also allows to measure the transmission spectrum of an optical medium. FMS utilizes a high speed phase modulator to generate an optical signal in which the wavelength modulation deviation is greater than the linewidth of the spectral features. Ideally, only phase modulation is performed, so a photodiode located after the gas sample will measure a constant level of optical power that is independent of the emission wavelength. This is strictly true unless the wavelength of the laser is tuned within the vicinity of an absorption molecular (or atomic) transition. In this situation, the optical signal is distorted by the spectral line generating an output signal that makes possible

to recover the absorption spectrum of a gaseous sample. Besides this, the phase of the detection system can be adjusted to obtain the quadrature component of the beat note that is directly related to the dispersive distortion suffered by the optical signal (for more details refer to [20]). Therefore, FMS allows for measuring not only the absorption, but also the dispersion spectrum of the sample. In the same way, the baseline problem is solved and, given the high frequency of the generated beat note, the signal to noise ratio is improved with respect to previous methods. Nevertheless, the normalization issue is still present. FMS signals are dependent on the total amount of power impinging on the receiver and, hence, are difficult to manage in open path gas monitoring sensors.

Two-Tone Frequency Modulation Spectroscopy (TT-FMS), that was presented in 1985 by Cooper and Gallagher [24], is a derivation of FMS that allows the use of low bandwidth detectors. The laser beam is modulated by two high frequency signals that are only separated by an offset of a few MHz at maximum before it travels through the gas sample. As the light impinges on a photodiode, a beatnote with a frequency equal to the frequency offset between the modulation signals is generated having equivalent information to that of the pure FMS output signal. Even though the normalization problem affects TT-FMS in the same way that it did with FMS, the second modulation opens the possibility to employ low-bandwidth large area photodetectors improving the sensitivity of the sensor. This features have been exploited in different works [25–27]. As disadvantages, it is possible to mention the considerable increase in the complexity of the sensor and the loss of the ability to detect dispersion.

With the modulation techniques previously presented (WMS, FMS and TT-FMS) the baseline problem is automatically solved improving at the same time the sensitivity of the detection setups. Nevertheless, the normalization problem is still present and, in order to overcome it, two distinctive research lines have been followed. The first is focused on adapting absorption based schemes to be amplitude independent, and the second one proposes dispersion based methods.

It could be said that the first research line (intensity independent absorption spectroscopy) was started by Cassidy and Reid in 1982 [28] when they proposed the normalization of the higher harmonics of the WMS signal by the amplitude of the first harmonic (1*f* normalized WMS). This results in a power-normalized WMS signal that is immune to DC power fluctuations. Their work was later followed by Uehara and Tai [29] and

Iseki, Tai and Kimura [30], and more refinements and developments of this idea have also been published. The recent works of Rieker et al. [31], Bain et al. [32] and Sun et al. [33] stand out among them.

Unfortunately, there is not such a thing as a 1*f* normalized WMS version neither for DLAS, nor for FMS. This assertion looks obvious in the case of DLAS but not for FMS given that the differences with respect to WMS are very small. It has to be noted, however, that the detection schemes of the two techniques are quite different. Whereas in WMS different harmonics of the modulation signal can be easily monitored at the same time, in FMS the reception is far more complex. The signal of interest is, in fact, the first harmonic, and even though it is possible to obtain equivalent information from the second harmonic, it has not been probed yet that a relationship between the two tones can be used for getting normalization free operation. On top of that, the complexity of the design of the sensor will probably increase far beyond the point that is reasonable for the gain in performance that would be obtained.

Dispersion-based TDLS methods have not received traditionally as much attention as absorption techniques. Nevertheless, its importance has remerged as a mean for overcoming the limiting normalization problem of absorption-based approaches. Besides this, the linear relationship between concentration and dispersion leads to an improvement of the dynamic range of the instrument.

As a difference with optical intensity, it is not possible to measure directly the optical phase of an optical signal travelling through the sample, and some type of interferometric or heterodyning approach is needed to perform this measurement. Even though not as a proper spectroscopic techniques, several publications [34–38] have been presented in which classical interferometric approaches have been employed to measure dispersion in the vicinity of molecular spectral lines. Also, as it was previously said, FMS not only can recover the absorption profile of a medium, but it is also able of recovering the refractive index as a function of the frequency. By controlling the phase of the signal captured by the photodiode before the downmixing (consult Ref. [20] for further information) the in-phase and quadrature components of the beat signal can be selected to yield the absorption and dispersion spectra respectively. Nevertheless, these output signals are affected by variations in the power transmitted through the gas. The sensitivity of FMS can be improved by several orders of magnitude using cavity-enhancement techniques: Noise-

Inmune Cavity-Enhanced Optical Heterodyne Molecular Spectroscopy (NICE-OHMS) was proposed by Ye et al. [39] and it basically consists on a combination of a FMS system and an optical cavity. However, not only the laser must be locked to a cavity mode, but also the modulation frequency must be controlled with high precision to match the free spectral range of the cavity. Different implementations have been presented [40–42] and a good analysis of NICE-OHMS can be found in Ref. [43]. Nevertheless, this kind of systems is not really devised to be taken out of the laboratory and its utility in the field sensors area is very limited.

It has not been until very recently when Chirped Laser Dispersion Spectroscopy (CLaDS) [44] was proposed as a technique for dispersion spectroscopic measurements capable of overcoming problems like the normalization or the limited dynamic range of absorption-based instruments. This technique, as well as the novel approach for molecular dispersion spectroscopy that was presented in paper [A], are thoroughly reviewed in the chapter 2 of this dissertation.

1.3.2 Wide-band spectroscopic methods

TDLS narrow-band methods take advantage of the near-monochromatic spectrum of lasers for the extraction of the spectral information. The signal detected at a given moment is directly related to the emission wavelength of the laser at that particular moment. Thus, the measurement carried out by the detection subsystem during the complete sweep range of the laser yields the absorption or the dispersion profile of the sample as a function of the wavelength. Instead, when continuous broadband emitters are used as sources, the whole spectrum of frequencies reaches the photodetector all the time. Therefore, it is not possible to directly differentiate the contributions at different wavelengths and a spectral interrogation method must be used for spectral component separation (as a reference the optical spectrum of a broadband Tungsten-Halogen lamp is shown in Fig. 1-11).

The simplest wide-band spectroscopic approaches for continuous illumination sources are based on spectrometers that separate the frequency components of the optical signal allowing the wavelength dependent characterization of the spectrum transmitted (or reflected) through the sample. The various technologies for the implementation of spectrometers, from the refractive prism to diffraction grating or monochromators, offer

different spectral resolutions, detection ranges and flexibilities of configuration. Nonetheless, the wide-band gold standard, is Fourier Transform Infrared (FT-IR) spectroscopy [45].

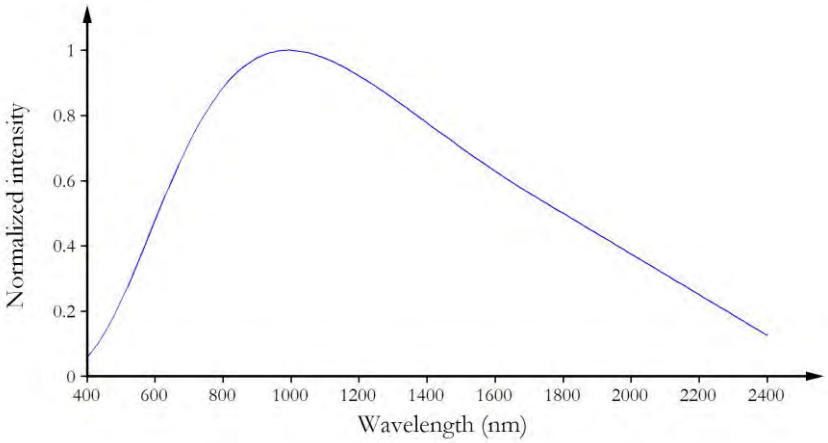

Fig. 1-11. Optical spectrum of a Tungsten-Halogen lamp.

In FT-IR spectrometry the spectral interrogation is performed taking advantage of a Michelson interferometer (even though other architectures are also in use). The simplest FT-IR spectrometer architecture is shown in Fig. 1-12 in which the light from a continuous optical source is divided in two paths and recombined before travelling through the sample and being detected. The particularity of the system is that one of the mirrors of the interferometer is movable being possible to adjust the difference in the lengths of the two optical paths. Therefore, considering monochromatic illumination, when the position of the mirror is that that make the optical path difference to be equal to a multiple of the wavelength of the optical signal, constructive interference occurs and the combined signal reaches its maximum. In the same way, when the difference between optical paths (known as retardation) is equal to a multiple plus half wavelength there is destructive interference and the signal goes to its minimum value. When the mirror is moved at a uniform speed, the interference between the two optical paths generates a sinusoidal modulation of the optical intensity that is known as the interferogram. Then, the frequency of the variation of the optical intensity depends on the wavelength of the optical signal and the speed at which the mirror is moved. It is possible to extrapolate now this behavior to an signal with multiple optical frequency components. The

result would be an interferogram in which the optical intensity of each component is sinusoidally modulated at a frequency directly dependent on their wavelength.

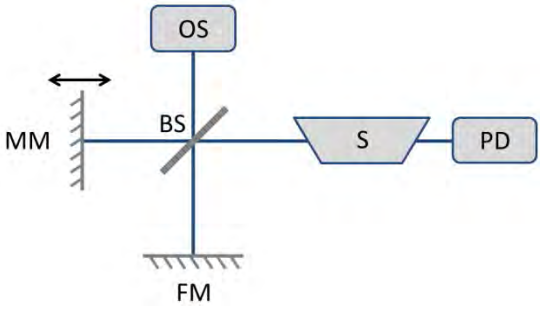

Fig. 1-12. Basic architecture of a FT-IR spectrometer. OS, Optical source; BS, Beam splitter; MM, Movable mirror; FM, Fixed mirror; S, Sample; PD, Photodiode.

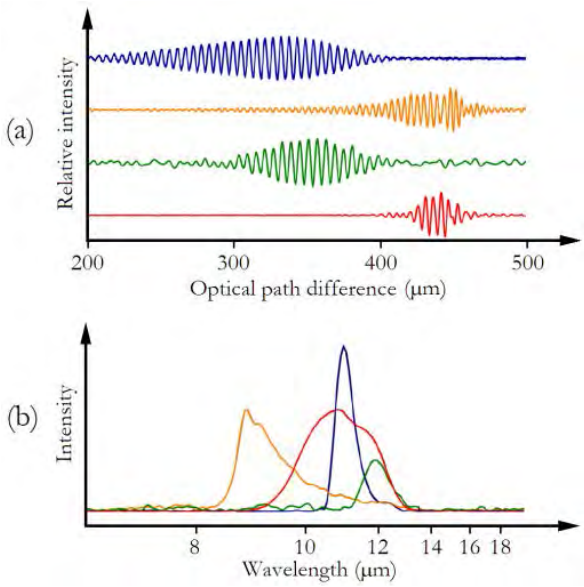

Fig. 1-13. Examples of FT-IR (a) interferograms and the (b) correspondent spectra [46].

As it was previously said, the output of the architecture of Fig. 1-12 is an interferogram in which the amplitude of each spectral component of the illumination spectrum is modulated at a certain frequency. To obtain finally the optical spectrum, FT-IR spectroscopy requires (and that is the reason for its name) a Fourier transformation of the interferogram to be performed. Therefore, the interferogram has to be digitized by an acquisition system and a Fourier transformation yields the optical intensity as a function of the frequency of the signal measured by the photodetector. Four examples of interferograms and their correspondent intensity spectra are shown in Fig. 1-13 [46].

Using the basic scheme of FT-IR spectroscopy of Fig. 1-12 is not possible to measure the optical dispersion induced by the sample. The reason for that is that the two optical beams of the interferometer are combined before travelling through the sample and thus both waves experience the same dispersion (same phase shift) producing no overall effect on the phase of the interferogram. A modified architecture for dispersive FT-IR spectroscopy is presented in Fig. 1-14, in which the position of the sample has been shifted to one of the branches of the interferometer (any of the two branches can be selected with similar results). In this way, the profile of the refractive index of the sample introduces a phase shift in one of the optical beams that is reflected on the final interferogram and can be detected.

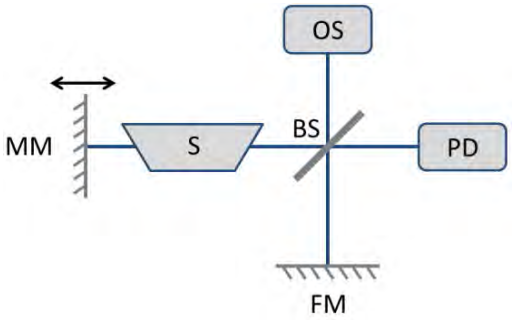

Fig. 1-14. Architecture of a dispersive FT-IR spectrometer. OS, Optical source; BS, Beam splitter; MM, Movable mirror; FM, Fixed mirror; S, Sample; PD, Photodiode.

Even though the basic FT-IR spectroscopy scheme is quite simple, many considerations must be taken into account for the implementation of

these instruments. Firstly, the resolution of a FT-IR system is given by the maximum retardation; this implies that the resolution of the spectrometer is limited by the maximum range of movement of the mirror. Secondly, the spectral coverage of the system is, not only determined by the optical source, but also by the sampling frequency of the interferogram. Coarsely speaking, the sampling must be performed at retardation intervals equal, at least, to the inverse of two times the maximum frequency reaching the detector. The position of the movable mirror must then be precisely monitored to ensure equal sampling intervals and high frequency accuracy. It is, therefore, the precision with which the movable mirror is controlled what mainly marks the performance of the whole system. Thus, the major constrain of a FT-IR spectrometer is the fact that its performance is related to a large extent to a mechanically driven component of the system.

The pulsed nature of OFCs (that were briefly introduced in the first section of the chapter) allows to overcome these restrictions and makes possible the implementation of wide-band spectrometers without movable parts. OFC-based spectrometers are thoroughly reviewed in chapter 3, where also new architectures and detection schemes are proposed.

1.4 SPECTRAL ANALYSIS METHODS

In the diagram of a spectroscopic system of Fig. 1-1 the different blocks that make up a complete instrument were presented. This scheme can now be reviewed in more detail using for illustration the FT-IR spectroscopic technique presented in the previous section. In that way, a broadband light source would be employed in an architecture in which a Michelson interferometer and a photodetector constitute the detection block. The output of the spectroscopic technique is an interferogram that has to be acquired and digitally processed. In FT-IR spectroscopy this processing is mainly a Fourier transformation of the digitized interferogram that yields the measured optical spectrum. Nonetheless, further processing associated to the compensation of the spectral shape of the optical source is also needed. Generally, a measurement is performed without any sample to obtain a baseline level and, subsequently, a second measurement is carried out now with the sample in place. The ratio between the actual measurement and the baseline yields the absorption or dispersion profile of the sample. This absorption (or dispersion) profile has to be further

processed for information extraction by spectral analysis methods in order to obtain the target results of the instrument (this process is known as calibration). These target results are usually the concentrations of certain analytes but, as it said previously, it can also be the temperature, the speed at which molecules are moving or any other parameter of the medium. The spectral analysis method is therefore very dependent not only on the available spectral information but also on the targeted results.

One of the simplest scenarios for spectral analysis is that of single-species gas detection and monitoring in which the concentration of gas can be directly extracted from the measurement of the optical spectrum in the vicinity of one of the transition lines of the target molecule. Both absorption and dispersion are directly related to the concentration of gas allowing an easy monitoring of the composition of the sample. In the opposite case, the calibration process is far more complex in an instrument that is devised for multi-species detection. The problem might not be that complicated in multi-species gas detectors given that at low pressure transition lines of different molecules can be independently measured without any overlapping between them. Nevertheless, in the multi-species analysis of liquids and solids the measured spectrum is the result of the contributions of all the components of the sample. As presented in the first section of the chapter, the most common example of highly complex multi-species optical media are biological tissues, in which the spectral contributions of a huge number of tissue components overlap. It is then not possible to directly separate the spectra of the target analytes for the estimation of concentration. Various information extraction methods have been proposed to address this problem, nevertheless, the option that became standard procedure in some fields of spectroscopy and is becoming increasingly important in others is the use of spectral classification algorithms [47–49].

Multivariate data classification algorithms provide a distinctive approach to the problem of spectral analysis for the extraction of information. The focus of these methods is the differentiation and quantification of the contributions of the different analytes that are present in the medium. In its application to spectroscopy, multivariate algorithms are able to recover and separate the individual spectra of several contributors from measurements of their mixes. There are, nonetheless, so many classification algorithms available that it is not always easy to find the right method for a certain application. One of the most robust and extended techniques is Partial Least Square (PLS) that has presented good results in complex biomedical problems [50–52]. Two other methods, Principal

Component Analysis (PCA) and Independent Component Analysis (ICA) are presented in chapter 4 and employed to assess different states of blood concentration in a bioengineered skin substitute.

1.5 SPECTROSCOPIC SYSTEM INTEGRATION

The integration of each of the sub blocks into a self-contained device capable of autonomously carrying out measurements and presenting the results to an end user is the last of the steps in the development of a spectroscopic system. As it was said previously, in most laboratory demonstrations and during the first stages of development of an instrument, most of the tasks related to the operation of the spectroscopic characterization setup, data acquisition, data pre-processing and spectral analysis are very often performed manually. In a final system, even though the complexity of the system varies strongly from instrument to instrument, these procedures have to be performed automatically. A generic block diagram of the electronics for signal processing and instrument control of an optical spectroscopic device is shown in Fig. 1-15.

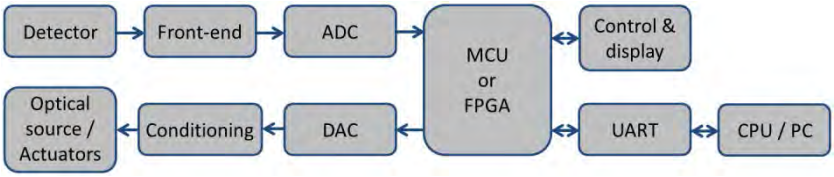

Fig. 1-15. Block diagram of the electronics for signal processing and instrument control of an optical spectroscopic system. ADC, Analog to digital converter; DAC, Digital to analog converter; MCU, Microcontroller; FPGA, Field programmable gate array; UART, Universal asynchronous receiver-transmitter; CPU, Central processing unit; PC, Computer.

The main component of the electronic system is the microcontroller. Microcontrollers are designed for embedded applications and contain, therefore, not only a processor but also memory and peripherals. A microcontroller can be programed to perform (with or without help from extra components) data processing and instrument control enabling automatic system operation. Whereas some systems have a dedicated control

panel with a data display screen and switches or push buttons for control, others are provided with a communication interface that allows the user to manage the instrument using a computer, nonetheless, most high-end systems have both possibilities. The second approach allows to use the computer (that is commonly much more powerful that the processor of the microcontroller) for signal processing, reducing the requirements of the electronics of the sensor.

The design of the processors (included in the microcontrollers) is not always well suited to perform tasks like high speed data processing or multi-channel parallel processing, and in these situations additional hardware must be employed. Several options are available, from the use of Digital Signal Processors (DSP) to custom microcontrollers designed to perform certain tasks with maximum performance that are of general use in large-scale macro-production devices. Nevertheless, in the usual small-scale of fabrication of spectroscopic instruments, Field Programmable Gate Arrays (FPGA) are equally powerful and much most cost-effective. FPGAs are devices that can be programed to perform hardware (instead of software) data processing, resulting in a significantly faster operation in certain tasks due to their parallel working nature. These parallel processing capabilities are also very useful in multichannel synchronous data processing.

Independently of the processing unit, the interface between the controller and the instrument itself is (almost in any case) made by analog to digital and digital to analog converters, ADC and DAC respectively. As shown in the upper left part of Fig. 1-15, the optical signal captured by the photodetector must be first electronically conditioned (common circuits are transimpedance amplifiers and programmable gain amplifiers) before being digitized by an ADC. The digital signal can now be processed by the controller to obtain, for example, the Fourier transformation and perform the spectral analysis. In the same way, the control of the optical sources or the actuators of the instrument (movable mirrors, optical switches…) is performed in the other direction. An analog signal generated by a DAC is conditioned and used a specific component of the system.

Besides the hardware design, the development of the control software is equally important. Different routines must be written to address each of the tasks that must be performed by the system. Usually low level software functions are in charge of the communication with the different components of the system (this communication is performed through writing and reading from registers), whereas high level functions manage the

functionality of the whole system, from data reading, to the presentation of results. The design of these functions and routines is also very dependent on the overall architecture of the instrument and differ between computer based sensors and self-contained analyzers.

An example of system integration in which a spectroscopic instrument has been developed to perform a viability study is presented in chapter 4. In this system, an amplitude modulated multiple laser illumination source and a multi-channel phase-sensitive detection architecture have been implemented for the measurement of the reflectance of biological samples. The detection scheme, a microprocessor and some additional electronics have been embedded into a FPGA that allows the whole system to be controlled by a user interface running into a computer.

1.6 OBJECTIVES AND ORGANIZATION OF THE DISSERTATION

This doctoral dissertation is focused on the development of the different aspects of spectroscopic systems for the implementation of reliable and fast optical instruments. The main line of work has been the development of new methods and architectures based on devices and techniques used in RF and optical communications for narrow and wide-band dispersion spectroscopy that provide a more robust operation than that of absorption spectroscopic methods. In this way, devices like lasers, photodiodes, optical combiners or high speed optical intensity modulators from optical communications have been used in conjunction with techniques like synchronous phase-sensitive detection or optical heterodyning. Further work has also been done in the area of spectral analysis and system integration with the design, development and the validation of the performance of a diffuse reflectance spectroscopy instrument based on data classification methods for biomedical applications.

In chapter 2, the contributions to narrow-band dispersion spectroscopic techniques are reviewed. A novel heterodyne phase-sensitive detection method for molecular dispersion spectroscopy based on tunable lasers is presented and experimentally validated. This technique is based on the measurement of the phase shift induced on a three tone optical signal by the variations of the refractive index of the sample. The method is baseline

free, immune to fluctuations of the received optical power, and offers an output linearly dependent of the gas concentration. Moreover, an analytical model has been developed enabling calibration-free operation. Several of the ideas that emerged from the works carried out towards the development of the heterodyne phase-sensitive detection method were of direct application to the CLaDS dispersion spectroscopic technique. Therefore a new CLaDS architecture is also proposed and presented in chapter 2. The setup simplifies previous implementations and can be considered as a step forward in reducing the complexity of current sensors bringing these analyzers a step closer to be self-contained and field-deployable.

The spectral range and the speed at which the previous methods can operate are limited by the capabilities of the tunable lasers used to sweep the spectral range of interest. In chapter 3 a new multiheterodyne molecular dispersion spectroscopy method based on a dual-comb optical source generated by the modulation of a single continuous wave laser that can simultaneously measure dispersion at multiple points is presented. The aim of this work is to make possible to take advantage of the potential of optical frequency combs out of the laboratory. The multi-channel parallel lock-in detection scheme proposed measures the phase shift induced in each of the teeth of the measurement comb enabling high speed operation. This is in contrast with the semi-static characterization operation performed by traditional OFC-based instruments. The method features a combination of simple implementation and ease of configuration in which most of the complexity of classical OFC approaches has been shifted from the optical to the electronic domain. The range of application of the multiheterodyne dispersion method here introduced goes far beyond molecular dispersion spectroscopy, therefore, also in chapter 3, a robust dual-comb absorption spectrometer architecture based on the previous design is presented and validated both for spectroscopic measurements and the characterization of optical components. The strong points of the setup are its simplicity (in comparison with traditional dual-comb implementations), low-cost, easy operation and configuration, high stability and high output data rate.

Apart from the new techniques and architectures and completing the scheme of a spectroscopic instrument of Fig. 1-1, different spectral analysis and system integration tasks were carried out for the development and validation of a reflectance spectroscopic sensor for monitoring the evolution of bioengineered skin substitutes in the first days after engraftment. The stand-off instrument, that was based on data classification methods (PCA and ICA), has been able to non-invasively differentiate between the

evolutions of grafts with different states of angiogenesis. This work is presented in chapter 4 and proves that the spectral analysis method and the integration of the instrument are as important as the spectroscopic technique for the overall performance of the instrument.

Chapter 5 gathers the main conclusions that can be extracted from this dissertation.

2. NEW DETECTION METHODS AND ARCHITECTURES FOR DISPERSION SPECTROSCOPY BASED ON TUNABLE LASERS

As it was presented in the introduction chapter, an important number of narrow-band optical spectroscopic techniques have been proposed during the last decades for the detection, estimation of concentration and monitoring of atoms and molecules in gaseous phase. Given the particular characteristics of this problem, most of these methods are based on tunable laser sources. In general terms, an optical spectroscopic system can be focused on two completely different, however closely related, approaches: absorption and dispersion spectroscopy. As previously introduced and as will be detailed throughout this chapter, the particular features of dispersion spectroscopy make this solution particularly well suited for its application in the design of open path gas analyzers [53].

Open path optical gas sensors, in contrast to closed path sensors, do not require sampling the gas and taking it to the interior of the sensor itself, but the analysis is somehow performed in the mass of gas surrounding the system. Hence, these schemes are particularly prone to suffer problems related to particles in suspension (partially blocking the optical path or depositing on optical elements of the sensor) and power fluctuations induced by atmospheric turbulences or pointing instabilities [54]. Therefore, for gas analyzers devised to have an open measurement path, the number of advantages of using spectroscopic methods that are not directly dependent of the total amount of power transmitted through the gas is noteworthy. This independence from power fluctuations is one of the main characteristics of dispersion spectroscopy and this is what positions it well in front of other alternatives in terms of suitability for the application.

Currently, the number of available dispersion spectroscopy techniques focused on gas detection and analysis is very reduced and, on top that, most of them are affected by important limitations regarding its field deployability. In this chapter, a new method based on heterodyne phase-sensitive detection for dispersion molecular spectroscopy is introduced. The technique, that bases its operation on RF techniques and optical communications components, presents several advantages over existing approaches. These advantages, that will be presented and justified in this chapter, are mainly in the line of providing simplicity of implementation and operation while keeping high performance standards. In the same way, some of the ideas developed for the heterodyne phase-sensitive detection method

have been applied to a CLaDS dispersion spectroscopy architecture greatly reducing the complexity of current implementations.

This second chapter of the dissertation provides the background necessary to place the contributions presented in papers [A] and [B]. Also, some additional information regarding the functioning and implementation of these proposed techniques is presented. Therefore, the next section contains a brief introduction to molecular spectroscopy in which the different types of gas analyzers are introduced, current dispersion based methods are presented, and the framework of the contributions is established. In the second section, the heterodyne phase-sensitive technique for molecular dispersion spectroscopy, presented in paper [A], is described. Next, the third section gathers the application of several of the ideas from the previous work to the design of instruments based on CLaDS (paper [B]). Finally, chapter 2 concludes with a short analysis of results and conclusions.

2.1 LASER MOLECULAR SPECTROSCOPY FOR OPEN PATH GAS SENSORS

The term "molecular spectroscopy" is in general applied to identify a group of spectroscopic techniques that are oriented to the study of atoms and molecules in gaseous state. As it was said in the introduction, the main feature of gas spectroscopy is the existence of very narrow lines of absorption (and hence, of dispersion) that are characteristic of the different gases. The position in the spectrum of the absorption lines can be determined by solving the Schrödinger equation of the molecule and its shape and width depend on the temperature and the pressure of the gas. As an example, the absorption coefficient of methane (measured in cm^{-1}) for wavelengths between 1625 nm and 1675 nm is shown in Fig. 2-1. The particular positions of the absorption features allow the identification of the molecule, and special care must be taken when designing a gas sensor to avoid any interference from absorption lines of other gases. Generally speaking, the strength of the line allows to extract the concentration of the gas in the sample, and the lineshape yields information mainly about the pressure.

Both open and closed path gas measurement systems are equally capable of analyzing the composition of a gaseous medium targeting

different molecules or atoms. Even though, independently from the spectroscopic techniques employed, their operating principles are exactly the same, the architecture of the two types of sensors is very different. In a closed path sensor the analysis of the gas is performed within an optical cavity located into the sensor itself. In this situation, the laser beam travels inside this optical cell and therefore gas must be pumped into the cavity prior to carrying out the analysis. As opposed to this, in open path systems, the measurement is performed outside the sensor system, not using any gas cell or closed cavity, but free space (a more extent review of open and closed path sensors can be found in Appendix I).

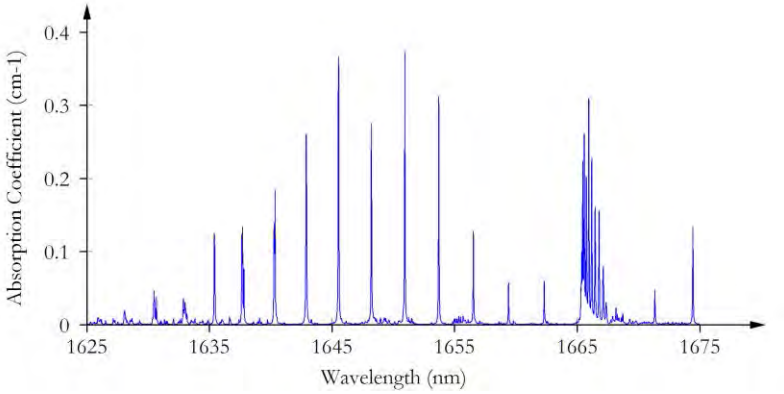

Fig. 2-1. Absorption coefficient of methane in the vicinity of 1650 nm [5].

Each of the two sensor architectures has its own benefits and drawbacks. To begin with, the disadvantages of the closed path systems are mainly related to the need of pumping the gas sample into the optical cavity, not only because of the power consumption of the pump (an important problem in remote locations without direct access to power lines), but because of the problems associated with the tubing. The main issues are the delay introduced by the tubing system and the (usual) need of correcting factors to account for, for example, pressure and temperature variations due to the pumping process. The measurement is also affected, more importantly, by tubing sorption, a mechanism whereby certain molecules become attached to the tubes themselves, filters, or any other ducting component. This is potentially quite an important issue for CO_2 and H_2O sensors. By contrast, closed path sensors are very robust to atmospheric

phenomena like fog and rain and are particularly well suited to dusty conditions, where filters play an important role [55].

Meanwhile, open path sensors suffer from problems associated to any interference with its optical path. First, it can be quite complex to maintain a good optical alignment and a good cleanliness of the optical elements exposed to the environment. Besides this, given that the optical setup is completely exposed to the weather, even light rain or snow can prevent the system to work properly by the continuous obstruction of the light path. Problems also emerge in dusty environments, not only because of the deposition of particles in the optical elements of the sensor, but also because of the possibility of fast partial blockings of the optical path. Hence, even though the issues presented by closed path sensors related to tubing are automatically solved by open path sensors, their weakest point is the sensitivity of current spectroscopic methods to fluctuations in the optical power reaching the receiver.

Dispersion characterization techniques can be used to overcome these limitations given that the measurement of the optical phase shifts associated to variations of the index of refraction can be performed independently of the optical intensity transmitted through the medium [53]. The measurement of dispersion has not only been used for gas monitoring and analysis [44,56], but also to assess different biological parameters [57,58]. An example of this second application field can be found in Appendix II, in which the architecture of an instrument for the estimation of the glucose concentration in water solutions based on the measurement of dispersion in the W-band (75 – 110 GHz) is presented. The results obtained indicate that the detected phase shifts are linearly related to the concentrations of glucose.

Although different approaches have been proposed, the dispersion profile is always obtained from the measurement of optical phase shifts induced by the changes in the refractive index of the sample. As it was previously said, the features of this measurement method overcome most of the issues presented by the absorption based methods previously presented. For instance, the measure of phase is not affected by the baseline problem and, in the same way, variations in the total amount of power reaching the photodetector do not induce output signal changes (normalization problem). Furthermore, as opposed to the exponential relation between the gas concentration and the optical power absorbed, there is a linear dependency between concentration of analytes and refractive index change (as presented in chapter 1). This enables dispersion based methods to have a huge

dynamic range in comparison with absorption techniques as it was experimentally demonstrated by Franz et al. [59].

Chirped Laser Dispersion Spectroscopy (CLaDS) [44] (Wysocki and Weidmann) was recently proposed as a technique suitable for field dispersion spectroscopic measurements in open path sensors. It was presented as a robust method capable of taking advantage of molecular dispersion for trace gas sensing, directly overcoming problems like the normalization, or the limited dynamic range. It is based on a frequency-chirped laser and takes advantage of the frequency shifts induced in a beat note due to variations in the index of refraction of the gas. These beat note frequency shifts are demodulated to recover the dispersion profile of the sample. The architecture of the instruments that were presented in the first publications [44,54] was based on a quantum cascade laser that was chirped in frequency at a reasonably high speed. The output of the laser is connected to a free space acousto-optic modulator before subsequently recombining the 0^{th} and 1^{st} orders diffracted by this modulator. Therefore, a two tone optical signal with a spacing equal to the driving frequency of the modulator is generated. When this signal is chirped over an absorption feature of a gaseous sample, optical dispersion induces a frequency shift between the optical tones. Hence, when a square law detector captures the power transmitted through the gas, the frequency of the generated beat note will be shifted depending on the sample dispersion characteristics. After performing frequency demodulation (using a high-end spectrum analyzer in all the implementations published so far), molecular dispersion can therefore be inferred from the frequency variations of the beat note.

An alternative detection scheme was also presented [54] to address what the authors considered the main limitations of the CLaDS method: the effect of noise in the demodulation process [60], and the issues associated to the different lengths traveled by the optical tones. Subsequent developments of the design enabled the measurement of nitrous oxide in an open-path configuration [53] and also of methane [61], with a revised architecture in which the acousto-optic modulator was replaced by an electro-optic amplitude modulator [62]. Nevertheless, the complexity of the architecture of the instrument is considerably high, and nothing similar to a stand-alone sensor prototype has been achieved yet.

The contributions of the dissertation discussed in this chapter are primarily focused on the development of dispersion techniques characterized by its immunity to absolute power fluctuations that can

directly overcome the most important current open path analyzer limitations. A novel calibration-free dispersion spectroscopy method named Heterodyne Phase-Sensitive Detection Spectroscopy (HPSDS) that improves some of the characteristics of CLaDS is presented in the next section. Besides this, in section 2.3, an optical heterodyning scheme for CLaDS that highly simplifies previous implementations is also introduced. Finally, the main conclusions drawn from the chapter are discussed.

2.2 HETERODYNE PHASE-SENSITIVE DETECTION FOR MOLECULAR DISPERSION SPECTROSCOPY (PAPER [A])

This section presents the work undertaken in this thesis towards the design and development of HPSDS, a new optical dispersion spectroscopic technique based on the idea of simplifying existing methods. The reasoning behind this concept makes possible the field deployability of reasonably simple molecular dispersion spectroscopy open path gas analyzers. This contribution is described by paper [A]; the reader is referred to this publication (section 6.1) for a full description of the method.

2.2.1 Description of the technique

The architecture presented in this section is based on a laser that is intensity modulated at high frequency generating a three tone optical signal. The profile of the refractive index in the vicinity of the absorption line induces different propagation velocities for each of the three optical tones when this signal is swept across a molecular spectral line. This results in optical phase differences between the tones that are measured to estimate the dispersion profile. It is then possible to do an assessment of, between other characteristics of the sample, the concentration of analytes from the dispersive optical measurement. Since the only parameter of interest for the proposed spectroscopic method is the phase of the optical signals, the technique is robust to fluctuations of the optical power. Therefore the method is inherently baseline-free and does not require normalization. Furthermore, the linear relationship between the concentration of the gas and the change in the index of refraction (in opposition to the exponential

relationship with absorption) provides an extended dynamic range in comparison with absorption based sensors. The existence nowadays of spectral databases like HITRAN [5] make possible the calibration-free operation of sensors taking advantage of propagation models. Hence, an analytical model for determining the effect of the spectral feature on the phase of the optical signals has also been developed (section 2.1 of paper [A]).

As presented on paper [A], the phase of the beatnote that is generated when the three tone HPSDS spectral interrogation signal impinges on a photodiode is a function of the profile of the index of refraction $n(\omega)$ of the sample and the modulation frequency Ω_1:

$$\varphi_o = \frac{\omega_0 L}{2c}\left(n(\omega_0 + \Omega_1) - n(\omega_0 - \Omega_1)\right) \tag{2-1}$$

where ω is the optical frequency, L the length of the gas sample and c the speed of light. It is therefore possible to recover the index of refraction from the measurement of phase during the sweep of the spectral feature by the tunable laser. For optimum performance, the modulation frequency and the frequency of the beatnote is in the GHz range when targeting ambient pressure gases. A frequency downshift is thus necessary to obtain the measurement of phase without compromising the complexity and cost of the system. The electronic heterodyne frequency down-conversion scheme that is shown in Fig. 2-2 was then proposed.

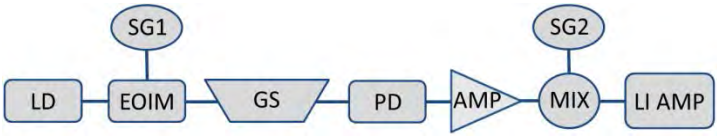

Fig. 2-2. Basic block diagram of a heterodyne phase-sensitive molecular dispersion spectroscopy sensor based on electrical frequency downmixing. LD, Laser diode; SG1, Signal generator at frequency Ω_1; EOIM, Electro-optical intensity modulator; GS, Gas sample; PD, Photodiode; AMP, Radio frequency amplifier; SG2, Signal generator at frequency Ω_2; MIX, Radio frequency mixer; LI AMP, Lock-in amplifier. (Fig. 5 of paper [A])

A second architecture based on optical heterodyne frequency conversion (Fig. 2-3) was also proposed for an improved performance and flexibility of operation. Six extra optical tones (see Fig. 2-4) are generated as a result of the second modulation that provides a low frequency beatnote on the photodetector that can be detected by the lock-in amplifier.

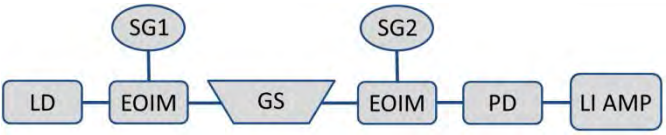

Fig. 2-3. Basic block diagram of a heterodyne phase-sensitive molecular dispersion spectroscopy sensor based on optical frequency downmixing. LD, Laser diode; SG1, Signal generator at frequency Ω_1; EOIM, Electro-optical intensity modulator; GS, Gas sample; SG2, Signal generator at frequency Ω_2; PD, Photodiode; LI AMP, Lock-in amplifier. (Fig. 6 of paper [A])

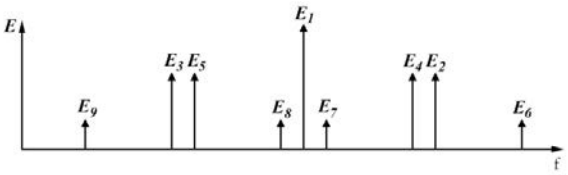

Fig. 2-4. Optical spectrum of the nine tone signal generated by the second electro-optical intensity modulator. (Fig. 7 of paper [A])

2.2.2 Adjustment of the modulation frequency

Some details that were not included in the paper regarding the effects of the modulation frequency of the HPSDS system on the output signal are given in this section.

As repeated throughout paper [A], there is an optimum modulation frequency of the tunable laser (that controls the spacing between the three tones of the spectral interrogation signal) for the measurement of a spectral feature of a certain linewidth. As a complement to the results presented on the paper, the HPSDS output for the optical downconversion scheme for

modulation frequencies between 2 and 12 GHz in the characterization of the same spectral feature are shown in Fig. 2-5. It is possible to see that the peak to peak phase difference is increased up to its maximum value at 8 GHz and starts decreasing afterwards. A modulation frequency swept like the one shown in Fig. 2-5 but with a finer resolution was used for the estimation of the optimum operation point in the experimental validation performed in paper [A]. Another aspect that must be noted is that the separation between the two maximums of the signal is directly related to the linewidth of the spectral feature and the modulation frequency, therefore it is possible to perform a rapid estimation of the FWHM of the spectral line. This assessment can be then used for readjusting the modulation frequency for optimum detection performance.

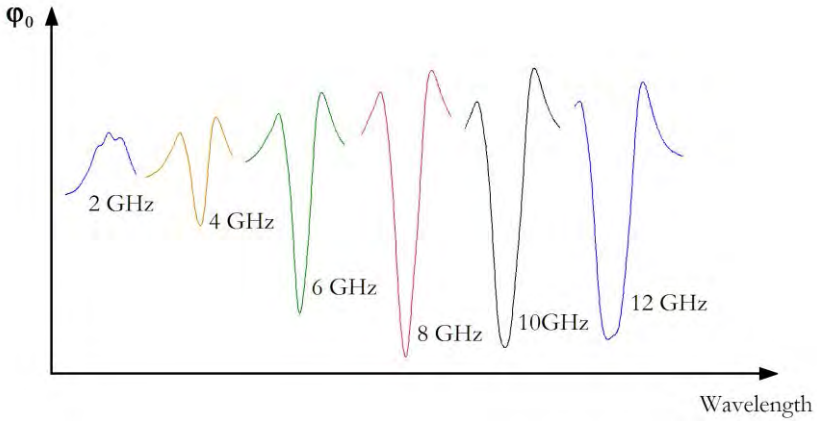

Fig. 2-5. Measurements of the 1650.96 nm transition of methane for various modulation frequencies.

2.2.3 Model for calibration-free operation

Further details, not included in paper [A], about the calibration-free model and the influence of pressure in the measurements are described below. With regard to the model for obtaining the output phase of the HPSDS technique, spectroscopic information from HITRAN was used in the calculations. Following the description of the data compilation found on

the 2012 HITRAN report [5] it is possible to calculate the absorption coefficient of the molecular gas sample. The profile of the index of refraction is obtained from the absorption coefficient using the Kramers-Kronig equations (chapter 1). Then, the output signal is calculated by using Eq. (2-1).

In the experimental validation carried out in paper [A] methane was used as the target gas, performing measurements in the vicinity of 1651 nm, where several ro-vibrational lines are present. In the calculations for the calibration-free model from spectroscopic data, it must be noted that the spectral line of methane targeted in the paper (that is shown in Fig. 2-6 (a)) is the actual result of the overlapping of the four molecular transitions shown in Fig. 2-6 (b).

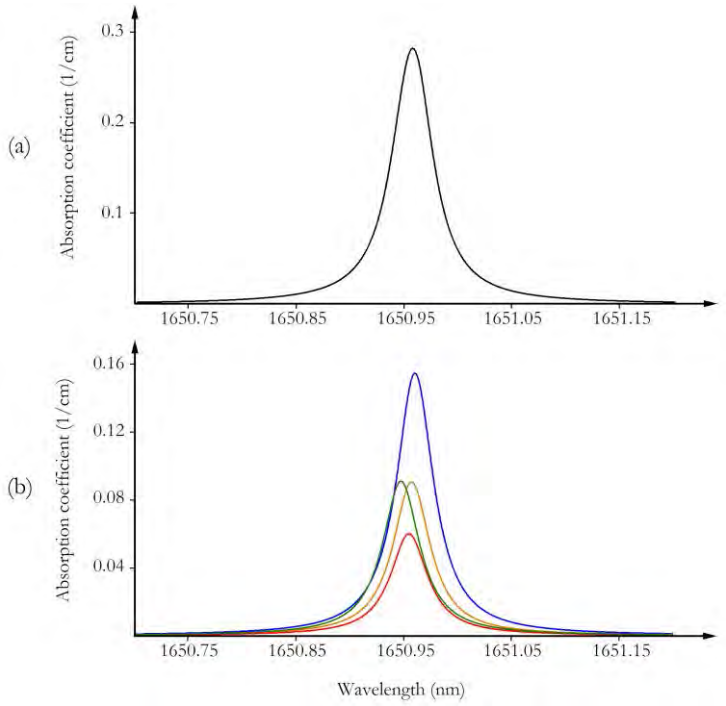

Fig. 2-6. (a) Absorption coefficient of methane in the vicinity of 1650.96 nm at 1 atm. This spectral feature is the result of the overlapping of the four lines shown in (b) [5].

The high proximity between the center frequencies of the four features ensures minimal variation in the dispersion profile and the output signal (with respect to a single absorption line) for pressures close to atmospheric pressure. Nevertheless, at very low pressure it is necessary to account for the effect of the narrowing of the absorption lines. To illustrate this, the profile of the index of refraction at low pressures is shown in Fig. 2-7 (a) and a simulation of the phase of the optical downconversion setup for this refractive index in Fig. 2-7 (b). The independent contributions of the four lines are now evident and in clear contrast to the signal measured by the HPSDS instrument at high pressure (Fig. 2-9).

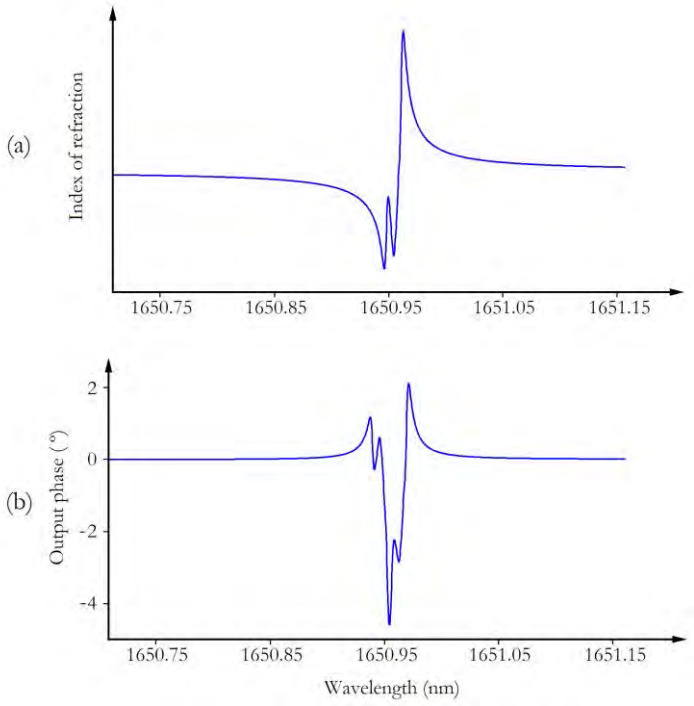

Fig. 2-7. (a) Profile of the index of refraction of methane around 1650.96 nm at 0.1 atm. (b) Simulation of the phase shift induced in the HPSDS signal with the optical downconversion scheme for a gas concentration of 7.5 %. As previously said, the profiles are calculated from the absorption coefficient using the Kramers-Kronig equations.

As presented in the previous paragraphs, and as happens in any other molecular spectroscopic technique, the pressure of the gas sample has an

important effect on the output phase. This does not affect the calibration-free performance of the system given that this influence can be accurately modeled from spectral data from HITRAN or any other spectral data base.

2.2.4 Experimental validation

The performance of the two HPSDS implementations of Fig. 2-2 and Fig. 2-3 was validated using the setups described in paper [A]. The results are shown in Fig. 2-8 and Fig. 2-9 for the electronic and optical downconversion schemes respectively. In the same way, the calculations for optimum modulation frequency and the immunity of the method to optical intensity fluctuations were proved.

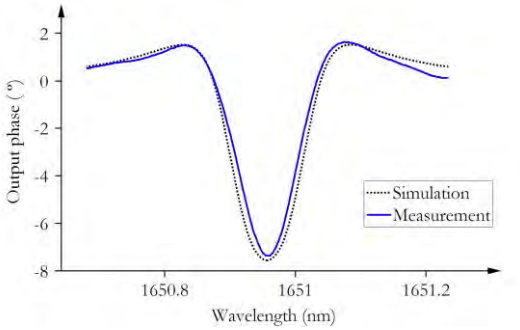

Fig. 2-8. Phase shift induced in the optical signal by the ro-vibrational transition of methane at 1650.96 nm recovered using the electrical frequency downshifting approach. (Fig. 8 of paper [A])

As previously stated, two heterodyning approaches have been proposed, one based on a conventional electrical downmixing scheme and a second based on optical frequency conversion. Both alternatives have been validated using the ro-vibrational line of methane at 1650.95 nm obtaining detection limits of 60 and 12 ppm*m/Hz$^{1/2}$ respectively. The electrical setup is slightly more complex to implement than the optical version: high-speed photodetectors and RF mixers and amplifiers are necessary, whereas only an extra intensity modulator and a slow photodiode are required for the optical scheme. Besides this, the immunity to noise and interference of the optical elements is far better than for the RF components, and this has an effect on

the achievable SNR. As found in the experimental validation, the SNR of the electrical conversion method is improved in almost an order of magnitude by the optical approach and this behavior is directly reflected in the detection limit of the instruments. The possible range of modulation frequencies is also a factor that must be taken into account given that it is very important to adjust the modulation frequency to the optimum point in order to obtain optimum performance. In the electrical setup this operation range is limited by the RF components being very dependent on the quality of the devices. In the optical setup the operation range is only limited by the optical intensity modulators that usually have a bandwidth that goes from DC to a few tens of GHz, having therefore much higher flexibility of configuration.

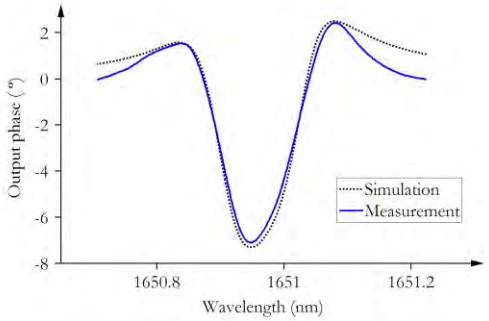

Fig. 2-9. Phase shift induced in the optical signal by the ro-vibrational transition of methane at 1650.96 nm recovered using the optical frequency downshifting approach. (Fig. 9 of paper [A])

Besides this, an analytical model for the propagation of light in a dispersive medium has been developed to enable calibration-free operation using as input data from a spectral database. From simulations performed using an analytical expression based on a low gas concentration approximation, calibration-free accuracies of 4.5% and 3.5% were obtained for the electrical and optical frequency conversions schemes respectively.

2.3 OPTICAL FREQUENCY DOWNCONVERSION ARCHITECTURE FOR CHIRPED LASER DISPERSION SPECTROSCOPY (PAPER [B])

As a direct consequence of the work performed towards the development of the HPSDS optical downconversion detection architecture, it became evident that several of the ideas that emerged were of direct application to other dispersion spectroscopic method like CLaDS (presented in the introduction of this chapter). These ideas were gathered in paper [B] and will be briefly discussed in this section. The reader is referred to section 6.2 for the full text of the publication.

2.3.1 Previous CLaDS implementations

CLaDS is a technique that has been extensively tested, validated and improved over the last few years. Different architectures, some of them based on quantum cascade lasers working in the mid-IR [44,54] and others based on laser diodes working in the range between 1500 and 1700 nm [61,62], have be presented and experimentally demonstrated. Similarly to what happens with the HPSDS method, in CLaDS there is an optimum modulation frequency for the maximization of the SNR of the sensor that very often lies within the GHz range [61]. Therefore, the beat note generated in the detector would equally be in the GHz frequencies. Because of the architecture of CLaDS sensors, it is necessary to perform a frequency demodulation of the beat note signal and given the complexity of performing this task at such high-frequencies, the common approach in all the references presented up to now has been to employ a high-end RF spectrum analyzer.

In paper [B] a new CLaDS architecture based on optical heterodyne frequency downmixing is presented. The setup makes possible the demodulation of the beat note using a low cost and compact frequency demodulator that is directly connected to a low-speed photodetector.

2.3.2 Optical downshifting frequency conversion scheme for CLaDS

The block diagram of the proposed optical frequency conversion architecture is shown in Fig. 2-10. The spectral feature induces a frequency shift in the chirped optical signal that can be measured to recover the dispersion profile of the sample. Nevertheless, it is necessary to detect small frequency changes (that can be of a few tenths of Hz) on high frequency signals and therefore some kind of heterodyning is fundamental. In paper [B], an optical heterodyning method similar to the one presented for the HPSDS method is proposed. Hence, a second electro-optic intensity modulator is placed after the gas cell before the photodiode. The beat note is shifted to an arbitrary low frequency that can be directly processed by a regular FM demodulator.

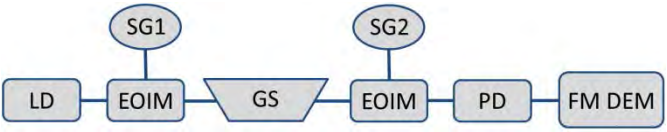

Fig. 2-10. Basic block diagram the optical frequency downmixing setup for Chirped laser dispersion spectroscopy. LD, Laser diode; SG1, Signal generator at frequency Ω_1; EOIM, Electro-optical intensity modulator; GS, Gas sample; SG2, Signal generator at frequency Ω_2; PD, Photodiode; FM DEM, FM demodulator. (Fig. 1 of paper [B])

Using the analytical expression for the time dependent phase of the beat note (Eq. (2-2)) it is shown that the output signal of the proposed setup is equal to that of the original CLaDS system presented by Wysocki and Weidmann [44]. The only variation is the downshifting of the central frequency from the modulation frequency of the tunable laser (in the GHz range) to an arbitrarily low frequency that can be easily controlled to yield within the frequency range of a low cost FM demodulator.

$$f(\omega) = \Omega_1 - \Omega_2 + \frac{SL\omega}{2c}\left(\left.\frac{dn}{d\omega}\right|_{\omega+\Omega_1} - \left.\frac{dn}{d\omega}\right|_{\omega-\Omega_1} \right) \qquad (2\text{-}2)$$

2.3.3 FM receiver implementation

By the limited extension of the letter in which this architecture was presented only rough details were given about the detector, now the full schematic is presented in this section together with pictures of the actual circuit implementation.

The schematic is given in Fig. 2-11 and it is based on the test circuit of the NE604A (Philips Semiconductors, Eindhoven, Netherlands) low power 455 kHz FM IF integrated circuit. The values of the components employed were 100 nF for C1, C2, C3, C4, C5, C7 and C8, 10 pF for C6, 15 nF for C9, 150 pF for C10, 1 nF for C11 and 6.8 μF for C12. In the same way, R1 was equal to 51 Ω, R2 and R3 to 1500 Ω and R4 to 100 kΩ. The RF filter F1 was a Murata CFULA455KB4Y-B0 with a center frequency of 455 kHz and a bandwidth of 15 kHz. Finally, the resonant LC circuit (F2) was implemented using a 180 pF capacitor and a 330 μH variable inductor with an adjustable range of 6%. A picture of the final PCB of the circuit is shown in Fig. 2-12.

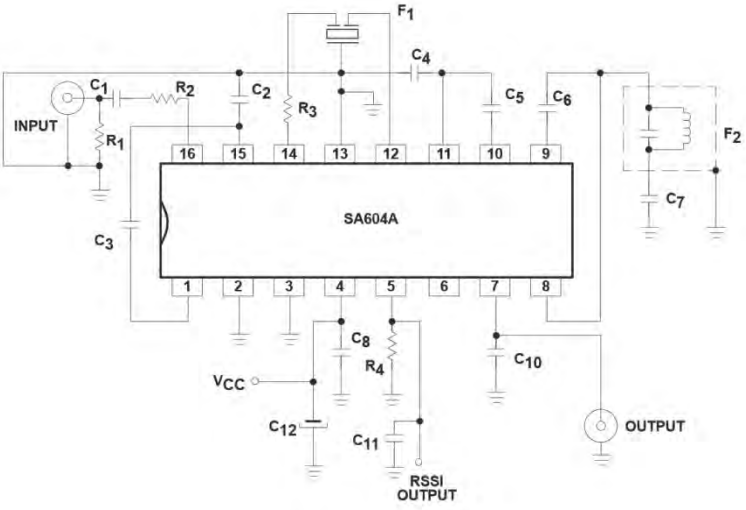

Fig. 2-11. Schematic of the low cost FM demodulator used in the experimental validation of the optical CLaDS architecture.

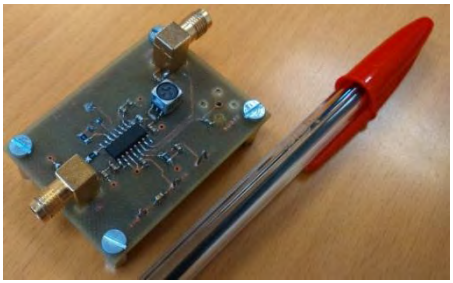

Fig. 2-12. Picture of the PCB of the FM demodulator. A pen is also shown for size reference.

2.3.4 Experimental validation

The optical frequency conversion scheme for CLaDS has been validated using again the transition of methane at roughly 1651 nm. The results that are shown in Fig. 2-13 provide a detection limit of roughly 6.5 ppm*m/$Hz^{1/2}$ a value in the same order of magnitude that the detection limit obtained by previous implementations of CLaDS [61] based on much more complex and expensive equipment.

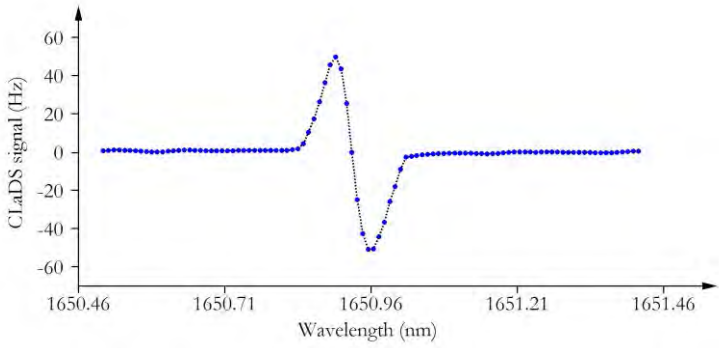

Fig. 2-13. Measured CLaDS signal (deviation from the central frequency) as a function of the wavelength. (Fig. 2 of paper [B])

2.4 DISCUSSION OF RESULTS

From the very first sections of this chapter the advantages of using dispersion based spectroscopic methods have been presented. These advantages are especially useful for open path gas analyzers in which the optical measurement path is in free space. New detection methods and architectures based on telecommunication, RF and optical processing techniques and devices for molecular dispersion spectroscopy have been introduced and experimentally validated conforming the first two contributions of the author (papers [A] and [B]).

The HPSDS technique presented on paper [A] is based on the measurement of the phase shifts induced on a three tone optical signal by the variations of the index of refraction (as a consequence of the presence of a gas) in the vicinity of a spectral transition. Given that only the phase of the beat note is measured and used for the estimation of concentration, the technique is inherently robust to power fluctuations in the optical path and, hence, does not require normalization. By the range of application, HPSDS can be directly compared to CLaDS. Both techniques are immune to power fluctuations and to the effect of the power baseline and have an extended dynamic range in comparison to absorption methods. Nevertheless, not necessarily form the implementation point of view, but heterodyne phase sensitive sensors are not nearly as complex as CLaDS analyzers in terms of data processing. As a reference, in CLaDS the absorption feature must be swept at high speed in a few microseconds and this usually introduces nonlinearities in the swept signal that distort the output of the sensor. In HPSDS the speed of the sweep has no effect of the output and can be freely chosen to obtain a certain output data rate. The effect of noise is also more problematic in a FM demodulation than in lock-in phase detection, given that, in the second case, the noise bandwidth is reduced by several orders of magnitude.

Besides this, some of the ideas that emerged from the work carried out towards the development of HPSDS are of direct application to CLaDS sensor and therefore a new architecture was proposed in paper [B]. The new scheme allows the use of a slow-speed photodiode and a low-cost regular FM demodulator to isolate the output signal in what supposes a noticeable reduction in the complexity and the cost of current CLaDS sensors. Besides this, the modulation frequency employed (that must be adjusted to match the FWHM of the spectral line for best performance) can be compensated in the second optical modulator to not have effect on the detection

subsystem and, therefore, the flexibility of the sensor is highly increased. Hence, the wide range of operation of the electro-optic modulators enables easily achievable optimum performance at any pressure. The new architecture brings CLaDS sensor design a step closer to the obtaining of a self-contained field deployable system.

3. DUAL OPTICAL FREQUENCY COMB BASED ARCHITECTURES FOR DISPERSION MOLECULAR SPECTROSCOPY AND ROBUST SPECTRAL CHARACTERIZATION

As briefly introduced in the first chapter of this dissertation, OFCs are light sources that provide a spectrum which consists of equidistant optical monochromatic tones. Various technologies for comb generation have been developed; among them the combs generated by passively mode-locked lasers have thousands of individual frequency components that are spread over a spectral range of more than an octave [1,2]. OFCs thus can be considered as an optical source that combines the advantages of lasers and broadband emitters. Nevertheless, as well as broadband emitters, OFCs need a spectral interrogation method for the extraction of the spectral information. Even though traditional methods can be used for performing this spectral interrogation (like spectrometers or FT-IR spectroscopy), dual-comb spectroscopy [63,64] is very often the detection method of choice due to its great potential. This technique, as presented in the next sections, is based on heterodyning two stabilized OFC in a way in which each optical tooth is individually mapped into the RF domain where many signal processing methods are readily available. However, the typical requirements and cost of such a setup are remarkably high, concealing the use of OFCs inside the metrology laboratory. New solutions are currently under development to overcome this constraint [65].

An alternative to traditional wide spectral coverage OFCs based on solid-state or fiber lasers are the combs generated by the modulation of a continuous-wave laser with a RF source. Even though the number of spectral components (lines) is more limited, these combs are very convenient for many applications due to its higher power per line, the simple spacing control and far lower complexity and cost. This method for synthetizing OFCs is especially well suited for dual-comb spectroscopy because of the possibility of generating the two combs from a single continuous wave laser removing the need for inter-comb synchronization. In this chapter, different dual-comb architectures for robust and fast operation are presented with the main aim of paving the way to the use of combs in spectroscopic instruments out of laboratory environments.

In connection to the previous chapter, even though OFCs can only perform measurements at discrete wavelengths, these points can be continuously monitored achieving in this way far higher speeds of operation than those of methods based on tunable sources. Likewise, the accuracy with which spectral features can be measured using OFCs, given that the

separation between the lines of the comb can be referenced to a frequency standard, is far higher than the accuracy that can be achieved with any other method.

In this third chapter of the thesis, a multiheterodyne architecture based on a coherent dual-comb source generated by the electro-optic modulation of a single continuous wave laser for fast molecular dispersion spectroscopy is presented. While keeping the same characteristics of the dispersion based approaches presented in the previous chapter, the scheme takes advantage of the parallel simultaneous characterization of multiple spectral points to offer an improvement by several orders of magnitude of the output data rate of current tunable laser based gas analyzers. Moreover, the architecture exploits the measurement of dispersion together with the coherence between the repetition rates of the two combs and the acquisition hardware to eliminate any reference optical path used by current absorption-based architectures, greatly simplifying preceding setups (paper [C]).

Besides this, and based on the advancements in the development of the multiheterodyne molecular dispersion spectroscopy architecture previously introduced, a second dual-comb setup for fast and robust spectroscopy and optical device characterization is also presented. In this architecture the placement of the gas sample has been taken out from its traditional location allowing for stable and robust operation without reconfiguration independently of the sample or the optical path length to characterize (paper [D]).

In the next section, the main concepts of OFCs are introduced together with dual-comb spectroscopy. Then the combs generated by the modulation of a single laser are introduced. Subsequently, the multiheterodyne architecture based dual-comb source generated from a single continuous wave laser for fast molecular dispersion spectroscopy is presented. After that, a second dual-comb setup for fast and robust spectroscopy and spectral characterization is also presented. The chapter ends with some conclusions.

3.1 OPTICAL FREQUENCY COMBS

The first optical frequency comb based on a mode-locked Ti:sapphire femtosecond laser was demonstrated in 1998 by the group of Prof. Theodor

W. Hänsch [66]. This work was soon followed by the first absolute optical frequency measurement using an OFC [67] with an improvement in the accuracy of more than an order of magnitude over previous optical measurements. These results triggered an authentic transformation in the field of high-precision optical metrology where the high potential of OFCs soon overshadowed classical optical sources like tunable lasers and blackbody emitters [68–70]. One of the most important particularities of OFCs is that the frequency of each one of the optical components can be exactly known (with respect to an atomic clock reference). This section is not intended to be a thoroughly revision of OFCs but just a brief introduction to the main characteristics and concepts of these sources. There is a good number of review papers covering in depth the notions here introduced [71–74].

As it was previously said, the main characteristic of an OFC is a spectrum consisting of equally spaced optical tones (also known as lines or teeth). The number of spectral components may vary between tens of thousands for combs based on femtosecond fiber lasers to a few tens for combs generated by the modulation of continuous-wave lasers. Nonetheless, as it is shown in Fig. 3-1, independently of the number of modes, the comb is characterized by the repetition frequency (f_{rep}) and the offset frequency (f_{off}).

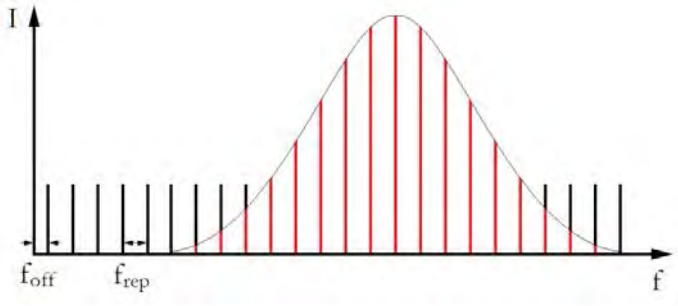

Fig. 3-1. Spectrum of an optical frequency comb.

The repetition frequency can be defined as the separation between optical tones and it is perfectly equal throughout the spectral range of the comb. Meanwhile, the offset frequency is the frequency of the lowest possible comb mode that will be obtained by extrapolating the comb spacing to the lower range of frequencies. In combs generated by mode-locked lasers, the repetition frequency is roughly equal to the inverse of the

round trip time of the cavity of the laser and the mismatch between the phase and group delays of propagation inside the cavity introduces a shift in phase between consecutive pulses that results in the offset frequency. Fortunately, there are different techniques that make possible to measure and stabilize f_{rep} and f_{off} with respect to a certain frequency reference. Therefore, the optical frequency of each of the teeth of the comb can be determined as:

$$f_n = f_{off} + nf_{rep} \tag{3-1}$$

where f_n is the frequency of the n^{th} mode. It must be noted that the comb spectrum of Fig. 3-1 is only represented by the red tones, while the black ones correspond to the extrapolation of teeth to lower frequencies.

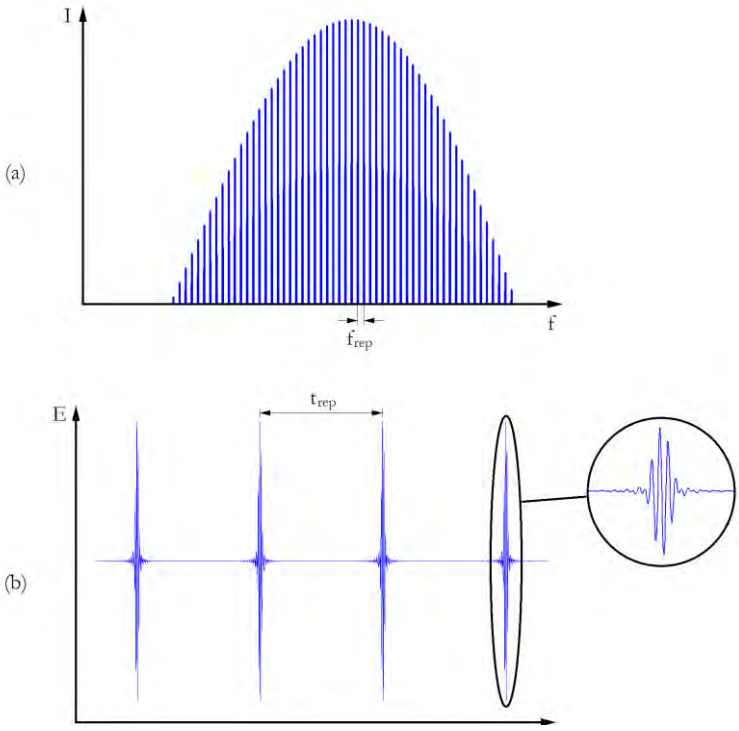

Fig. 3-2. Correspondence between (a) the frequency domain spectrum and (b) the time domain signal of a frequency comb.

It is well known that a frequency domain representation like that of an OFC corresponds in the time domain to a train of pulses. As an example, in Fig. 3-2 (a) the spectrum of an ideal Gaussian shaped comb is shown together with its time domain equivalent (Fig. 3-2 (b)). The time domain electric field of the optical signal consists on a train of short pulses equally spaced in time. The separation between pulses is named repetition rate (t_{rep}) and it is equal to the inverse of the repetition frequency. Hence, in a comb with high separation between pulses the optical tones will be widely spread and vice versa. In the same way, the pulse width of the comb is inversely related to the spectral bandwidth, and therefore ultra-short pulses must be obtained if an ultra-wide comb is to be generated. For these reason, in order to obtain combs with an exceptional spectral coverage, femtosecond lasers are very often compressed in highly nonlinear fiber [75].

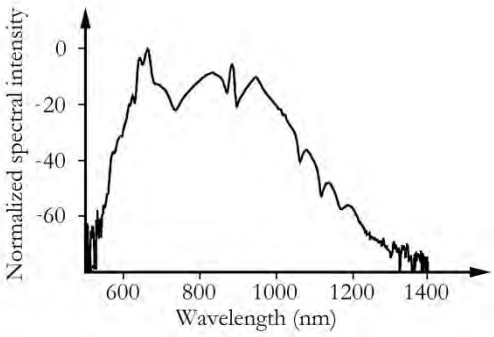

Fig. 3-3. Normalized spectral intensity of a Ti:Sapphire comb generator [76].

As it was previously stated, the stability of a comb is threatened by several noise sources that cause both the stretching and drift of the optical modes. Therefore, it is necessary to lock in phase the repetition frequency and the offset frequency to a frequency reference. In this way, the optical modes are coherent in phase not only with each other, but also with the reference [77], and their absolute frequency can be unambiguously determined. The repetition frequency can be easily monitored by the beating of the comb modes on a photodetector with adequate bandwidth; so it is possible then to use this measurement to control the cavity length, stabilizing in this way the repetition rate of the source. Even though other detection schemes are possible, if the OFC spans more than an octave, the offset frequency can be obtained by heterodyning the frequency-doubled n^{th}

mode of the lower range of frequencies with the $2*n^{th}$ mode [78]. This procedure is known as self-referencing and allows the stabilization of the comb by acting over the pumping power of the laser source [79] (others stabilization methods have also been demonstrated [80]).

Although OFCs can be implemented in various ways, the Ti:Sapphire femtosecond lasers were the firsts to spark a number of comb based demonstrations [72,81,82]. These combs synthesizers are based on a Titanium doped Sapphire crystal with an optical path length of a few millimetres that is pumped by a 515 nm or 532 nm laser. To obtain pulses of a few femtoseconds in duration, the optical cavity must be designed for Kerr lens mode-locking operation [83,84] and the group delay of the crystal must be compensated using chirped mirrors [85] or dispersion-compensating prisms [86]. The spectrum of a Ti:Sapphire femtosecond laser [76] is shown in Fig. 3-3. An external microstructure fiber can also be used for further spectral broadening [87,88].

Despite the superior performance of Ti:Sapphire femtosecond laser based OFCs in comparison with other types of comb generators, the setups are complex and hard to operate, and the cost of implementation is remarkably high. Erbium fiber laser based frequency combs reduce the size and cost and increase the robustness of Ti:Sapphire sources, and can be implemented in an all-fiber ring cavity [89] emitting with a wavelength range centred at 1500 nm. The basic schematic of fiber laser OFCs consists of an optically pumped Er-doped optical fiber that is placed within a closed loop forming an optical cavity [90,91]. As before, in order to stabilize the comb, the offset and repetition frequencies must be monitored and stabilized in relation to a frequency reference. The control of the pumping current of the fiber allows the lock of the offset frequency, whereas the use of an intracavity piezoelectric transducer to adjust the cavity length allows to stabilize the repetition frequency [92]. The spectral coverage of the synthesizer can be increased by the use of large mode fiber and highly nonlinear fiber [75].

3.1.1 Dual-optical frequency comb spectroscopy

As a difference with tunable lasers, OFCs need a spectral interrogation technique for the measurement of the spectrum. Traditional detection architectures are possible, like diffraction gratings to separate in space the different modes of the comb and a CCD to capture its intensity [93]. A

second detection method that has also been exploited in combs spectroscopy [94] is based on the use VIPA spectrometers [95,96] that consists on a solid etalon that vertically diffracts the comb light before it reaches the diffraction grating. However, dual-comb spectroscopy is a far more powerful detection method that makes possible to take advantage of the full accuracy and resolution of the combs and it is based on two OFCs with slightly different repetition frequencies.

Dual-comb spectroscopy was proposed by Schiller in 2002 [63] and the first experimental demonstration was performed by Keilmann et al. [64] two years later. In the basic setup of a dual-comb system that is shown in Fig. 3-4, one of the combs is sent through a gas sample and then combined with the second comb (known as the local oscillator and that has a repetition frequency slightly different from that of the measurement comb). Both optical combs are heterodyned on a photodiode and this results in a comb of radio frequency beat notes that can be digitized. In this way, each of the optical modes is individually mapped into de RF domain where high performance signal processing tools and methods are available. It is then possible to obtain the amplitude and phase of each of the optical teeth of the comb that have travelled through the gas sample in relation to the local oscillator obtaining thus the spectral response of the sample. A second detector is also included to obtain a reference measurement that is mainly used for amplitude and phase normalization, allowing to compensate any fluctuations in the spectral shape of any of the combs.

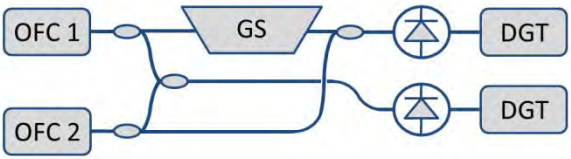

Fig. 3-4. Block diagram of a dual comb spectroscopy setup. OFC, Optical frequency comb; GS, Gas sample; DGT, Digitization.

The one to one frequency mapping property of dual-comb spectroscopy is illustrated in Fig. 3-5. The two optical combs must have the same offset frequency and marginally different repetition rates. In this way, when the combs are combined and heterodyned on a square law detector an array of beat notes is generated with the resultant one to one frequency downshifting. The most extended approach is to directly digitize the radio

frequency comb before performing a Fourier transformation that yields the amplitudes and phases of each of the teeth of the measurement comb.

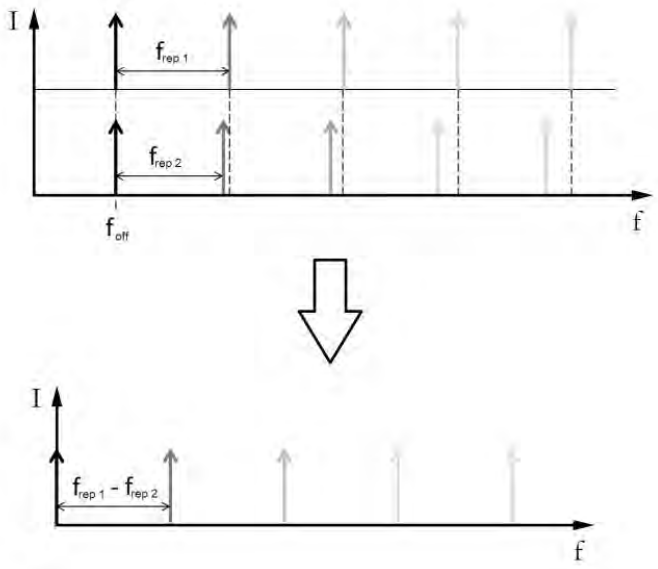

Fig. 3-5. Frequency mapping between the optical and radio frequency domains. A RF comb is generated as a result of the heterodyning between two combs with slightly different repetition frequencies.

The fundamentals of operation of dual-comb systems are exceptionally simple and the full accuracy of the combs has been probed with this method [97]. Nevertheless, many difficulties appear in its implementations and most of them are related to the synchronization between the two optical combs. Given that it is necessary to have good stability between the combs during the integration time of the measurement, the two OFCs must be locked to a common highly stable reference. For example, in a recent demonstration [92], a couple of continuous wave lasers stabilized to a single high-finesse cavity using the Pound-Drever-Hall lock method [98] were employed as the common reference. The beat notes between the couple of reference lasers and the combs were used to individually phase lock the offset and repetition frequencies of the two combs. All in all, despite the complexity of implementation, the extraordinary potential given to dual-comb by exactly

known optical frequencies that are mapped into the RF domain has been demonstrated in many works by different groups [99–104].

Even though dual-comb spectral interrogation setups are equivalent to the interrogation performed with an interferometer of FT-IR instruments [105], there are several differences that are worth mentioning. The complexity of implementation of dual-comb based systems is a disadvantage with respect to traditional FT-IR setups. Moreover, the requirements for phase stabilization between two OFC are very high, limiting, almost exclusively, the applicability of dual-comb to a laboratory. On top of that, the spectral coverage of OFCs nowadays is limited to a few THz, far below the common coverage attainable by FT-IR systems. In the other direction, the accuracy in the estimation of the optical frequency of FT-IR setups is improved by up to 8 orders of magnitude by dual-comb demonstrations [106]. And also very importantly, dual-comb schemes have no moving parts, simplifying the alignment and increasing the robustness of the instrument and providing resolutions that are far from those of state of the art FT-IR spectrometers.

3.2 OPTICAL FREQUENCY COMBS GENERATED BY THE MODULATION OF A SINGLE CONTINUOUS WAVE LASER

The demands in terms of complexity of implementation and operation of OFC generated from mode-locked pulsed lasers are remarkably high in terms of stability and environment control, complexity and cost. This factor restricts the applicability of this kind of sources beyond laboratory demonstrations, leaving space for tunable lasers and other emitters for the implementation of optical sensors in industrial, biomedical or environmental applications. Nevertheless, a new interesting approach for field spectroscopic applications is to use simple OFCs generators based on the modulation of a single continuous wave laser [107]. It is well-known that for many potential applications a level of operation as high as that of traditional OFCs is not needed, and the demands of many systems can be completely fulfilled with much lower levels of performance and characteristics that are in line with the requirements [77]. This prevents the use of combs based on mode-locked pulsed lasers in many applications and opens the possibility for

much simpler OFCs generated by the modulation of a single continuous wave laser [108].

Electro-optic modulators have become in the last years an interesting option for its use as OFC generators. On top of that, recent advances in electro-optic $LiNbO_3$ waveguide modulators [109,110] have lowered the driving voltages and increased the modulation frequency range, and new architectures have even made possible the obtaining of ultra-flat combs [107]. An alternative to the classical Ti:Saphire and Er-doped fiber OFCs that were presented in the previous section are thus the combs generated by the non-linear modulation of a continuous wave laser with a stable RF source. This modulation creates equidistant sidebands (with a separation equal to the modulation frequency) that are perfectly locked in phase with the RF source. Therefore, the repetition frequency is equal to the modulation frequency whereas the offset frequency is dependent on the emission wavelength of the laser.

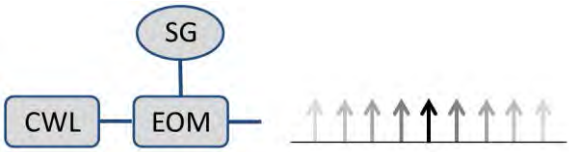

Fig. 3-6. Basic setup of an OFC generator based on modulating a continuous wave laser. CWL, Continuous wave laser, SG, Signal generator, EOM, Electro-optic modulator.

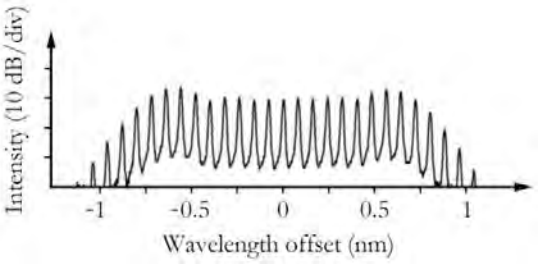

Fig. 3-7. Spectrum of an OFC generated by modulating a continuous wave laser with a single asymmetrically driven Mach-Zehnder modulator [107].

The basic setup of a frequency comb generator based a continuous wave laser and a $LiNbO_3$ modulator is shown in Fig. 3-6. The light of the

laser is directly launched into an electro-optic modulator that is driven at high power by a signal generator. The output of the modulator is a frequency comb that consists on a central tone and a number of upper and lower sidebands equally spaced with a separation equal to the modulation frequency. Therefore, it is possible to get an OFC with a number of teeth that ranges between just three and several tens. The main disadvantage of this kind of generation is the reduced spectral coverage in relation to classical combs. As an example in Fig. 3-7 the spectrum of a OFC generated by modulating a continuous wave laser with a single asymmetrically driven Mach-Zehnder modulator [107] is shown. It must be noted that a combination of several electro-optic modulators or pulse shaping methods can be used to greatly expand the spectral range of the combs. In this way, it is possible to generate combs with a spectral coverage of up to 20 nm with a 3.5 dB variation in the amplitude of the teeth and 60 nm with variations of 10 dB [111].

The combs generated by modulating continuous wave lasers have thus a reduced spectral coverage when compared to other Ti:Sapphire or fiber comb implementations. Nevertheless there are several noticeable benefits of using this technology: the complexity and the cost of these architectures are far lower than the cost of mode-lock laser-based combs what also results in extra robustness and easiness of operation. The spacing between optical modes, for instance, is not controlled by the length of a cavity but just by the radio frequency signal that drives the modulator. Besides this, a sensitivity limiting factor like the power per spectral component is also higher in combs generated by modulating continuous wave a laser.

3.2.1 Dual-comb spectroscopy based on a single continuous wave laser

As it was said before, the high stability required for the operation of classical OFCs extremely limits its applicability to a laboratory environment in which environmental conditions are precisely controlled. An important line of work is now under progress with the aim of overcoming these limitations. A recently published paper by Sinclair et al. [65] demonstrates a comb capable of being operated under vibration with linewidths in the Hz-level. However, the implementation of a field-deployable dual comb spectrometer is far more challenging because of the extra difficulties of locking together two optical combs. In fact, and also in a pretty recent work,

Ideguchi et al. [112] have proposed a change in approach in which a dual comb spectrometer based on two free-running OFCs and adaptive electronic signal processing is demonstrated. This technique could bring classical dual-comb systems a step closer to field applications. However, much further investigation is needed and it is not clear when a field-deployable dual-comb sensor based on mode-locked lasers will be available. By contrast, using combs generated by electro-optic modulators, it is possible to easily generate a dual OFC source from a single laser as shown in Fig. 3-8.

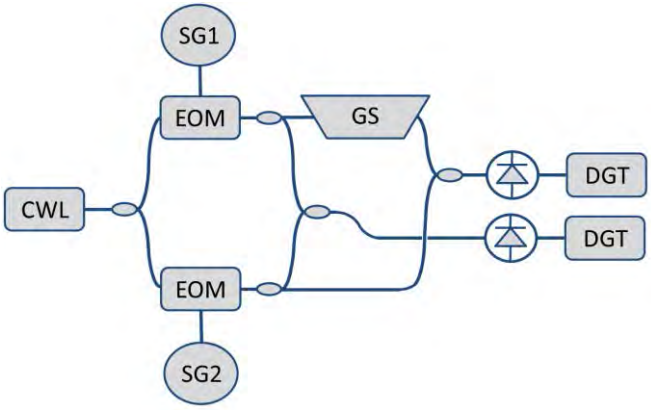

Fig. 3-8. Block diagram of a dual comb spectrometer based on a single continuous wave laser source. CWL, Continuous wave laser, SG1, Signal generator at frequency f_1, EOM, Electro-optic modulator; GS, Gas sample; SG2, Signal generator at frequency f_2, DGT, Digitization.

Even though the setup for a dual-comb spectrometer based on a single laser might look similar to that of classical combs, the level of complexity and cost is by far much lower. As optical source just a laser and two electro-optic modulators are used instead of two synchronized highly stable OFC sources. Therefore, the need of synchronization is removed, any fluctuations in the laser are self-compensated [113] and, consequently, highly stable spectrometers can be obtained. In the same way, the repetition frequency can be easily controlled by changing the frequency driving the modulators and the offset frequency is, on the other hand, given by the wavelength of emission of the laser. For dual-comb instruments, these frequencies will have a slight difference in their values to enable the beat notes between

corresponding optical modes to be mapped from the optical into the RF domain where can be acquired to read the amplitude and phase information.

It is worthwhile to note that to compensate from variations in factors like the temperature of the modulators that can influence the spectral distribution of intensity of the teeth of the combs, a reference optical path is commonly used, as shown in Fig. 3-8. This arrangement makes possible the normalization of the measurement for the compensation of any spectral variations that could affect the results.

In the multiheterodyne architecture for fast molecular dispersion spectroscopy that is presented in the next section this classical scheme has been further simplified by taking advantage of the opportunities that emerge from using dispersion based methods. The reader is referred to the section 6.3 of this thesis for the full paper.

3.3 DUAL ELECTRO-OPTIC OPTICAL FREQUENCY COMBS FOR MULTIHETERODYNE MOLECULAR DISPERSION SPECTROSCOPY (PAPER [C])

As it was repeatedly stated in the two previous chapters, dispersion molecular spectroscopic methods are based on detecting, instead of absorption, variations in the refractive index that occur in the vicinity of molecular transitions. For that it is necessary to measure the phase shift induced on optical waves propagating through the gas in the spectral range of interest. The HPSDS method presented in paper [A] exploits this measurement of phase to provide (unlike absorption based approaches) inherent immunity to baseline and normalization problems that results in robustness to optical power fluctuations. Besides this, the dependency between gas concentration and the change in the index of refraction is linear enabling higher dynamic ranges. That method is based on a monochromatic tunable laser source that sweeps the spectral line of interest while monitoring the phase shifts induced in the optical wave by the change in the index of refraction associated to the molecular transition. Therefore, the sweep time of the laser and the corresponding integration times in detection imply a limit in the speed of operation of the gas analyzers. Such limitations

in the speed of operation might be overcome by using a dual-comb approach that enables the parallel measurement at multiple discrete wavelengths. By its simplicity and spectral coverage, OFCs generated by modulating a continuous wave laser are the most suited comb synthesization method to employ in this scenario.

In this section, a multiheterodyne architecture based on a coherent dual-comb generated by the electro-optic modulation of a single continuous wave laser for high-speed molecular dispersion spectroscopy presented in paper [C] is introduced. Phase modulators are employed instead of the amplitude modulators used in previous demonstration almost doubling, as a result, the spectral coverage of the sensor. The use of phase-lock RF oscillators for the generation of the OFCs and the acquisition hardware together with the phase-sensitive scheme makes possible the operation of the analyzer without any reference optical path greatly simplifying previous architectures. Besides this, the multi-heterodyne parallel measurement design allows for increased speed of operation in comparison with current tunable laser based gas detectors.

3.3.1 Multiheterodyne molecular dispersion architecture based on a dual-comb optical source

The proposed electro-optic dual-comb architecture for high-speed multiheterodyne molecular dispersion spectroscopy is shown in Fig. 3-9. The only laser diode that is used in the setup is connected directly to the two phase modulators to generate the two combs that interrogate the sample. The electrical field of the teeth of the comb after travelling through the sample is described by (refer to paper [C] for more details):

$$\mathrm{E}_n = \mathrm{A}\cos(2\pi(\,\mathrm{f_c} + n\,\mathrm{f_{PM1}})t - \varphi_n) \tag{3-1}$$

where $\mathrm{f_{PM1}}$ is the repetition frequency of the comb and φ_n is the phase of the n^{th} mode that is a function of the refractive index of the sample $n(f)$:

$$\varphi_n = \frac{2\pi(\,\mathrm{f_c} + n\,\mathrm{f_{PM1}})\,L}{c}[n(\mathrm{f_c} + n\,\mathrm{f_{PM1}}) - 1] \tag{3-2}$$

When this comb is combined with the LO comb and heterodyned on a square law detector the measurement comb is mapped into the RF domain maintaining the phase shift introduced by the spectroscopic sample:

$$I_n \propto \cos\left(2\pi\left(f_{AOM} + n\,(f_{PM1} - f_{PM2})\right)t - \varphi_n\right) \qquad (3\text{-}3)$$

Therefore, the RF comb can be synchronously digitized and processed by a parallel multi-channel lock-in detector to yield the phase of each of the teeth of the comb and from this the refractive profile of the sample.

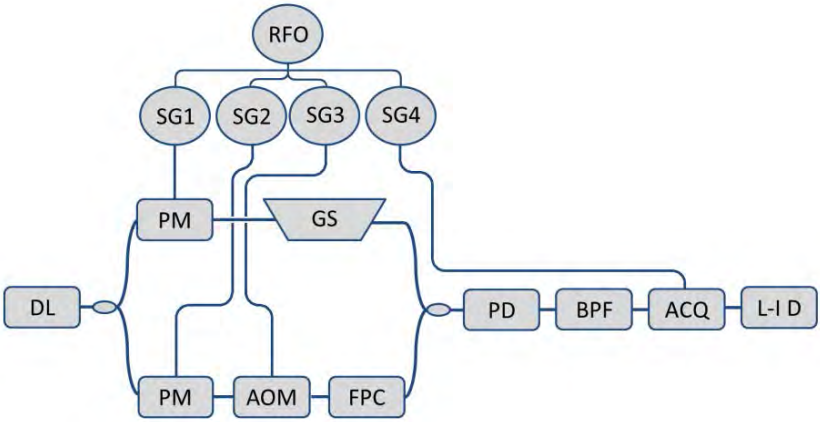

Fig. 3-9. Detailed block diagram of the multiheterodyne DC analyzer. RFO, Reference frequency oscillator; SG1, Signal generator at frequency f_{PM1} ; SG2, Signal generator at frequency f_{PM2} ; SG3, Signal generator at frequency f_{AOM}; SG4, Signal generator for the acquisition clock; LD, Laser diode; PM, Electro-optic phase modulator; GS, Gas sample; AOM, Acousto-optic modulator; FPC, Fiber polarization controller; PD, Photodiode; BPF, Band-pass filter; ACQ, Acquisition hardware; L-I D, Multi-channel lock-in detector. (Fig. 4 of paper [C])

The phase coherence between the repetition rates of the combs and the acquisition hardware (obtained by locking in phase all the oscillators involved in the setup) ensures the proper performance in recovery the optical phase. This phase lock between optical teeth allows for a wavelength step phase calibration procedure that is used to normalize the measurement of dispersion eliminating the reference optical path of previous architectures and increasing the robustness of the sensor. As presented in paper [C], another difference with previous setups is a design oriented for fast data

acquisition, instead of performing semi-static characterizations. For that purpose, the integration time of the multi-channel lock-in amplifier that is used to measure the phases have to be minimum and that can be obtained by increasing the separation between the repetition rates of the two OFCs.

3.3.2 Dual-comb data acquisition and analysis

Due to the lack of space, some of the details of the architecture and the detection method for multiheterodyne dispersion spectroscopy presented in paper [C] were not addressed in detail and will be discussed in more depth in this section.

In Fig. 3-10 a block diagram of the design of the multi-channel detector is presented. The digitized signal (RF comb) is processed in parallel by n channels (99 channels were implemented in the experimental validation) of a lock-in detector. Even though the structure of all the channels of the detector is exactly the same, the reference frequencies ($f_{1\ldots n}$) of the digital signal generators are different. These reference frequencies are configured at values equal to those of the teeth of the RF comb enabling the parallel monitoring of the phase of all the modes. The input signal is independently multiplied by the cosine and the sine of the reference frequency of each channel yielding two signals that are low-pass filtered. The two low-pass filters of the channel control also the integration time of the detector, data arrays are extracted from the input signals with a temporal length equal to the integration time. These arrays are then averaged (averaging is equivalent to low pass filtering) yielding the in-phase and quadrature (I and Q) components of the corresponding tooth of the comb. The last block of the channel calculates the final phase as the arctangent of the quadrature term divided by the in-phase term and assigns the right quadrant in each situation. In this way, the parallel approach can simultaneously extract the phase of each of the optical components of the measurement comb.

With this data acquisition and processing architecture the measurement speed obtained (10 ms) improves previous dispersion spectroscopic implementations. For example, a recently proposed dual-comb scheme also based on electro-optic OFCs [113] reported a measurement time of 30 s for a similar number of spectral lines. In comparison also with current molecular dispersion spectroscopic techniques based on tunable lasers, different CLaDS measurements have been carried

out with integration times of 1 s [54] and 10 s [53] for laboratory demonstrations and 37.5 s for field measurements [53]. The validation of the optical heterodyne CLaDS architecture of paper [B] was performed with an integration time of 1 s and also the HPSDS sensor of paper [A] had 1 s configured. Therefore, the approach proposed on paper [C] improves by two to three orders of magnitude the speed of previously developed techniques and setups.

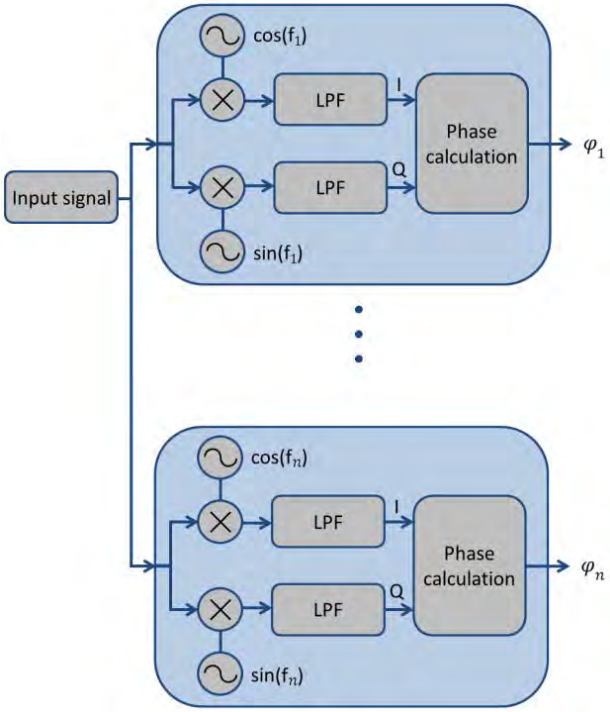

Fig. 3-10. Block diagram of the multi-channel lock-in phase detection scheme. LPF, Low-pass filter.

3.3.3 Experimental validation

The experimental validation of the setup was performed using the spectral line of HCN at 1544.51 nm. For repetition rates of 500 MHz and 500.1 MHz and an AOM of 40 MHz the results obtained are presented in Fig. 3-11 together with the spectral fit of the data for an integration time of 10 ms. The average SNR of the setup in the measurement of the transition of HCN at 1544.51 nm is 35 dB*$Hz^{-1/2}$ resulting in an estimated detection limit of 17.5 ppm*m/$Hz^{1/2}$. The extrapolation of these results to the stronger absorption features of methane in the 1650 nm region will result in a resolution of approximately 1 ppm*m/$Hz^{1/2}$, a figure that improves those obtained by classical [61] and optical heterodyne [114] CLaDS sensors and that of the first HPSDS demonstration [56].

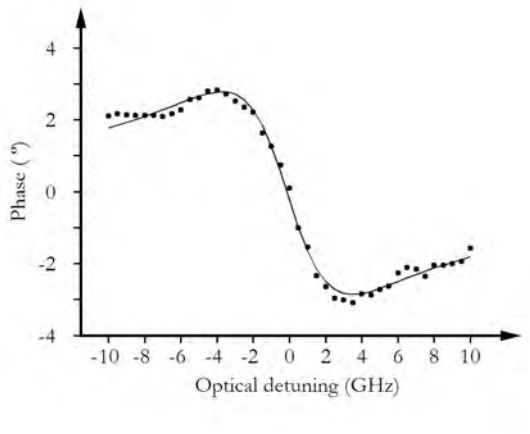

Fig. 3-11. Measurement of the phase shift induced by the spectral feature in the teeth of the comb as a function of the optical detuning (dots). The continuous line represents the fit of the results. (Fig. 5 of paper [C])

3.4 DUAL COMB ARCHITECTURE FOR ROBUST FAST SPECTROSCOPIC MEASUREMENTS AND SPECTRAL CHARACTERIZATION OF OPTICAL DEVICES (PAPER [D])

In this section, an absorption-based compact and robust design of a dual comb spectrometer based on two combs generated by modulating a single continuous wave laser for fast spectroscopic measurements and spectral characterization of optical devices, that was presented in paper [D], is analyzed. The full paper can be found in section 6.4. As a difference with the previously presented setup, this architecture is devised for the robust measurement of absorption. Due to the architecture of the instrument, robust and fast operation is achievable independently of the gas sample, optical device or optical path length to characterize. The architecture takes advantage of the simplicity of a dual comb setup based on the modulation of a single laser. Therefore, the sensor has simple comb configuration and control, high power per spectral component and high source stability.

One of the most important contributions of this paper is that the sample or the optical device to characterize has been taken out of its traditional location in one of the interferometric branches of the instrument (Fig. 3-8) and placed after the recombination of the combs, providing robust operation independently of the optical path or temporal stability of the sample. Furthermore, a parallel multi-channel lock-in detection scheme has been included improving the speed and the SNR of the system.

3.4.1 Multipurpose dual comb setup for spectroscopy and spectral characterization

The block diagram of the general purpose dual-comb spectrometer presented in this section is shown in Fig. 3-12. It is worthwhile to note that instead of the dual optical path of the classical architecture of Fig. 3-8, the instrument proposed in paper [D] uses an optical reference for the normalization of amplitude that is taken after the recombination of the two combs.

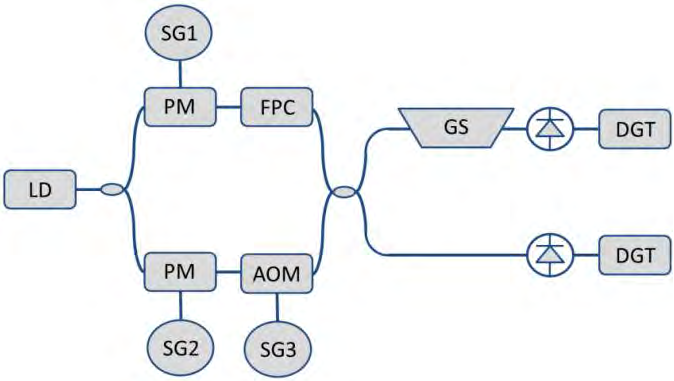

Fig. 3-12. Block diagram of the general purpose dual-comb spectral characterization setup. LD, Laser diode; PM, Electro-optic phase modulator; FPC, Fiber polarization controller; AOM, Acousto-optic modulator, SG1, Signal generator at frequency f_{PM1} ; SG2, Signal generator at frequency f_{PM2} ; SG3, Signal generator at frequency f_{AOM} ; GS, Gas sample; DGT, Digitization. (Fig. 1 of paper [D])

Any mismatch in the optical path lengths of the two branches of the interferometer will cause the appearance of the phase noise of the laser in the frequency of the beat notes. Therefore, the difference in the length of different component avoids the implementation of a multipurpose dual-comb device with a traditional architecture. In the scheme proposed in this section, the two interferometric branches are first combined and then sent through the sample, being possible to precisely minimize the optical path differences of the interferometer to optimize the SNR. After the combination of the two combs, the resulting optical signal can be used (together with the reference) for the characterization of any optical device independently of its length without degradation in the noise isolation of the sensor.

3.4.2 Data acquisition and analysis

The block diagram of the detection setup used in the experimental validation of the architecture of paper [D] is shown in Fig. 3-13. The implementation is similar to that of the detection scheme described in the previous section (paper [C]) but several modifications have been made. The first and most evident is that the channels of the lock-in amplifier detect amplitude instead of phase. Therefore the in-phase and quadrature signals

are squared and added to obtain the amplitude of each teeth of the comb under analysis. Given that the architecture has now a reference optical path for the normalization of the measurement of amplitude, two similar multi-channel detectors are operating in parallel, one for the detection of the measurement comb, and the other for the reference comb (Fig. 3-12). The amplitudes of the corresponding tooth for the two combs are divided for the normalization of the measurement.

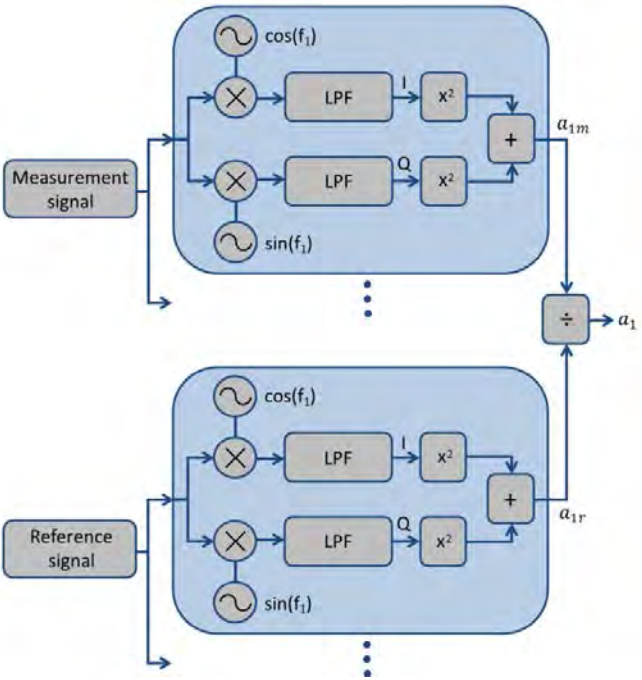

Fig. 3-13. Block diagram of the double multi-channel lock-in amplitude detection scheme. LPF, Low-pass filter.

3.4.3 Experimental validation

As it was presented, in this system the two combs are generated and combined before being sent through the spectroscopic sample or device under test (DUT) ensuring the flexibility and robustness that is needed for a multipurpose spectral analysis instrument. This performance has been validated through the spectral characterization of two different optical targets, the 1544.51 nm transition line of HCN and a Fabry-Perot optical filter (FFP-TF2, Micron Optics Inc., Atlanta, USA), and the results of the measurements are shown in Fig. 3-14 and Fig. 3-15. The fast operation that is enabled by the lock-in detection scheme and the configuration of the combs allows measurements to be taken in 100 μs, providing an output data rate of 10000 measurements per second. In these conditions, the obtained SNRs are 75 $dB*Hz^{-1/2}$ and 70.5 $dB*Hz^{-1/2}$ respectively for the gas sample and the optical filter. It is worthwhile to note that between the measurements of the gas cell and the filter no reconfiguration was made on the system probing the robustness of the spectrometer against any modifications in the characteristics of the sample to characterize.

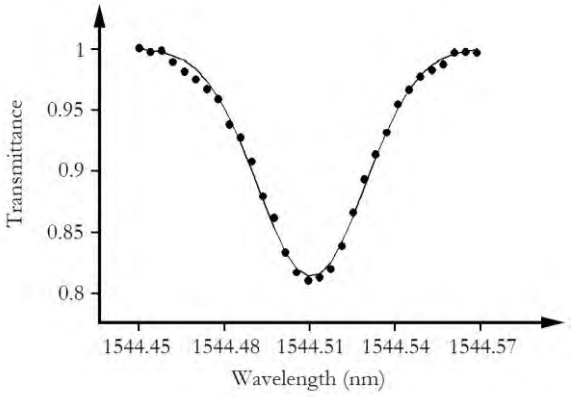

Fig. 3-14. Measurement of the ro-vibrational line of HCN at 1544.51 nm (dots) and the Voigt fit of the results (continuous line). (Fig. 4 of paper [D])

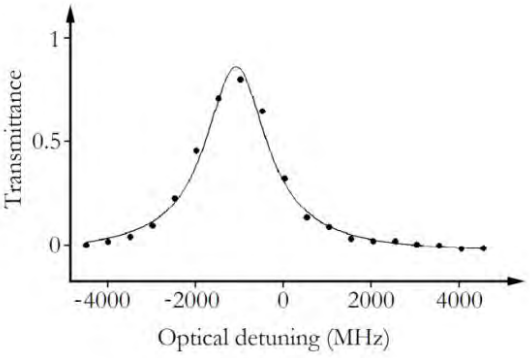

Fig. 3-15. Measurement of the spectral response of a fiber coupled optical filter (dots) and the Lorentzian fit of the results (continuous line). (Fig. 5 of paper [D])

3.5 DISCUSSION OF RESULTS

This chapter discussed the development of new architectures for dual-comb spectrometers based on combs generated by the modulation of continuous wave lasers. Even though these combs provide a narrower spectral coverage than that of classical OFCs, their robustness, low cost and simplicity allow to take advantage of the high potential of OFCs out of the metrology lab.

A new dual-OFC scheme has been first used to increase the speed (in comparison with techniques based on tunable lasers) at which a gas analyzer can operate (paper [C]). Therefore, a multiheterodyne architecture for fast molecular dispersion spectroscopy was presented in section 3.3. The scheme, based on a coherent dual-comb source generated by the electro-optic modulation of a single continuous wave laser, keeps the dispersion measurement approach of the instruments presented in chapter 2 but enables fast multi-wavelength parallel detection. On top of that, the architecture exploits the dispersive measurement and the coherence between the repetition rates of the two combs and the acquisition hardware to eliminate any reference optical path used by current absorption-based architectures greatly simplifying preceding setups. A simple calibration procedure has been established for obtaining of a normalization reference. The main point in favour is of the setup is that (as in many of the

contributions presented in this dissertation) the complexity in the implementation of the dual-comb system is taken from the optical to the electrical domain, where there is almost an unlimited number of tools and techniques available. Also a multi-channel lock-in detection scheme has been introduced. These factors together hugely reduce the complexity and the cost of the setups and provide ease of configuration and robustness of operation.

Besides the dual-comb analyzer for molecular dispersion spectroscopy, a second dual-comb architecture for general purpose fast and robust spectroscopic measurements and optical device characterization has been also developed (paper [D]). A difference in the length of the two optical path of the interferometer in which the two OFCs are generated affects the SNR of the sensor. This is not a problem of the previous multiheterodyne molecular dispersion spectroscopic sensor given that the length of the cavity can be easily compensated. Nevertheless, in a general purpose characterization setup this issue must be addressed. Therefore, in this second architecture the placement of the sample has been removed from its traditional location and a lock-in detection scheme has been included increasing the stability and the robustness of operation of the system.

4. Integration and calibration of a Diffuse Reflectance Spectroscopic system based on Blind signal separation for tissue engineering applications

The contributions that have been presented in the previous two chapters are focused on new spectroscopic techniques and architectures (even though signal processing methods for the obtaining of the spectral information were also proposed) for molecular spectroscopy and spectral characterization. These contributions can be, therefore, located in the left part of the block diagram of a spectroscopic system which was included at the beginning of chapter 1 (Fig. 1-1).

In this fourth chapter, the main contributions are made in the application of spectral analysis methods for information extraction (calibration) to a particular spectroscopic problem, and are, thus, located in the right part of the scheme of Fig. 1-1. To better represent these points, the Acquisition and spectral analysis block has been further expanded in Fig. 4-1. In this way, the output of the spectral technique is acquired and digitally processed to obtain the spectral information of the sample. Most instruments require additional processing steps, like the compensation of the spectral shape of the optical source, of the baseline or the normalization of the measurement, to isolate the spectral profile of the sample. Calibration procedures are then applied for determining the targeted results (like analyte concentrations) from the spectral profile, and finally, these results are presented to the user.

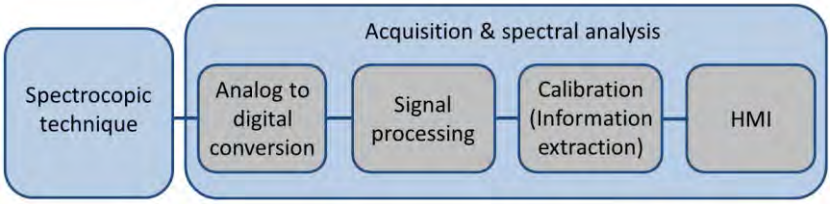

Fig. 4-1. Block diagram of a spectroscopic instrument. The acquisition and spectral analysis subsystem has been further detailed. HMI, Human Machine Interface.

In order to better illustrate the tasks performed by these last components of a spectroscopic system, this chapter presents a study of the application of various spectral analysis methods based on data classification

algorithms to biomedical applications. In the same way, taking advantage of the complete spectroscopic instrument for diffuse spectroscopy that was developed as a platform for performing the study, system integration considerations are also presented.

In the next section, the basics of diffuse reflectance optical spectroscopy for biomedical applications are presented providing the necessary information to place the contributions of paper [E]. In the second section, the biological problem is presented, and the design of the instrument detailed. As justified below, the particularities of the biological problem make it very well suited to the use of data classification methods for the spectral analysis of the measurements. This approach has proved the feasibility of the non-invasive monitoring of bioengineered skin graft substitutes. The chapter ends with a discussion of the results of this work.

4.1 CONTINUOUS WAVE DIFFUSE REFLECTANCE SPECTROSCOPY

In line with the description of the characteristics of optical media of section 1.2, the propagation of light in molecular samples, which has been thoroughly reviewed in previous chapters, is, as it was previously justified, limited by optical absorption. On the contrary, the propagation of light in biological tissues is mainly limited by scattering. This kind of propagation has given rise to a spectroscopic technique like Diffuse Reflectance Spectroscopy (DRS) in which the optical sample is illuminated by a light source with a certain spectral range capturing the back reflected optical intensities from the target (even though other approaches have been presented, this chapter is exclusively focused on DRS). One of the single most important steps in the development of DRS methods for biomedical applications was the recognition of the propagation of light in biological tissues as a diffusive mechanism [115]. The photons entering the medium are randomly diffused thought the volume in consecutive dispersive events, and those photons that are not absorbed will emerge back from the tissue carrying spectral information about any absorber present in the medium.

Due to the low absorption of water within what is called the therapeutic window (from 600 nm to 1100 nm), photons are able to travel long distances into tissues like the human skin. The propagation of light at

the therapeutic window range mainly undergoes scattering events that are caused by, as it was previously said, cells, cell organelles, such as the mitochondria and nuclei, and collagen that allow photons to travel deep into the tissue before re-emerging to the surface. Nevertheless, there is also a small level of absorption that is primarily induced by hemoglobin, melanin, lipid and water. Through the analysis of the diffusively back reflected optical spectrum different parameters like the concentration of absorbers or the structure of the tissue can be assessed [116]. Nevertheless, the estimation of the concentration of analytes is complicated by the presence of different pigments in the skin and the important differences between patients. It must be noted that a more detailed review of the methods for the extraction of information from the back reflected spectral profile in biological tissues is included in Appendix III.

DRS, unlike other existing techniques, makes possible non-invasive in-vivo measurements removing the need to take biopsies from patients that limits highly the applicability of other characterization methods. On top of that, once the tissue has been excised, hemoglobin concentrations for example begin to diverge from physiologic quantities and the hydration level also begins to change [117]. DRS methods overcome these problems allowing for real-time operation whereas avoiding the need of performing a biopsy to the patient. DRS together with different spectral analysis methods have been demonstrated in many different biomedical applications, from the obtaining of quantitative data of tissue oxygenation and blood volume [118], to the characterization of skin hemodynamics [119,120] and the measurement of collagen content [121] and lipids and water contents [122]. Besides this, DRS has been applied to the assistance in diagnosing different diseases, from gingivitis and periodontitis [123] to pancreatitis [124] and the prediction of ulcer healing [125,126] and wound [127] healing. Also, to pigmented skin lesions (including melanoma) [128,129] and breast cancer [86].

4.1.1 Spectral analysis methods for Diffuse Reflectance Spectroscopy

As happens with the analysis of liquids and solids (described in section 1.2), in the analysis of biological tissues the overlapping between spectral features of different analytes makes necessary further spectral analysis processing to obtain the concentrations of the components of interest.

Between the different existing approaches for DRS spectral analysis, one of first method employed was the modeling of the propagation of light in tissues through an analytical expression (this approach is in the same vein that the calibration models based on spectral data information presented in chapter 2). In its application to biological tissues, the Radiation Transport Equation (RTE) [7] provides the basis for the separation of the contribution of different analytes. Nevertheless, it is common to derive the much simpler Photon Diffusion Equation (PDE) [6,8] from the RTE for computing efficiency. Even though, these models have been able of performing remarkably well [118,130,131] for DRS under certain conditions, the complexity of most biological structures and factors like the inter-patient variability make difficult to obtain reliable results in every situation. A different approach related in some way to the analytical modeling of the sample is the Monte-Carlo simulation method [132–134] that has also been widely used for DRS analysis to estimate the concentration of analytes but suffer from the same problems that the analytical solutions (these methods and others are reviewed in more detail in Appendix III). Therefore, the calibration of spectroscopic instruments based on analytical models preforms well in the study of molecular samples, but presents major deficiencies in the application to turbid samples.

A different approach, that has become the standard procedure in most fields of spectroscopy, is the use of multivariate data classification algorithms. Between them, Blind Signal Separation (BSS) techniques provide a distinctive approach to the solution of the inverse problem. The focus is not in the recovery of the optical properties of the sample, but in the identification and quantification of the contributions of the analytes that are present in the medium. BSS techniques are able to recover the individual spectra of several contributors from measurements of their mixes, relying only on the assumption of mutual independence between such contributors. Therefore, regardless of the suitability for the application of a particular solution of an analytical model or the complexity of the structure of the optical media, and even though with some limitations, BSS methods should be able to assess the contributions of the different components that affect the optical spectrum. Unfortunately, it is not always possible to identify the physical meaning of every component and in some situations it is necessary to force the spectrum of an analyte into the algorithms. There are many BSS methods having particular characteristics, nevertheless, in this section Principal Component Analysis (PCA) and Independent Component Analysis (ICA), that will be used later on the chapter, are briefly introduced.

For a thoroughly revision of these methods there are several references available [135–138].

PCA is based on the linear transformation of the measured data from its original coordinate system to an orthogonal coordinate system whose axes correspond to the principal components. Each succeeding principal component is calculated in a way in which accounts for the largest possible variability in the data (maximum variance). Therefore, the dimensionality of the data can be reduced from its original size to the number of uncorrelated contributors to the measurement (this is a highly valuable characteristic of PCA especially when multiple high resolution spectra are under analysis). Recently, PCA has been employed for the classification of multispectral diffuse reflectances in imaging reconstruction [139] and the quantitative evaluation of analytes concentrations [140].

ICA, in a very similar approach, has been developed to separate several sources from the measurement of the mixture of these sources. ICA can separate the spectra of several analytes from the measurement of the combined spectrum and estimate the concentration of the different constituents. This method has also been previously employed with success in different applications [141,142].

In the next section, the application of PCA and ICA methods for the monitoring of the level of angiogenesis on bioengineered skin substitutes in the first days after engraftment is presented. Likewise, the design and integration of the DRS instrument that has been developed as a platform for the spectral characterization of the biological samples are also detailed.

4.2 Integration and calibration of a remote Diffuse Reflectance Spectroscopic instrument for tissue engineering monitoring based on Blind Signal Separation (Paper [E])

The work performed towards the development of a remote, non-invasive DRS demonstrator for performing a feasibility study about the possibility of early monitoring of bioengineered skin substitutes, that was

published in paper [E] (that can be found in section 6.5 for further details), is presented in this section.

Bioengineered skin grafts are covered after surgery by a protective layer that is, very often, a devitalized skin. Therefore, the assessment of the characteristics of the engraftment must be performed with photons going through this protective layer and coming back to the surface. On top of that, the optical properties of the protective layer change within days and this result in a problematic scenario that makes very difficult the application of common PDE solutions or MC simulations. Thus, BSS methods were employed to analyze the data obtained from the measurements performed on a set of skin grafts in which different behaviors were induced. The results validated the viability of the non-invasive remote assessment of the early evolution monitoring of bioengineered skin grafts.

Between the contributions of paper [E], this is, to the knowledge of the author, the first use of DRS for the monitoring of bioengineered skin substitutes. The same applies to the use of data classification algorithms for calibration procedures in tissue engineering applications.

4.2.1 Bioengineered skin grafts

Bioengineered skin was designed to address the need for early coverage of extensive burns. This artificial alternative overcomes the limitations of surface presented by skin autografts and reduces the complications that may occur during the recovery process. A thorough revision of the principles of how bioengineered skin substitutes are designed and manufactured is far from the focus of this chapter (detailed information can be found in refs. [143–145]), however some very basic ideas will be briefly given below. The main component of bioengineered skin substitutes is a fibrin matrix that hosts the dermal cells allowing for blood clotting and cell migration. The fibrin matrixes are populated with fibroblasts for supporting keratinocyte growth and an easy remodeling into collagenous dermal tissue. This design has been created by looking at the wound healing process and, even though the perfect skin substitute has not been achieved yet, it fulfills many of the desired clinical requirements. In fact, the effectiveness in achieving tissue regeneration is now widely acknowledged. Nevertheless, there are still some issues related to the dermal matrix that, if solved, could allow better tissue regeneration and further enhance the performance of skin substitutes.

Researchers from the Regenerative Medicine Unit of the Epithelial Biomedicine Division based at the Centro de Investigaciones Energéticas, Medioambientales y Tecnológicas (CIEMAT), Madrid, Spain have developed a humanized mouse model suitable to the study, development and improvement of bioengineered skin substitutes. This model has already shown its validity for evaluating tissue regeneration [146] and can be considered as a preclinical platform for reproducing the functional and structural characteristics of the human wound healing process. The skin substitution tests involve replacing the skin from the back of a humanized mouse model with the bioengineered skin graft. The skin that has been removed from the mouse model is devitalized through a number of cycles of freezing and thawing and, afterwards, it is placed over the skin graft as a protective layer. The devitalized skin gets dehydrated with the pass of the days and this induces a profound change in its optical properties. Therefore, the visual assessment of the evolution of the engraftment is not viable and only after the devitalized skin is removed (or slough off) typically three weeks after surgery, the state of the skin engraftment can be properly evaluated. The objective of the work presented in paper [E] was to study the viability of the non-invasive monitoring of the evolution of angiogenesis in bioengineered skin substitutes, that could provide valuable information during the first day after engraftment.

4.2.2 Diffuse reflectance spectroscopic sensor for bioengineered skin substitutes monitoring

The basic scheme of the sensor is shown in Fig. 4-2, the setup is divided in three main subsystems, the electronic and optical subsystems and the optical head. The whole design was developed in the Electronic Technology Department of the Universidad Carlos III de Madrid (Spain). The main component of the electronic subsystem is a multipurpose Cyclone III FPGA from Altera (Altera Corporation, California, USA) in which the four Digital Signal Synthesizers (DSS) that generate the modulation signals and a digital four channel lock-in amplifier (this detection techniques has been thoroughly reviewed in previous chapters) are embedded. A Nios II soft processor, also embedded in the FPGA, is used for the control and configuration of the setup and for measurement triggering and data requesting tasks. These operations are performed under request from a Graphic User Interface (GUI) running into a PC that communicates with the FPGA using a RS-232 interface. Besides the FPGA, addition signal

conditioning, acquisition and digital to analog conversion hardware is required. The digital signals of the DSSs are sent to four digital to analog converters that generate the actual analog signals that are used to modulate the amplitude of the four lasers. As it was previously said, the modulation at different frequencies make possible to simultaneously detect the reflectance at each of the wavelengths. The values of frequency (chosen to minimize the cross talk between channels) were 3800, 4500, 5100 and 6000 Hz. On the other hand, the signal from the single photodetector is amplified (with a programmable-gain amplifier) before being digitized by a 12 bits analog to digital converter at 50 MSPS. This signal is then fed to a digital four channel lock-in amplifier that isolates the reflected amplitudes at each wavelength (modulation frequency) yielding a measurement of the diffuse reflectance spectrum of the tissue under analysis.

In a dedicated PCB, connected to the main FPGA using a PCI104 stacking connector, the drivers for the laser diodes have been implemented. The design is based on the LDD driver series from Wavelength Electronics (Wavelength Electronics Inc., Montana, USA) and was optimized for optimum amplitude modulation performance. Apart from the four drivers, a high gain transimpedance amplifier with a filtering stage has also been implemented for the electronic conditioning of the signal captured by single photodiode that is used in the setup. A picture of the main PCB together with the power supply and the PCB of the drivers and conditioning electronics is shown in Fig. 4-3.

Within what can be considered the optical subsystem are the laser diodes and the optical combination. It was decided to cover all the wavelength range of the therapeutic window and four laser diodes with wavelengths of 532 nm, 635 nm, 850 nm and 1064 nm were selected for the application (DJ532-10, Thorlabs Inc., New Jersey, USA and PL63C0053FCA-0-0-01, PL85B0053FCA-0-0-01 and PL10B0053FCA-0-0-01 from PD-LD Inc., New Jersey, USA). The light of the four lasers is combined into the single fiber that guides the optical signal to the optical head using a set of multimode optical combiners (FCMM625-50A, Thorlabs Inc., New Jersey, USA).

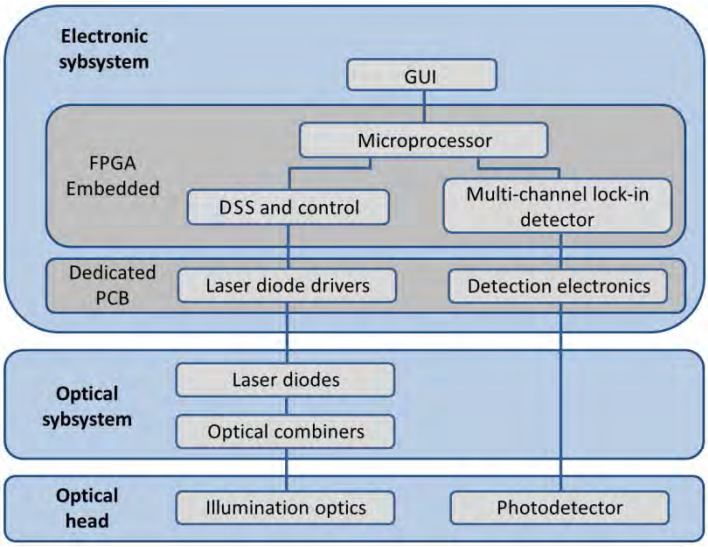

Fig. 4-2. Block diagram of the DRS instrument.

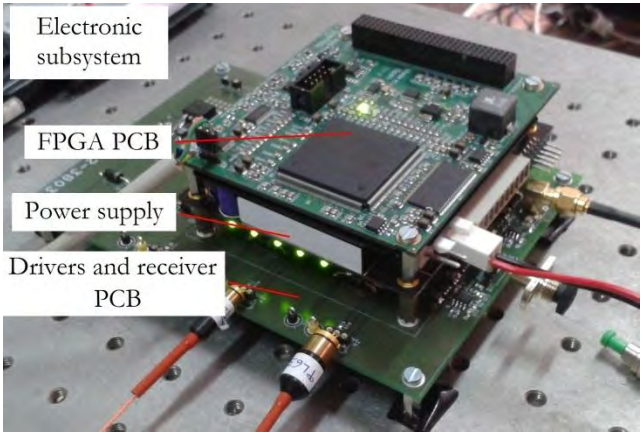

Fig. 4-3. Picture of the electronic subsystem of the spectroscopic system.

Finally, the optical head includes the illumination assembly and the receiver optics. The fiber that carries the light from the lasers is connected to a fiber collimator (F220FC-780, Thorlabs Inc., New Jersey, USA) that concentrated the signal on a spot around 2 mm wide on the surface of the tissue. A polarizer (LPVIS050-MP, Thorlabs Inc., New Jersey, USA) is placed after the collimator to ensure the uniform linear polarization of the illumination signal. Given the spectral range to cover, a silicon photodetector (FDS100, Thorlabs Inc., New Jersey, USA) was used is the collection of the back reflected signal. A second polarizer (crossed with respect to the other) was placed in front of the detector in order to eliminate the reflection from the surface of the tissue. It has been proved that light reflected by the superficial layers of the skin can be differentiated from light backscattered from inner layers [147] using polarization gating. The polarization of photons reflected on the superficial layers of the skin remains unchanged whereas the polarization of photons that penetrate through deeper layers is exponentially randomized due to scattering events [148] and by the birefringence introduced in the tissue by collagen fibers [149]. Therefore, using two cross-polarizers for the illumination and the detection of light reflected from the tissue ensures that only photons that have reached the volume of interest for the experiment are captured.

As said before, after acquisition, the signal is processed to extract the intensities of the reflectances at the four wavelengths of the sensor. This processing is performed taking advantage of a four channel lock-in amplifier detector that is implemented into the FPGA. The design of the intensity detector, that is shown in Fig. 4-4, is different from the design of the detectors of previous chapters. In this scheme an active filtering stage has been included to remove the effect of the interference from the power line or the room illumination in the measurements. On top of that, both amplitude and phase are extracted; the scheme uses the CORDIC method for the measurement of phase.

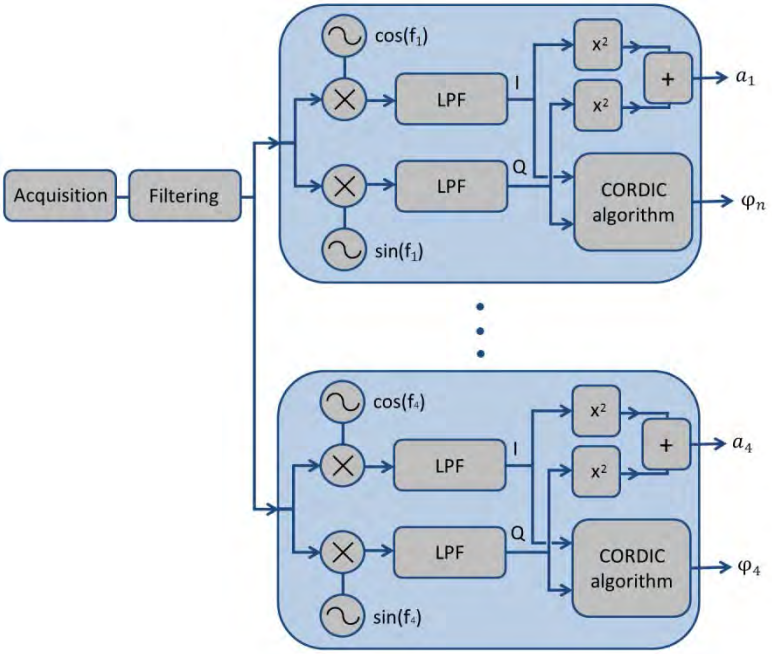

Fig. 4-4. Block diagram of the four-channel lock-in detector implemented in the FPGA. LPF, Low-pass filter.

The control, data triggering and reading of results of the FPGA-embedded lock-in amplifier is performed using a set of function that act as drivers. The calls to these drivers are performed by the user GUI (that it is executed in a PC) via RS-232 interface. A list with the main functions and a short description of their operation is given below:

void mc_lockin_amp_pre_gain(unsigned int gain): Controls the gain of the analog input chain allowing to maximize the resolution of the ADC connected to the FPGA.

void mc_lockin_amp_offset_comp(void): Automatically compensates the input offset of the analog input chain.

void mc_lockin_amp_input_mux(unsigned int input): Selection between the main receiver and a possible auxiliary channel.

void mc_lockin_amp_hp_filter(unsigned int enable): Enables or disables a digital high pass filter designed to eliminate frequencies below 1000 Hz.

void mc_lockin_amp_dds_freq(unsigned int channel, unsigned int freq): Allows to directly configure the frequency of each oscillator.

void mc_lockin_amp_dds_vpp(unsigned int channel, unsigned int vpp): Controls the peak to peak voltage of the modulation signal.

void mc_lockin_amp_dds_offset(unsigned int channel, unsigned int offset): Controls the offset DC level of the modulation signal.

void mc_lockin_amp_dds(unsigned int channel, unsigned int enable): Enables or disables the direct digital synthesizers.

void mc_lockin_amp_acq_time(unsigned int channel, unsigned int time): Allows to set the integration time of each lock-in amplifier.

void mc_lockin_amp_trigger(unsigned int channel): Triggers a measurement in the selected channel.

float mc_lockin_amp_get_module(unsigned int channel): Returns the value of the module of a measurement of a particular channel.

float mc_lockin_amp_get_phase(unsigned int channel): Returns the value of the phase of a measurement of a particular channel.

float mc_lockin_amp_get_input_max(void): Returns the maximum input voltage in the ADC during a measurement.

float mc_lockin_amp_get_input_min(void): Returns the minimum input voltage in the ADC during a measurement.

void mc_lockin_amp_gpio_config(unsigned int port, unsigned int inout): Configuration of the digital input-output pins as inputs or outputs.

unsigned int mc_lockin_amp_gpio_read(unsigned int port): Returns the read of a digital input.

void mc_lockin_amp_gpio_write(unsigned int port, unsigned int value): Allows to write a bit in a digital output.

void mc_lockin_amp_info_reg(void): Returns the contents of all the registers.

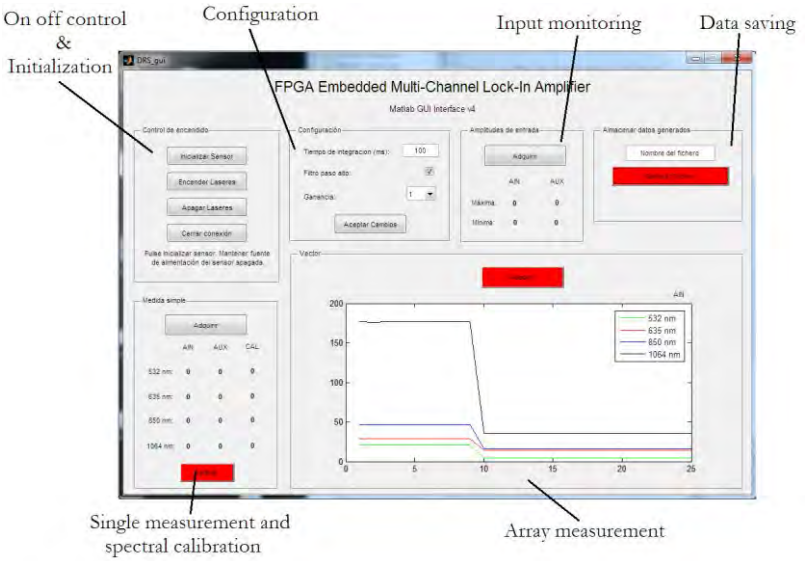

Fig. 4-5. GUI used in the tests. The different control zones are highlighted.

A screen capture of last of the components of the spectroscopic system, the GUI used in the tests, is shown in Fig. 4-5. The GUI was designed to be used for personnel non-trained in optics or photonics systems after a sort introduction of a few minutes. The different control areas of the program have been differentiated, first the on-off control where the instrument is initialized and the lasers can be turned on for temperature stabilization. Then, the configuration block allows the setup of the integration times of the lock-in amplifiers, to enable extra filtering and the control of the gain of the front end. The input monitoring area performs measurements of the amplitude of the input signal to avoid the saturation of the ADC. At the bottom left, the single measurement zone allows the spectral calibration of the setup using a reflectance standard and the array measurement zone is designed to capture data arrays. Finally, data saving stores all the information into and .xls file.

4.2.3 Experimental protocol

As it was previously stated, the main aim of this work is to study the viability of the non-invasive monitoring of the evolution of skin substitutes. This is done through the measurements carried out on a set of skin grafts in which different angiogenesis behaviors (i.e. the strength and speed with which blood vessels appear in the skin substitute) were forced.

Four mice were engrafted with different types of skin substitutes, in two of them a regular bioengineered skin substitute was engrafted, whereas in the other two the keratinocytes of the skin were made to overexpress the VEGF (Vascular Endothelial Growth Factor) protein. Vascularization is expected to appear earlier and in higher proportion in the VEGF-expressing grafts than in the normal grafts. Therefore, changes in the DRS back reflected spectrum should be apparent and give an indication of the state of vascularization of the skin substitute.

The mice with VEGF-expressing grafts were labelled as VEGF1 and VEGF2 and the control mice (with the normal grafts) as CTL1 and CTL2. As it is shown in Fig. 4-6, the measurements performed to monitor the evolution of the bioengineered skin were carried out placing the illuminated spot right in the centre of the grafts. Besides this, measurements on a second control point located at the nape of the mouse were used to quantify the consistency of the instrument.

In Fig. 4-6 it is also possible to appreciate the appearance presented by the circular protective devitalized skin layer placed over the engraftment a few minutes after surgery. By contrast, a picture of a mouse taken seven days after engraftment that is displayed in Fig. 4-7 shows the evident changes that the devitalized skin has suffered, dehydration, wrinkles, and non-uniform shape are evident. This is the main problem that the DRS sensor here developed has to address; it should be able to assess the evolution of the skin substitute that is placed underneath a protective layer that suffers a massive change in its optical characteristics.

The measurements were carried on the four anesthetized mice one after another on days 0, 2 and 6 after grafting. On day 7, biopsies of the engrafted skin were performed to study the vascularization of the tissues. To ensure the consistency of the data acquisition, a set three measurements were performed and averaged in each location.

Fig. 4-6. DRS measurements being carried out on a mouse.

Fig. 4-7. Appearance of the protective skin layer placed over the skin substitute seven days after engraftment.

4.2.4 Spectral data analysis

In the analysis performed in this study the two methods that were presented in the introduction of this chapter, PCA and ICA, have been applied. In particular, principal components and coordinates have been calculated applying the Singular Value Decomposition algorithm and ICA calculations have been performed using the Fixed Point Algorithm for ICA from Hyvärinen [138]. Both PCA and ICA calculations have been made using Matlab (MathWorks Inc, Massachusetts, USA).

As it has been discussed above, the engraftments were measured on the four anesthetized mice on days 0, 2 and 6 after grafting, two of the mice had normal skin substitute grafts and the other two were grafted with VEGF-expressing grafts (in which blood vessels are formed faster and in higher number). After that, on day 7, and in order to study the state of vascularization and structure of the skin substitutes, biopsies were performed in each type of graft. PCA method has been applied directly to these values of reflectance for days 2 and 6. The covariance obtained by the first principal component has been of 92 % on day 2 and 98 % on day 6, therefore it has been considered that only the coordinates for this first principal component are relevant for the separation between graft types. Also, as it was previously found by Kainerstorfer et al. [150], the first principal component presented a tight time consistency, it was practically equal on both days with a small difference of 3.2% between the two calculations.

The PCA analysis performed on day 6 shows a clear difference between coordinates for the first principal component of the mice from each type of graft that is not present on day 2, these results are shown in Fig. 4-8. The coordinates for VEGF1 and VEGF2 are almost equal and clearly separated from those of CTL1 and CTL2. Therefore, even though the sensor is not able to differentiate between graft types on day 2 (likely because not enough time has gone by for physiological differences to appear) it can quite evidently separate the evolution of both types of grafts four days later.

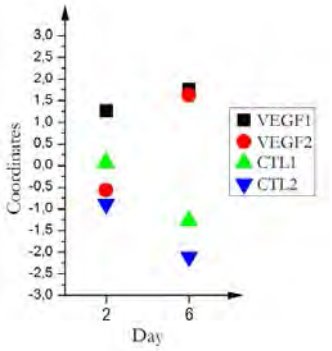

Fig. 4-8. Evolution of the coordinates of the first principal component of the PCA analysis for each mouse for days 2 and 6

In Fig. 4-9 the PCA coordinates for the three principal components on day 6 are plotted. The covariance represented by the first principal component is of 98% and thus it is possible to consider that only this principal component can be used for the assessment of the evolution of the grafts. Therefore, the dimensionality of the data is reduced from the four spectral measurements to the coordinate for the first principal component.

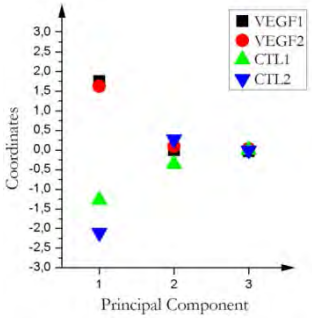

Fig. 4-9. PCA coordinates on day 6 for the three principal components. Note the clear differentiation between graft types for the first principal component.

In addition to the PCA analysis, the ICA method was applied to the mean reflectance values measured at each wavelength for the four mice on days 2 and 6. In this way, three constituent components are obtained for each measurement together with the estimation of their concentrations. One

of the constituent components (identified as constituent component 1) accounts for the highest variability in the results and, as before, the concentrations obtained for this component on days 2 and 6 are plotted in Fig. 4-10. Even though as before no differentiation between graft types is possible on day 2, clear contrast appears on day 6, with values of 0.043 and 0.041 for the VEGF-expressing grafts and 0.123 and 0.102 for the control grafts.

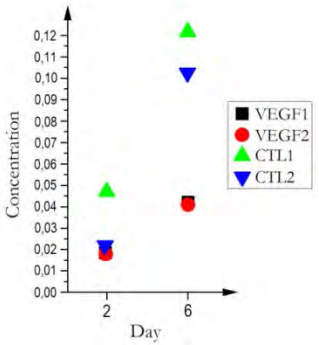

Fig. 4-10. Evolution of the concentration for the constituent component 1 obtained of the ICA analysis for each mouse for days 2 and 6.

The concentrations of the three constituent components obtained for day 6 are shown in Fig. 4-11. In something similar to what happened in the PCA analysis, the first constituent component accounts for almost all the variability in the results while the concentration of the rest of the components is pretty similar. Therefore, the concentration of only one of the analytes (presumably hemoglobin) is differentiating the two types of grafts.

After the measurement process, biopsies of the grafts were taken on day 7, the results of the histology of these tissues are shown in Fig. 4-12 and Fig. 4-13 for the control and VEGF-expressing grafts respectively. The structure of the fibrin dermal matrix is quite similar in both histologies, nevertheless, while only a few small size blood vessels are visible in the control skin substitute, in the VEFG graft ultra wide hemorrhagic blood vessels have been formed. Consequently, in relation to the typical chromophores targeted by DRS systems, the main difference between the

grafts is related to the amount of hemoglobin that can be found within the tissue.

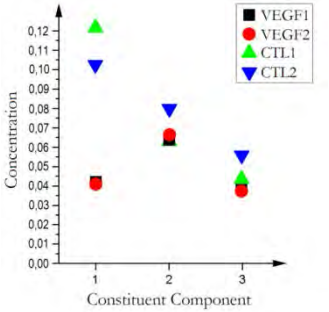

Fig. 4-11. Concentration obtained in the ICA analysis for the three constituent components.

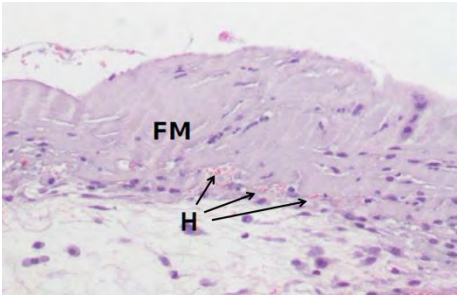

Fig. 4-12. Histological appearance of the control (normal) bioengineered skin substitute seven days after grafting. FM, Fibrin dermal matrix; H, Blood vessel.

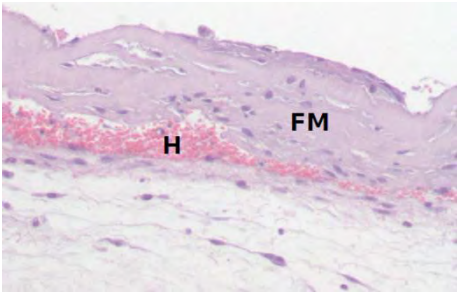

Fig. 4-13. Histological appearance of the VEGF-expressing graft seven days after grafting. FM, Fibrin dermal matrix; H, Hemorrhagic blood vessel.

The differences found on day 6 between the coordinates for the first principal component in the PCA analysis and the concentration for the constituent component 1 in the ICA analysis between the control grafts and the VEGF-expressing grafts are clear in both cases. This is in contrast with inexistence of differences between the coordinates of the rest of principal components and of the rest of constituents. It could therefore be considered that only one of the analytes that are being interrogated shows an important difference in its concentration between the control and the VEGF-expressing grafts. This conclusion is in evident agreement with the results of the histology that probed that the only noticeable difference between graft types was the hemoglobin content. The results of the PCA and ICA analysis also showed that separation on day 2 is not possible mainly because not enough time has passed for any significant change to appear in the grafts.

4.3 DISCUSSION OF RESULTS

As conclusions, in this chapter the multiple laser DRS instrument based on BSS classification algorithms for monitoring the evolution of bioengineered skin substitutes in the first days after engraftment that was proposed and experimentally validated in paper [E] has been presented. The stand-off instrument has been able to non-invasively differentiate between the evolutions of grafts with various states of angiogenesis.

A modulated four-wavelength illumination setup was developed in conjunction with a multi-channel phase-sensitive detection scheme for the synchronous measurement of the diffuse reflectance of the tissue. The particular characteristics of the biological problem to address have driven the use of BSS methods, instead of the analytical approach employed in previous chapters. PCA and ICA were used in the analysis of the measurements with both yielding a clear differentiation between the control and the VEGF-expressing grafts in the concentration of one of the analytes. In this respect, the histology performed to the tissues confirmed that the amount of hemoglobin that could be found in the grafts expressing the VEGF protein was far higher than that of normal grafts. This validates the ability of the set of techniques employed for the assessment of early vascularization of skin substitute grafts.

Besides the previously mentioned contributions, it is worthwhile to note that a complete stand-alone DRS system was implemented for the

study. The instrument was developed at the Electronic Technology Department of the Universidad Carlos III de Madrid and transported to the facilities of the Epithelial Biomedicine Division based at the Centro de Investigaciones Energéticas, Medioambientales y Tecnológicas (CIEMAT). The design of the sensor enabled its operation by personnel non-trained in photonics systems during most of the study.

5. Conclusions

In this thesis, contributions have been made to all of the main components of spectroscopic systems. In the successive chapters of this dissertation, new techniques and architectures for narrow-band spectral characterization based on tunable lasers, dual-comb systems based on electro-optic modulators and novel spectral analysis and integration approaches have been analyzed. The problems associated to the detection and monitoring of molecular samples using absorption based methods have been addressed by new narrow-band architectures for molecular dispersion spectroscopy. In the same vein, several contributions have been made focusing on overcoming the main limitations of current wide-band comb-based systems in terms of cost, complexity and lack of robustness to make possible its use in field instruments. Finally, a sensor based on BSS methods was developed for performing a viability study in which the ability of spectroscopic techniques together with data classification algorithms for monitoring the state of angiogenesis of bioengineered skin substitutes has been probed. These contributions can be placed in the block diagram of a spectroscopic system shown in Fig. 5-1. Therefore, whereas in paper [A] a completely new technique for molecular dispersion spectroscopy was presented, paper [B] was focused on a novel detection scheme for CLaDS sensors. Papers [C] and [D] proposed new spectroscopic architectures and signal processing techniques for robust dual-comb spectroscopy, and, in paper [E], apart from the integration of the system, the applicability of DRS and various calibration algorithms to a biological problem were studied.

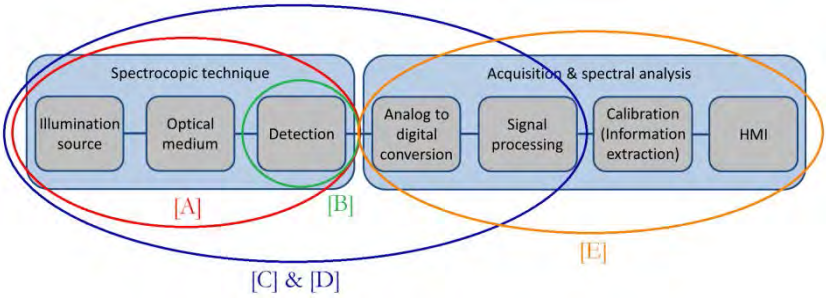

Fig. 5-1. Detailed block diagram of a spectroscopic instrument. The circles with different colors show the placement of the contribution of each paper of this dissertation.

In general, it can be considered that one of key contribution of the dissertation is the use of devices and processing techniques mainly from communications, RF, and commercial electronics to simplify the design of current spectroscopic systems. This is reflected not just in the molecular dispersion spectroscopic and DRS techniques but also and more importantly in the proposed dual-comb architectures and processing methods.

Regarding the contributions for narrow-band spectroscopy based on tunable lasers for molecular dispersion spectroscopy, the recently presented heterodyne phase-sensitive detection (HPSDS) technique has been analyzed in the second chapter of the document. The aim of the architecture is to address the problem of the influence of power fluctuations in the estimation of concentration of traditional spectroscopic molecular analysis methods. The spectroscopic method takes advantage of the phase shift introduced by the profile of the index of refraction of the spectral feature on a triple tone optical signal to estimate the concentration of gas. The output of the system is independent from the optical intensity reaching the receiver and, therefore, the classical normalization problem of absorption based sensors is overcome. On top of that, the linear relationship between concentration and change in the index of refraction provides a virtually unlimited dynamic range. A simple analytical model for the dispersion of light in the vicinity of molecular features has also been developed enabling calibration-free operation from data from spectroscopic databases. In comparison with other existing molecular dispersion spectroscopy techniques, the new method has obtained in its first demonstration a resolution limit that is in the same order of magnitude that the resolution of methods at more advanced stages of development. Furthermore, the implementation and the analysis and extraction of the spectral information are not nearly as complex as that of CLaDS systems for example.

Also in the second chapter a new architecture for CLaDS sensors was presented. This architecture is based on the optical frequency downshifting scheme of HPSDS and takes advantage of optical heterodyning techniques to provide a major simplification of current CLaDS sensors. In the monitoring of gases that are not very low pressures, the CLaDS signal that must be FM demodulated lies in the GHz range, therefore, high-end electronic spectral analyzers have been employed in the demonstrations published in the literature. The architecture proposed in this thesis allows through an optical downshifting scheme to use a low cost general purpose FM demodulator for the demodulation of the CLaDS signal, supposing a

very important reduction in the complexity and the cost of current CLaDS sensors.

Apart from the narrow-band techniques, two novel architectures based on dual-comb sources generated by the modulation of a continuous wave laser have been analyzed in chapter 3. Both setups have been devised for robust operation in clear contrast with the sensitivity of traditional ultra-wide-band dual-comb setups to almost any external factor. Furthermore, the cost of implementation, the complexity and reliability and the difficulties for configuration and operation of the electro-optic combs are by far lower than those of Ti-Saphire or fiber laser based combs. The efforts put into the developments of the new dual-comb architectures are focused on the objective of taking combs out of the lab allowing the full application of the characteristics of comb based systems on field instruments.

The first dual-comb scheme presented is devised to overcome mainly the limitations in speed of gas monitoring methods based on tunable lasers. The sweep of the spectral line that is necessary for the characterization of the spectral profile of the sample that methods based on tunable laser use for the estimation of concentration implies a limit in the speed of operation. The tunability speed of the laser, together with the associated integration times on detection, restrict the operation speed of the sensor. In contrast with the commons semi-static characterization performed by traditional OFC-based instruments, in this dissertation a high-speed multi-heterodyne dispersion molecular spectroscopic architecture is proposed. The multiple teeth of a comb are continuously monitored by a multi-channel lock-in detection scheme to yield a fast measurement of concentration that it is not dependent on the sweeping time of the laser. Besides this, the architecture uses the coherence between the repetition rates of the two combs and the acquisition hardware to eliminate any reference optical path used by current absorption-based architectures greatly simplifying preceding setups. The resolution limit found in the experimental validation of the setup slightly improved the results of tunable laser dispersion-based methods while decreasing integration times by two to three orders of magnitude.

The previously mentioned second dual-comb architecture also analyzed in chapter 3, was proposed as a general purpose instrument for spectroscopic measurements and spectral characterization of optical components with fast and robust performance. In a general purpose setup, the length of the optical cavity or the fiber of an optical device have an influence in the performance of a traditional dual-comb setup. The

placement of the sample to characterized therefore has been shifted out of the interferometric branches of the architecture increasing the stability and the robustness of operation of the system. The architecture was validated through the analysis a gas sample and an optical filter, with no reconfiguration between measurement, obtaining in both situations SNRs higher than 70 dB/Hz$^{-1/2}$ and probing the operation for integration times of 100 μs.

In chapters 2 and 3, new spectroscopic techniques and architectures have been proposed as well as signal processing (like the multi-channel lock-in detection for dual-comb setups) for spectral interrogation and the extraction of the spectral profile. In the fourth chapter, and completing each block of the diagram of a spectroscopic system (Fig. 1-1), the application of various spectral analysis methods based on data classification algorithms for biomedical studies are analyzed. Furthermore, different considerations about spectroscopic system integration are also presented. A DRS system based on a multi-laser illumination source, synchronous multi-channel lock-in detection and BSS spectral analysis methods for the monitoring of the level of angiogenesis on bioengineered skin substitutes in the first days after engraftment is detailed in chapter 4. A viability study was performed probing that the non-invasive optical instrument together with the data classification algorithms are able to differentiate between the evolutions of grafts with different states of vascularization.

There are several present and future lines of experimentation and research that are worth mentioning at this point. First, in relation with the contributions for dispersion molecular spectroscopy based on tunable lasers and, especially, on dual-comb architectures; both approaches are in their first stages of development and further work is required to fully exploit their potential and to take advantage of all the opportunities that these methods provide. Therefore, in the field of gas sensing and analysis, tests with gas samples with precisely controlled concentrations and environmental conditions should be performed in order to find the limits of these arrangements. In the same way, the applicability of the narrow-band dispersion spectroscopic methods to different areas of research has to be studied and tested.

Not only the potential, but also the range of application of the dual-comb based setups presented in chapter 3, go far beyond the experimental demonstrations carried out to validate the performance of the proposed architectures. The use of dual-comb optical sources generated by the

modulation of a continuous-wave laser for different uses is now under study by our research group. In fact, a reasonably advance state of development has been reached in the applicability of these emitters to the fast reading of optical fiber sensors and to optical ranging and positioning. Nonetheless, several improvements can be included in the setups for further system simplification, extra robustness and ease of scaling and integration.

Finally, and with respect to the spectroscopic instruments and techniques for biomedical applications (fourth chapter of this thesis), the study performed on animal models probed the viability of the non-invasive monitoring of the evolution of angiogenesis on bioengineered skin substitutes. The integration of the instrumentation system has provided a complete diagnostic, including a GUI, that can be operated by non-experts. In this sense, the system is set-up and ready to be incorporated in eventual clinical tests to study its applicability in tissue engineering and medical applications.

6. Publications

6.1 PAPER [A]

Pedro Martín-Mateos and Pablo Acedo, "Heterodyne phase-sensitive detection for calibration-free molecular dispersion spectroscopy," Opt. Express 22(12), 15143-15153 (2014)

OSA, Optics Express

Published: 06/2014

2013 Impact Factor: 3.525

Heterodyne phase-sensitive detection for calibration-free molecular dispersion spectroscopy

Pedro Martín-Mateos* and Pablo Acedo

Departamento de Tecnología Electrónica, Universidad Carlos III de Madrid, C/ Butarque 15, 28911 Leganés, Madrid, Spain

*pmmateos@ing.uc3m.es

Abstract: In this paper, a technique for molecular dispersion spectroscopy based on heterodyne phase-sensitive detection is presented. The method offers immunity to fluctuations of the received optical power and an output linearly dependent of the gas concentration. Besides this, an analytical model for the propagation of light in gaseous samples has been developed enabling calibration-free operation. The proposed architecture has been tested and experimentally validated using methane as target gas.

©2014 Optical Society of America

OCIS codes: (280.4788) Optical sensing and sensors; (300.6260) Spectroscopy, diode lasers; (300.6310) Spectroscopy, heterodyne.

References and links

1. J. Reid, J. Shewchun, B. K. Garside, and E. A. Ballik, "High sensitivity pollution detection employing tunable diode lasers," Appl. Opt. **17**(2), 300–307 (1978).
2. J. Reid, M. El-Sherbiny, B. K. Garside, and E. A. Ballik, "Sensitivity limits of a tunable diode laser spectrometer, with application to the detection of NO(2) at the 100-ppt level," Appl. Opt. **19**(19), 3349–3353 (1980).
3. H. I. Schiff, D. R. Hastie, G. I. Mackay, T. Iguchi, and B. A. Ridley, "Tunable diode laser systems for measuring trace gases intropospheric air," Environ. Sci. Technol. **17**(8), 352–364 (1983).
4. G. B. Rieker, J. B. Jeffries, and R. K. Hanson, "Calibration-free wavelength-modulation spectroscopy for measurements of gas temperature and concentration in harsh environments," Appl. Opt. **48**(29), 5546–5560 (2009).
5. G. C. Bjorklund, "Frequency-modulation spectroscopy: a new method for measuring weak absorptions and dispersions," Opt. Lett. **5**(1), 15 (1980).
6. W. Lenth, "Optical heterodyne spectroscopy with frequency- and amplitude-modulated semiconductor lasers," Opt. Lett. **8**(11), 575 (1983).
7. J. A. Silver, "Frequency-modulation spectroscopy for trace species detection: theory and comparison among experimental methods," Appl. Opt. **31**(6), 707–717 (1992).
8. J. Ye, L.-S. Ma, and J. L. Hall, "Ultrasensitive detections in atomic and molecular physics: demonstration in molecular overtone spectroscopy," J. Opt. Soc. Am. B **15**(1), 6 (1998).
9. A. Foltynowicz, F. M. Schmidt, W. Ma, and O. Axner, "Noise-immune cavity-enhanced optical heterodyne molecular spectroscopy: Current status and future potential," Appl. Phys. B **92**(3), 313–326 (2008).
10. B. M. Siller, M. W. Porambo, A. A. Mills, and B. J. McCall, "Noise immune cavity enhanced optical heterodyne velocity modulation spectroscopy," Opt. Express **19**(24), 24822–24827 (2011).
11. D. E. Cooper and T. F. Gallagher, "Double frequency modulation spectroscopy: high modulation frequency with low-bandwidth detectors," Appl. Opt. **24**(9), 1327 (1985).
12. D. E. Cooper and J. P. Watjen, "Two-tone optical heterodyne spectroscopy with a tunable lead-salt diode laser," Opt. Lett. **11**(10), 606 (1986).
13. G. R. Janik, C. B. Carlisle, and T. F. Gallagher, "Two-tone frequency-modulation spectroscopy," J. Opt. Soc. Am. B **3**(8), 1070 (1986).
14. K. Franz, D. Weidmann, and G. Wysocki, "High Dynamic Range Laser Dispersion Spectroscopy of Saturated Absorption Lines," in Conference on Lasers and Electro-Optics 2010, 2010, p. CMJ4.
15. D. Roschdestwensky, "Anomale Dispersion im Natriumdampf," Ann. Phys. **344**(12), 307–345 (1912).
16. P. van der Weijer and R. M. Cremers, "Hook method: improvement and simplification of the experimental setup," Appl. Opt. **22**(22), 3500–3502 (1983).

17. W. T. Bayha, "A revised fringe equation for the hook method in anomalous dispersion," J. Appl. Phys. **60**(5), 1560 (1986).
18. V. Majidi, W. Hsut, and D. M. Coleman, "Number density measurements on analytical discharge systems: application of 'hook' spectroscopy," Spectrochim. Acta Part B At. Spectrosc. **43**(4–5), 561–573 (1988).
19. E. Kindel, M. Kettlitz, C. Schimke, and H. Schöpp, "Application of the hook method and emission spectroscopy for the determination of radial density and temperature profiles in high-pressure mercury discharges," J. Phys. D. Appl. Phys.**31**(11), 1352–1361 (1998).
20. V. Hasson, A. J. D. Farmer, and R. W. Nicholls, "Application of dispersion techniques to molecular band intensity measurements. I. Principles of 'fringe shift' and 'fringe slope' band analysis procedures," J. Phys. B At. Mol. Phys. **5**(6), 1241–1247 (1972).
21. R. Gross, R. Chodzko, E. Turner, and J. Coffer, "Measurements of the anomalous dispersion of HF in absorption," IEEE J. Quantum Electron. **16**(7), 795–798 (1980).
22. A.-P. Tzannis, J. C. Lee, P. Beaud, H.-M. Frey, T. Greber, B. Mischler, P. P. Radi, and K. Boulouchos, "OH Concentration Measurements by Resonant Holographic Interferometry and Comparison with Direct Numerical Simulations," Flow, Turbul. Combust. **64**(3), 183–196 (2000).
23. J. J. Moschella, R. C. Hazelton, and M. D. Keitz, "Resonant, heterodyne laser interferometer for state density measurements in atoms and ions," Rev. Sci. Instrum. **77**(9), 093108 (2006).
24. G. Wysocki and D. Weidmann, "Molecular dispersion spectroscopy for chemical sensing using chirped mid-infrared quantum cascade laser," Opt. Express **18**(25), 26123–26140 (2010).
25. P. Martin-Mateos, B. Jerez, and P. Acedo, "Heterodyne architecture for tunable laser chirped dispersion spectroscopy using optical processing," Opt. Lett. **39**(9), 2611-2613 (2014).
26. L. S. Rothman, I. E. Gordon, Y. Babikov, A. Barbe, D. C. Benner, P. F. Bernath, M. Birk, L. Bizzocchi, V. Boudon, L. R. Brown, A. Campargue, K. Chance, L. H. Coudert, V. M. Devi, B. J. Drouin, A. Fayt, J.-M. Flaud, R. R. Gamache, J. Harrison, J.-M. Hartmann, C. Hill, J. T. Hodges, D. Jacquemart, A. Jolly, J. Lamouroux, R. J. LeRoy, G. Li, D. Long, C. J. Mackie, S. T. Massie, S. Mikhailenko, H. S. P. Müller, O. V. Naumenko, A. V. Nikitin, J. Orphal, V. I. Perevalov, A. Perrin, E. R. Polovtseva, C. Richard, M. A. H. Smith, E. Starikova, K. Sung, S. A. Tashkun, J. Tennyson, G. C. Toon, V. G. Tyuterev, and G. Wagner, "The HITRAN 2012 Molecular Spectroscopic Database," Journal of Quantitative Spectroscopy and Radiative Transfer. Elsevier, 01-Nov-2013.
27. G. Plant, M. Nikodem, D. M. Sonnenfroh, and G. Wysocki, "Chirped Laser Dispersion Spectroscopy for Remote Sensing of Methane at 1.65 μm . - Analysis of System Performance," in CLEO: Applications and Technology 2013, OSA Technical Digest (online) (Optical Society of America, 2013), paper JW2A.79.

1. Introduction

When light travels through a gaseous sample, it experiences absorption and dispersion in amounts dependent of the composition and characteristics of the sample. As a result, there are different spectroscopic techniques for gas sensing and analysis that are capable of identifying the gases which are present in a medium and estimate parameters like its concentration, temperature or pressure. Several of the most important of those techniques are based on the use of tunable lasers. Between them, Tunable Laser Direct Absorption Spectroscopy (TLDAS) [1] is the most straightforward method and only requires the measurement of the power transmitted through the sample. When a spectral feature of a molecule is swept by a laser, TLDAS uses the amount of optical absorption to estimate the gas concentration. However, its major drawback is the existence of a baseline that requires normalization of the transmitted power and, additionally, this baseline is usually several orders of magnitude higher than the signal variation that is to be measured, limiting the sensitivity of the system.

Wavelength Modulation Spectroscopy (WMS) [2,3] overcomes some of the limitations of TLDAS by slowly modulating the laser wavelength and detecting the power transmitted through the gas sample (generally) at the second harmonic of the modulation frequency. This technique eliminates the baseline problem and improves the signal to noise ratio of the measurement by displacing the signal to a higher frequency region. However, an inherent problem of WMS is that the amplitude of the extracted lineshape depends on the total power received, making necessary the normalization of the measured waveform. This normalization process can be complicated by the presence of fluctuations of the emitted power or by pointing instabilities and also if the optical path is partially blocked by floating particles for

example. Nevertheless, Rieker et al. have recently presented an interesting solution [4] to the problem of normalization.

A different approach is Frequency Modulation Spectroscopy (FMS) [5–7]. In this case, the wavelength modulation deviation of the laser is greater than the linewidth of the absorption feature and the high modulation frequencies decrease the intensity noise of the laser with respect to WMS. In addition, the technique is inherently baseline free and, even more important, FMS allows to measure not only optical absorption, but also wavelength dispersion. The disadvantages of this method are that high speed modulators and receivers are needed and, since the information is encoded in the amplitude of the transmitted signal, the normalization process is still indispensable. The ability of FMS to measure the dispersion spectrum has been exploited by Noise Immune Cavity Enhance Optical Heterodyne Molecular Spectroscopy (NICE-OHMS), a technique first proposed by Ye et al. [8] that is of interest for different groups [9,10]. Two Tone Frequency Modulation Spectroscopy [11–13] is a variant of FMS in which the laser wavelength is modulated using two high frequency signals separated a few megahertz. The beat note of the two signals can therefore be acquired using a low speed photodetector to give absorption information equivalent to that of FMS. As drawbacks, the ability of FMS to recover the dispersion spectrum is partially lost and power normalization remains necessary.

Tough these classic absorption spectroscopic methods are widely spread nowadays, the so called dispersion spectroscopy techniques are an interesting alternative for gas sensing and analysis. Dispersion spectroscopy methods are based on the measurement of optical dispersion associated to refractive index variations with wavelength that are inherent to molecular transitions and present significant advantages over classical methods. For example, with certain dispersion-based techniques, it is possible to directly overcome baseline and normalization problems typical of absorption-based approaches. Besides this, the refractive index changes are linearly dependent on the species concentration giving a better dynamic range to dispersion spectroscopy sensors when compared with absorption measurement instruments [14].

The first accurate measurements of molecular dispersion in the vicinity of spectral features were carried out a century ago when Roschdestwensky proposed the hook method [15]. This is a classical interferometric method that has been revised and improved over the years [16], [17] and employed in different scenarios [18,19]. The hook method has also served as the basis for the development of other techniques that use different information extraction setups [20] or illumination sources [21]. Similarly, phase shifts associated with spectral features have also been characterized combining tunable lasers and other interferometric schemes [22,23]. In a different line, Wysocki et al. recently proposed Chirped Laser Dispersion Spectroscopy (CLaDS) [24], a method that takes advantage of a frequency-chirped laser to transform optical phase changes into frequency shifts that can be demodulated to recover the dispersion spectrum. This technique can be combined with photonic processing leading to compact and easily integrable solutions [25].

In this paper, we present an alternative technique for dispersion spectroscopy, in which the optical phase shift produced by a spectral feature is measured using phase-sensitive detection. A tunable laser is intensity modulated at high frequency to generate an optical spectrum composed of three tones that is swept across the spectral range of interest. The changes of the refractive index in the vicinity of molecular transitions produce a relative phase shift between the three optical waves that is reflected in the phase of the beat note when the optical signals impinge on a square law photodetector. The phase shift of the beat note can be measured and used to recover the dispersion spectrum of the sample and, from this, the gas species present in the sample and their characteristics. Since the phase of the beat note is immune to power fluctuations, the technique inherently allows normalization-free operation. In combination, an analytical model for the propagation of light in gaseous samples has been developed enabling calibration-free molecular dispersion spectroscopy using spectral data from HITRAN [26].

In the next section, a simple analytical model for the propagation of light that describes the fundamentals of the method is presented. Then, two possible receiver schemes are introduced and experimentally validated using a ro-vibrational transition of methane at $1.65\,\mu m$. Finally, the performance of the new dispersion spectroscopy technique is discussed and compared with other existing methods.

2. Molecular dispersion spectroscopy using phase-sensitive detection

2.1 Operating principles

It is well known that the refractive index in the vicinity of a molecular transition of center ω_c [cm^{-1}] has the form:

$$n(\omega) = n_0 + s\frac{\omega_c - \omega}{(\omega_c - \omega)^2 + \left(\frac{\gamma}{2}\right)^2} \tag{1}$$

where s is a variable dependent of the spectral line and γ [cm^{-1}] is the Full Width at Half Maximum (FWHM) of the spectral feature. The graphical representation of Eq. (1) is shown in Fig. 1(a). The dispersion profile is thus characterized by ω_c and FWHM.

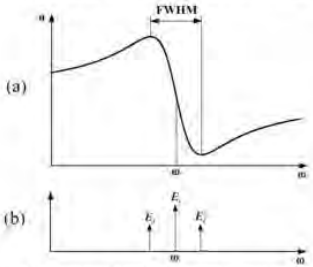

Fig. 1. (a) Refractive index in the vicinity of a molecular transition with center ω_c. (b) Spectrum of an intensity modulated optical carrier centered in the dispersion line.

When a molecular transition is swept by a multi-tone optical signal like the one shown in Fig. 1(b), each optical tone experiences a slightly different refractive index. The dispersion spectroscopy technique proposed in this paper takes advantage of this effect to recover the refractive index profile and, consequently, the characteristics of the gas in the sample. The basic scheme for a dispersion spectroscopy system based on this idea is presented in Fig. 2.

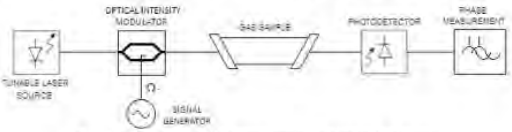

Fig. 2. Block diagram of the phase-sensitive detection technique.

A continuous wave tunable laser source is intensity modulated at a frequency Ω_1 [rad/s] to generate an optical spectrum composed of a carrier (E_1) and two sidebands (E_2 and E_3) (Fig. 1(b)):

$$E_1 = A_1 \cos(\omega_0 t) \tag{2}$$

$$E_2 = A_2 \cos\left[(\omega_0 + \Omega_1)\mathrm{t}\right] \tag{3}$$

$$E_3 = A_3 \cos\left[(\omega_0 - \Omega_1)\mathrm{t}\right] \tag{4}$$

where ω_0 [rad/s] is the optical frequency. In the vicinity of a molecular transition, electromagnetic waves of different frequencies will experience different refractive indexes. Hence, as the optical waves propagate through a dispersive medium, each component travels at a slightly different speed producing changes in their relative optical phases. At a distance L [m] from the emitter, the three optical signals can be expressed as:

$$E_1 = A_1 \cos(\omega_0 t - \varphi_1) \tag{5}$$

$$E_2 = A_2 \cos\left[(\omega_0 + \Omega_1)\mathrm{t} - \varphi_2\right] \tag{6}$$

$$E_3 = A_3 \cos\left[(\omega_0 - \Omega_1)\mathrm{t} - \varphi_3\right] \tag{7}$$

being

$$\varphi_1 = \frac{\omega_0 L}{c}\left[n(\omega_0) - 1\right] \tag{8}$$

$$\varphi_2 = \frac{\omega_0 L}{c}\left[n(\omega_0 + \Omega_1) - 1\right] \tag{9}$$

$$\varphi_3 = \frac{\omega_0 L}{c}\left[n(\omega_0 - \Omega_1) - 1\right] \tag{10}$$

where $n(\omega)$ is the refractive index of the medium at ω and c is the speed of light in vacuum. When this three component signal impinges on a square law photodetector (with adequate electrical bandwidth) two beat notes are generated as a result:

$$I_{12} \propto A_1^2/2 + A_2^2/2 + A_1 A_2 \cos\left[\Omega_1 t - (\varphi_2 - \varphi_1)\right] \tag{11}$$

$$I_{13} \propto A_1^2/2 + A_3^2/2 + A_1 A_3 \cos\left[\Omega_1 t - (\varphi_1 - \varphi_3)\right] \tag{12}$$

Then, the phase of the resulting beat note (of frequency Ω_1) can be expressed as:

$$\varphi_o = \tan^{-1}\frac{A_2 \sin(\varphi_2 - \varphi_1) + A_3 \sin(\varphi_1 - \varphi_3)}{A_2 \cos(\varphi_2 - \varphi_1) + A_3 \cos(\varphi_1 - \varphi_3)} \tag{13}$$

The expression for the phase of the beat note can be greatly simplified if absorption in the gaseous sample is considered negligible (low gas concentration). In this case, the amplitudes of the optical tones are equal, and hence, the amplitudes of two beat notes are also equal ($A_2 = A_3$) resulting in Eq. (14). As a reference, the low gas concentration approximation introduces an accuracy error of 0.85% in the experimental validation performed in this paper, nonetheless, it provides a simplified model that better illustrates the basics of the heterodyne phase-sensitive detection method.

$$\varphi_o = \frac{\varphi_2 - \varphi_3}{2} \tag{14}$$

Replacing Eqs. (9) and (10) into Eq. (14), an Eq. relating the beat note phase and the refractive indexes at the two optical frequencies is obtained:

$$\varphi_o = \frac{\omega_0 L}{2c}\left(n(\omega_0+\Omega_1)-n(\omega_0-\Omega_1)\right) \tag{15}$$

Thus, if the optical signal is swept across the spectral transitions of a gaseous sample, the dispersion profile can be retrieved from the measurement of the phase φ_o of the beat note. From φ_o, and using Eq. (15), it is possible to directly obtain the refractive index profile of the medium as a function of the wavelength, and from this, the species concentration and other different parameters of the gas.

The ability to recover the dispersion spectrum is subject, nevertheless, to the proper selection of the modulation frequency Ω_1. When the three tone signal is swept across a spectral line, the waveform and the amplitude of the detected phase signal φ_o are a function of the modulation frequency Ω_1, and the optimum modulation frequency (that maximizes the peak to peak phase output) can be obtained combining Eqs. (1) and (15). The relationship between modulation frequency Ω_1 and the peak to peak output phase φ_o is shown in Fig. 3. It must be noted that the optimum modulation frequency is equal to the FWHM of the line multiplied by 0.58.

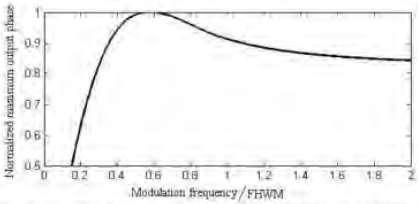

Fig. 3. Relationship between modulation frequency (normalized by the FWHM) and the maximum output phase. The modulation frequency that optimizes the measurement of dispersion is equal to the FWHM multiplied by 0.58.

At the optimum modulation frequency, when the spectral feature is swept, φ_o has the form shown in Fig. 4. If the modulation frequency is not at its optimum point, the peak to peak phase difference is reduced, and only for frequencies far from the optimum frequency the waveform is distorted.

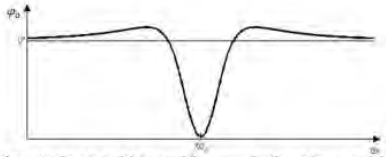

Fig. 4. Measured phase at a function of the optical frequency for the optimum modulation frequency.

To operate at optimum performance, the modulation frequency (and thus, the beat note frequency) must be in the MHz to GHz range for most gases depending on its pressure. Therefore, to obtain a compact system, heterodyning is necessary to down-shift the frequency

of the beatnote. Two different heterodyne frequency conversion architectures have been used in this paper, the first architecture is based on radio-frequency heterodyning while in the second architecture most of the signal processing is done taking advantage of optical heterodyning.

2.2 Heterodyne phase sensitive detection for calibration-free molecular dispersion spectroscopy.

As stated before, the basic scheme of the sensor presented in Fig. 2 requires an additional heterodyning stage for phase information recovery. The most obvious solution is the architecture based on radio-frequency down-conversion heterodyning shown in Fig. 5. The light of a tunable laser source is intensity modulated and detected by a high speed photodiode after traveling through the gaseous medium. The resultant beatnote must be, usually, amplified before being fed to the RF input of a mixer. A second signal generator is connected to the OL input of this mixer to obtain an intermediate frequency within the range of the lock-in amplifier that isolates the phase of the beat note. Another mixer is necessary to extract the frequency difference between the two signal generators that will be used as the reference by the lock-in amplifier.

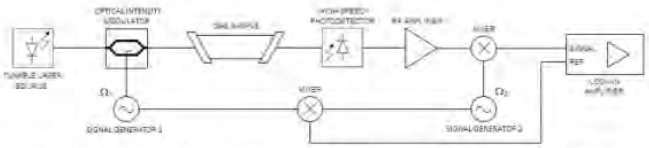

Fig. 5. Block diagram of the dispersion spectroscopy sensor based on electrical frequency conversion.

Alternatively, it is also possible to adopt an optical heterodyning approach similar to that of [25] to simplify the implementation requirements of the sensor and increase the robustness to noise and interference of the system. The block diagram of the phase-sensitive detection sensor based on optical frequency down conversion is shown in Fig. 6. The transmitter of this scheme is equal to the transmitter of the electrical frequency conversion architecture, a tunable laser source intensity modulated by an external modulator. However, in this approach, after travelling through the gas sample, the light is intensity modulated again by a second intensity modulator at a frequency Ω_2 (a few kHz lower than Ω_1). This second modulator generates two extra tones as a consequence of the modulation of the optical carrier:

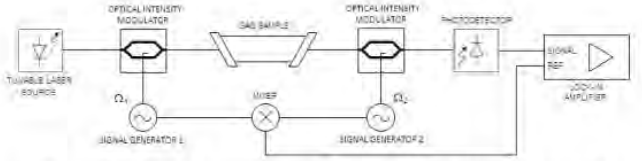

Fig. 6. Block diagram of the dispersion spectroscopy sensor based on optical frequency conversion.

$$E_4 = A_4 \cos\left[\left(\omega_0 + \Omega_2\right)t - \varphi_1\right] \tag{16}$$

$$E_5 = A_5 \cos\left[\left(\omega_0 - \Omega_2\right)t - \varphi_1\right] \tag{17}$$

and four extra tones of smaller amplitude as a consequence of the modulation of the two sidebands.

$$E_6 = A_6 \cos\left[(\omega_0 + \Omega_1 + \Omega_2)t - \varphi_2\right] \tag{18}$$

$$E_7 = A_7 \cos\left[(\omega_0 + \Omega_1 - \Omega_2)t - \varphi_2\right] \tag{19}$$

$$E_8 = A_8 \cos\left[(\omega_0 - \Omega_1 + \Omega_2)t - \varphi_3\right] \tag{20}$$

$$E_9 = A_9 \cos\left[(\omega_0 - \Omega_1 - \Omega_2)t - \varphi_3\right] \tag{21}$$

The spectrum of the nine tone signal is shown in Fig. 7. It is now possible to adjust the electrical bandwidth of the photodetector (higher than $\Omega_1 - \Omega_2$, but much lower than Ω_1 and Ω_2), to capture only the beat notes between the sidebands E_2-E_4 and E_3-E_5 obtaining a phase signal equal to that of Eq. (15) but at a frequency $\Omega_1 - \Omega_2$ (that lies directly within the operation range of the lock-in amplifier). The beat notes between E_1-E_7 and E_1-E_8 (all of them of frequency equal to $\Omega_1 - \Omega_2$) will also contribute to the beat note, even though they do not affect the output phase. Besides this, it is necessary to add a correction factor k that accounts for unbalanced sidebands amplitudes due to mismatches between the transfer function characteristics of the optical intensity modulators. This results in a new expression for the output phase of the optical frequency conversion:

$$\varphi_o = \frac{\omega_0 L}{2c}\left(k * n(\omega_0 + \Omega_1) - n(\omega_0 - \Omega_1)\right) \tag{22}$$

In our setup, k was found to be equal to 1.07. It is worthwhile to note that with this value of k, the optimum modulation frequency moves from 0.58 to 0.62 multiplied by the FWHM.

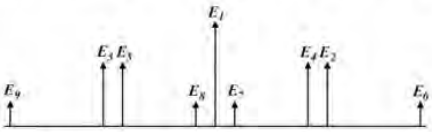

Fig. 7. Optical spectrum at the output of the second intensity modulator.

3. Experimental validation

The performance of the proposed dispersion spectroscopy architectures was experimentally demonstrated using as a target the molecular transition of methane at 1650.96 nm. To evaluate the calibration-free operation capabilities, the results are compared to simulations of the expected signals obtained using spectral data from HITRAN.

A custom build high-pressure (2150 Torr) reference gas cell of methane at a concentration of 7.5% and a path length of 70 mm was used in the tests. The tunable laser source selected was a VCSEL from VERTILAS (VERTILAS GmbH, Munich, Germany) with a tunable range of 1644.5 to 1651.5 nm. This VCSEL, the first optical intensity modulator (LN65S-FC, Thorlabs Inc., New Jersey, USA) and the gas cell were used in the tests of both architectures with equal configuration. Similarly, a SR-830 (Stanford Research Systems Inc., California, USA) lock-in amplifier was employed in both setups using a wideband balanced mixer (CMB40400609M, CERNEX Inc., California, USA) for the generation of the reference signal.

For the implementation of the electrical frequency conversion approach, a high speed XPDV2020 photodetector from u^{2}t Photonics AG (Berlin, Germany), a 2-8 GHz wideband amplifier (ZRON-8G, Mini-Circuits Inc., New York, USA) and a ZMX-10G (Mini-Circuits Inc., New York, USA) mixer were employed. Measurements were carried out with a modulation frequency approximately equal to the FWHM of the spectral line multiplied by 0.58 (Ω_1 = 7.5 GHz and Ω_2 = 7.4999 GHz, resulting in an intermediate frequency of 100 kHz). The measured and simulated dispersion spectra for this setup are shown in Fig. 8 where it is possible to appreciate the high correspondence between them. With an integration time of 1 s, a value of SNR = 19.3 dB was calculated by dividing the peak to peak phase amplitude by the standard deviation of the phase far from the absorption line. With this value of SNR, we can estimate a detection limit of 60 ppm*m/Hz$^{1/2}$. From the calibration-free operation point of view, the accuracy was calculated as the standard deviation of the difference between the measured and the simulated dispersion spectra, a figure of 4.5% was obtained.

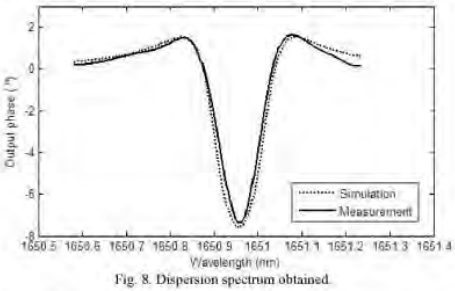

Fig. 8. Dispersion spectrum obtained.

On the other hand, in the implementation of the optical frequency conversion scheme, a second LN65S-FC optical intensity modulator was used in conjunction with a pigtailed G8195-12 InGaAs photodiode (Hamamatsu Photonics K. K., Iwai, Japan) directly connected to the lock-in amplifier current input. A modulation frequency approximately equal to 0.62 times the FWHM of the spectral feature (Ω_1 = 8 GHz and Ω_2 = 7.9999 GHz, the intermediate frequency is 100 kHz) was used in the measurements. The dispersion spectrum obtained and the results of the simulations using HITRAN data are shown in Fig. 9 (it is possible to see the unbalance in the symmetry of the waveform produced by the effect of the correction factor of Eq. (22)). The SNR was calculated as before to obtain a value of 26.5 dB for an integration time of 1 s, this gives an estimated detection limit of 11.7 ppm*m/Hz$^{1/2}$, almost an order of magnitude better than for the electrical scheme. Finally, the calibration-free accuracy was calculated obtaining a value of 3.5%.

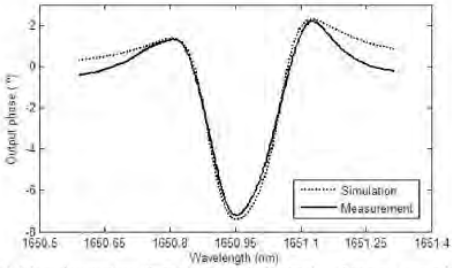

Fig. 9. Dispersion spectrum obtained using optical heterodyne frequency conversion.

As a difference with the electrical frequency conversion scheme, in the optical conversion setup the only limitations in the bandwidth of modulation frequencies are (apart from the signal generators themselves) those related to the optical intensity modulators. The modulators used in this test have an effective bandwidth ranging from DC to 18 GHz. Therefore, with the optical conversion approach, it was possible to fully characterize the dependence of the peak to peak phase with the modulation frequency and the results are shown in Fig. 10. As expected, the behavior presented is in agreement with the results of previous simulations.

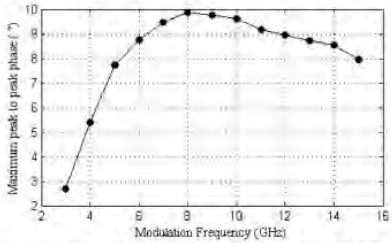

Fig. 10. Measurements of the maximum peak to peak output phase as a function of the modulation frequency.

As stated in the introduction, one of the main advantages of the described dispersion spectroscopy technique presented in this paper, when compared with absorption based methods, is the immunity of the measurement to power fluctuations. This feature was tested by increasingly obstructing the optical path of the sensor and the results are shown in Fig. 11. It is possible to see that the output phase waveform is immune to power variations of 10 dB, and only a small degradation of the SNR is noticeable.

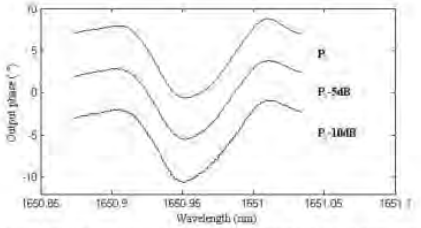

Fig. 11. Output phase signal for different power levels. The three signals are shifted vertically for viewing purposes.

4. Conclusions

In this paper, a heterodyne phase-sensitive detection technique for molecular dispersion spectroscopy has been presented, tested and experimentally validated. The method is baseline free, immune to fluctuations of the received optical power and offers an output linearly dependent of the gas concentration that leads to a high dynamic range. Moreover, two different system designs have been proposed. The high correlation between the output signal for the electrical and optical frequency down conversion schemes and the results of the analytical model makes possible calibration-free operation with an accuracy of 4.5% and 3.5% respectively. Nevertheless, these figures could be further improved mainly with a better analytical model and, in this respect, there is already work in progress.

In comparison with other dispersion spectroscopy techniques, heterodyne phase-sensitive detection sensors are far simpler to implement than interferometric approaches without penalizing the detection limit. Unlike FMS and NICE-OHMS, the presented technique offers immunity to optical power fluctuation and easier operation, nevertheless, the sensitivity is far from the figures obtained by NICE-OHMS. By the range of application, the performance of the technique presented in this paper is directly comparable to CLaDS. The optical heterodyne phase sensitive detection setup implemented in this paper obtained a detection limit of 11.7 ppm*m/Hz$^{1/2}$ for methane in the 1.65 μm region. This figure is in the same order of magnitude that the 2.7 ppm*m/Hz$^{1/2}$ obtained by classical CLaDS sensors [27] and the 6.43 ppm*m/Hz$^{1/2}$ obtained by an optical heterodyne CLaDS system [25], both detecting methane in the same spectral region. Nevertheless, in general terms, the control and information extraction procedures using phase-sensitive detection are not nearly as complex as required by CLaDS and problems like the linearity and repeatability in the wavelength swept are simplified or eliminated.

Acknowledgments

The authors would like to thank Dr. Markus Ortsiefer from VERTILAS GmbH for providing the VCSEL used in this paper.

6.2 PAPER [B]

Pedro Martín-Mateos, Borja Jerez, and Pablo Acedo, "Heterodyne architecture for tunable laser chirped dispersion spectroscopy using optical processing," Opt. Lett. 39(9), 2611-2613 (2014)

OSA, Optics Letters

Published: 04/2014

2013 Impact Factor: 3.179

Heterodyne architecture for tunable laser chirped dispersion spectroscopy using optical processing

Pedro Martín-Mateos,* Borja Jerez, and Pablo Acedo

Departamento de Tecnología Electrónica, Universidad Carlos III de Madrid, C/Butarque 15, 28911 Leganés, Madrid, Spain
**Corresponding author: pmmateos@ing.uc3m.es*

Received February 21, 2014; revised March 26, 2014; accepted March 26, 2014;
posted March 26, 2014 (Doc. ID 206964); published 0 MONTH 0000

Dispersion-based spectroscopic techniques present many desirable features when compared with classical absorption spectroscopy implementations, such as the normalization-free operation and the extended dynamic range. In this Letter, we present a new sensor design based on direct optical processing for heterodyne conversion in tunable laser chirped dispersion spectroscopy that allows sensor implementations using low-speed photodetectors and low-cost FM demodulators. The performance of the new setup has been validated using as a target the ro-vibrational transition of methane at approximately 1650.96 nm. © 2014 Optical Society of America

OCIS codes: (200.4740) Optical processing; (280.4788) Optical sensing and sensors; (300.6260) Spectroscopy, diode lasers.
http://dx.doi.org/10.1364/OL.99.099999

The use of tunable lasers has become a widely spread solution for remote gas sensing and analysis, and in the last decades several spectroscopic techniques based on the use of such sources have emerged. In classical implementations such as wavelength modulation spectroscopy (WMS) [1–6], frequency modulation spectroscopy (FMS) [7–9], and two-tone frequency modulation spectroscopy [10–12], gas concentration is retrieved from the measurement of absorption produced by the spectral features of interest (although FMS allows also to measure dispersion). In these techniques, the information is encoded in the optical power transmitted through the gas sample and therefore a normalization process must be performed to compensate for possible power fluctuations. These fluctuations can be produced by dust particles getting into the optical path or depositing on lenses or mirrors and by pointing instabilities.

A solution to the problem of normalization of classical spectroscopic sensors is the use of dispersion-based measurements such as the ones based on frequency-chirped laser sources [13]. These chirped laser dispersion spectroscopy (CLaDS) methods rely on the measurement of the optical dispersion associated to refractive index variations (with wavelength) inherent to molecular transitions. In this case, gas concentration is retrieved from the dispersion spectrum in a procedure highly immune to fluctuations of the received optical power. Hence, if the system is carefully designed, power normalization is no longer required while the baseline-free capabilities of WMS and FMS are maintained. In addition, since dispersion is linearly dependent of the concentration, dispersion spectroscopy provides an extended dynamic range of concentration measurements in comparison with the exponential concentration response of classical techniques.

Several implementations of CLaDS have been reported in the last years [13–17] in which most of the efforts have been focused on reducing the complexity and increasing the robustness of the transmitter, while the design of the receiver has largely remained unchanged. In the reported implementations, a high-speed photodetector (required to detect the high-frequency beat note used in these systems) is connected to a high-performance RF spectrum analyzer to proceed to the extraction of the dispersion information associated to the instantaneous frequency shift of the beat note.

In this Letter, we describe a new architecture for spectroscopic measurements based on dispersion spectroscopy using a frequency-chirped laser source and optical processing resulting in a compact, easily integrable and low-cost system. In contrast with other implementations, the use of an optical processing stage based on an intensity modulator for direct heterodyne conversion allows that only a low-speed photodetector and a low-cost FM demodulator are required to recover the dispersion spectrum.

The proposed scheme is shown in Fig. 1. The emitter consists of a tunable laser source and an optical intensity modulator driven at frequency Ω_1 that generates a dual-side-band spectrum. At the output of this modulator, besides the carrier (ω_0), two sidebands appear at $\omega_0 + \Omega_1$ and $\omega_0 - \Omega_1$. A small modulation index must be used to prevent the appearance of higher harmonics. The three tone signal is then coupled to a gas cell and chirped across the spectral feature of interest at a given rate (MHz/μs). After travelling through the gas sample, the three optical waves (ω_0, $\omega_0 + \Omega_1$, and $\omega_0 - \Omega_1$) have been dispersed and can be expressed as (third optical spectrum shown in Fig. 1):

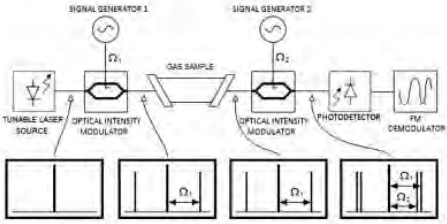

Fig. 1. Block diagram of the proposed configuration for laser dispersion spectroscopy. The optical spectra at different points of the system are also shown (see text for details).

$$E_1 = A_1 \cos\left[\omega_0(t-\Delta t_1) + \frac{1}{2}S(t-\Delta t_1)^2\right], \quad (1)$$

$$E_2 = A_2 \cos\left[(\omega_0+\Omega_1)(t-\Delta t_2) + \frac{1}{2}S(t-\Delta t_2)^2\right], \quad (2)$$

$$E_3 = A_3 \cos\left[(\omega_0-\Omega_1)(t-\Delta t_3) + \frac{1}{2}S(t-\Delta t_3)^2\right], \quad (3)$$

where

$$\Delta t_1 = \frac{L[n(\omega)-1]}{c}, \quad (4)$$

$$\Delta t_2 = \frac{L[n(\omega+\Omega_1)-1]}{c}, \quad (5)$$

$$\Delta t_3 = \frac{L[n(\omega-\Omega_1)-1]}{c}. \quad (6)$$

In these expressions, S [MHz/μs] is the chirp rate, L [m] is the length of the gas cell, ω [rad/s] is the optical frequency, $n(\omega)$ is the index of refraction of the gas at ω, and c [m/s] is the speed of light.

After the gas sample, the detection subsystem is responsible for the recovery of the dispersion spectrum. This receiver includes optical preprocessing of the optical spectrum based on a second optical intensity modulator, a low-speed photodetector, and an FM demodulator circuit (see Fig. 1). This second optical intensity modulator used after the gas sample is driven at frequency Ω_2 and, as a consequence of the modulation of the optical carrier (E_1), two extra sidebands appear in the spectrum at $\omega_0+\Omega_2$ and $\omega_0-\Omega_2$ (more tones are produced by this modulation but their amplitudes are negligible in comparison with the amplitudes of the main tones and have no noticeable effect on the demodulated signal):

$$E_4 = A_4 \cos\left[(\omega_0+\Omega_2)(t-\Delta t_1) + \frac{1}{2}S(t-\Delta t_1)^2\right], \quad (7)$$

$$E_5 = A_5 \cos\left[(\omega_0-\Omega_2)(t-\Delta t_1) + \frac{1}{2}S(t-\Delta t_1)^2\right]. \quad (8)$$

The five optical tones (last spectrum shown in Fig. 1) are then detected by a low-speed photodetector with a 3 dB bandwidth $\omega_{3\,\mathrm{dB}} \ll \Omega_1, \Omega_2$, but such as $\omega_{\mathrm{offset}} < \omega_{3\,\mathrm{dB}}$, being $\omega_{\mathrm{offset}} = \Omega_1 - \Omega_2$. Hence, and due to the optical preprocessing of the dispersion spectrum, only the beat notes between the two sets of sidebands $E_2 - E_4$ and $E_5 - E_3$ lay within the bandwidth of the photodiode and can be detected. If absorption is considered negligible, the amplitudes of the two beat notes are equal, and the phase of the resulting beat note will be an average of the phases of the two signals:

$$\varphi(t) = \left[\Omega_1 - \Omega_2 + \frac{S}{2}(\Delta t_3 - \Delta t_2)\right]t + \frac{\omega_0}{2}(\Delta t_3 - \Delta t_2) - \frac{1}{4}S(\Delta t_3^2 - \Delta t_2^2) + \Omega_2\Delta t_1 - \frac{\Omega_1}{2}(\Delta t_2 + \Delta t_3). \quad (9)$$

Equation (9) is analogous to the expression for the time dependent phase of the beat note in [13] and, therefore, under the same assumptions made in the cited reference, it is possible to obtain the instantaneous frequency of the heterodyne beat note:

$$f(\omega) = \Omega_1 - \Omega_2 + \frac{SL\omega}{2c}\left(\left.\frac{dn}{d\omega}\right|_{\omega+\Omega_1} - \left.\frac{dn}{d\omega}\right|_{\omega-\Omega_1}\right). \quad (10)$$

In Eq. (10) it is possible to see that the instantaneous frequency of the output signal provides direct information on the optical dispersion in the optical path associated to the changes of refractive index inherent to molecular transitions. This information is frequency modulated onto a carrier of a frequency, $\Omega_1 - \Omega_2$, that can be freely adjusted to be detected and demodulated using a low-speed photodetector and a simple FM demodulator circuit. The recovered demodulated signal can be then processed in an analogous way as done in previous CLaDS studies to obtain the gas concentration. It is important to note at this point that, using the scheme presented in this Letter, the requirements of the electronics are greatly reduced compared to [17] where the FM carrier frequency must be in the GHz range to enable optimum detection performance. This made mandatory the use of a high-speed photodiode and high-performance electronics for frequency demodulation.

To validate the performance of the new architecture presented, measurements of the ro-vibrational transition of methane at 1650.96 nm have been carried out. A custom-built cell of 10% methane with a path length of 70 mm and a pressure of 1250 Torr was used in the tests. The transmitter has been equipped with a 1648 nm VCSEL from VERTILAS (VERTILAS GmbH, Munich, Germany) with a tunable range from 1644.5 to 1651.5 nm. Two 10 GHz intensity modulators (LN56S-FC, Thorlabs Inc., New Jersey, USA) were also selected for the setup. The photodetector consists of an InGaAs photodiode (G8195-12, Hamamatsu Photonics K. K., Iwai, Japan) connected to a transimpedance amplifier with a bandwidth of 1 MHz. Since methane in the cell had a FWHM of approximately 8.5 GHz at 1650.96 nm, Ω_1 and Ω_2 were adjusted to 4.25 and 4.249545 GHz, respectively, to get the optimum performance of the system [13] and to fix ω_{offset} to 455 kHz. In this way, it is possible to use a low-cost FM demodulator based on the SA604A monolithic circuit (Philips Semiconductors, Eindhoven, Netherlands) with an intermediate frequency of 455 kHz connected directly to the photodetector to demodulate the beat note. It is worth noting again that ω_{offset} can be freely chosen to enable the use of any FM demodulator available.

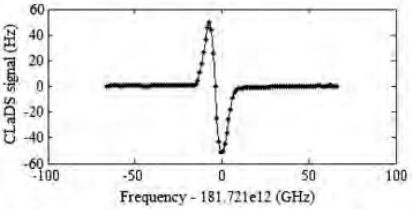

Fig. 2. Recovered chirped dispersion spectrum for $S = 150$ MHz/μs and an integration time of 1 s. Measurement has been carried out in the ro-vibrational transition of methane at approximately 1650.96 nm.

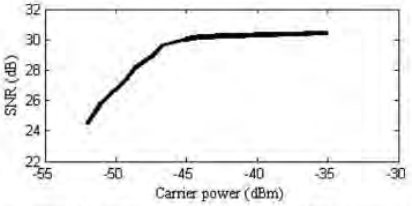

Fig. 3. Signal-to-noise ratio as a function of the power of the carrier signal measured at the photodetector. A small degradation of the SNR can be observed for values of power close to the sensitivity of the receiver.

The recovered chirped dispersion spectrum can be seen in Fig. 2 for $S = 150$ MHz/μs and an integration time of 1 s (this integration time was selected to allow direct comparison with other spectroscopic techniques). From these results, the signal-to-noise ratio (SNR) was calculated by dividing the peak-to-peak amplitude of the CLaDS signal by the standard deviation far from the absorption line. Using the estimated SNR, a detection limit of 6.43 ppm $*$ m/Hz$^{1/2}$ was obtained, a figure that is in the same order of magnitude than the detection limit for methane of previous studies [18,19].

It must be mentioned that a further advantage of using the proposed architecture with chirp rates in the order of 100 MHz/μs for gas sensing at pressures close to atmospheric pressure, is that the swept time of the spectral features is typically in the range from 60 to 150 μs, producing FM signals with bandwidths from 10 to 30 kHz approximately. Many high Q filters at 455 kHz with these bandwidths are commercially available, making it possible to optimize the noise isolation of the instrument.

Once the performance of the design has been validated, and given that the main advantage of dispersion spectroscopy over classical implementations is the normalization free capability, several measurements were carried out to test the immunity of the new architecture to power fluctuations. By increasingly obstructing the optical path of the sensor, it was found that the mean CLaDS signal remains constant for power variations up to 20 dB with a very small degradation of the SNR, as shown in Fig. 3. This limit is associated not to the proposed setup, but to the dynamic range of the low-cost FM demodulator and could be further improved by increasing the requirements of this component. In any case, the normalization free feature of dispersion spectroscopy has been demonstrated with the new sensor design.

To conclude, in this Letter a new dispersion-based gas sensor architecture has been presented. The new CLaDS setup allows the use of low-speed photodetectors and low-cost FM demodulators maintaining a similar detection limit, even for the high-modulation frequencies required under high-pressure conditions. Besides that, the operating wavelength range of the sensor has been extended beyond 1650 nm to target methane with optimum performance and with the ability of functioning at and above atmospheric pressure. Due to the wide wavelength range where the intensity modulators are able to operate, the proposed architecture could be used in combination with widely tunable laser sources [20] to provide a simple, compact and robust multispecies spectroscopy system.

The authors want to thank VERTILAS GmbH in the person of Markus Ortsiefer (Director of Research & Development) for providing the VCSEL used in these experiments.

References

1. J. Reid, J. Shewchun, B. K. Garside, and E. A. Ballik, Appl. Opt. **17**, 300 (1978).
2. J. Reid, M. El-Sherbiny, B. K. Garside, and E. A. Ballik, Appl. Opt. **19**, 3349 (1980).
3. J. Reid and D. Labrie, Appl. Phys. B **26**, 203 (1981).
4. D. R. Hastie, G. I. Mackay, T. Iguchi, B. A. Ridley, and H. I. Schiff, Environ. Sci. Technol. **17**, 352A (1983).
5. F. Slerm, G. W. Harris, D. R. Hastie, G. I. Mackay, and H. I. Schiff, J. Geophys. Res. **91D**, 5371 (1986).
6. G. B. Rieker, J. B. Jeffries, and R. K. Hanson, Appl. Opt. **48**, 5546 (2009).
7. G. C. Bjorklund, Opt. Lett. **5**, 15 (1980).
8. W. Lenth, Opt. Lett. **8**, 575 (1983).
9. J. A. Silver, Appl. Opt. **31**, 707 (1992).
10. D. E. Cooper and T. F. Gallagher, Appl. Opt. **24**, 1327 (1985).
11. D. E. Cooper and J. P. Watjen, Opt. Lett. **11**, 606 (1986).
12. G. R. Janik, C. B. Carlisle, and T. F. Gallagher, J. Opt. Soc. Am. B **3**, 1070 (1986).
13. G. Wysocki and D. Weidman, Opt. Express **18**, 26123 (2010).
14. M. Nikodem, D. Weidman, C. Smith, and G. Wysocki, Opt. Express **20**, 644 (2012).
15. M. Nikodem, D. Weidman, and G. Wysocki, Appl. Phys. B **109**, 477 (2012).
16. M. Nikodem and G. Wysocki, Sensors **12**, 16466 (2012).
17. M. Nikodem, G. Plant, Z. Wang, P. Prucnal, and G. Wysocki, Opt. Express **21**, 14649 (2013).
18. M. Nikodem, G. Plant, and G. Wysocki, in *Renewable Energy and the Environment Optics and Photonics Congress*, OSA Technical Digest (online) (Optical Society of America, 2012), paper EM2D.2.
19. G. Plant, M. Nikodem, D. M. Sonnenfroh, and G. Wysocki, in *Conference on Lasers and Electro-Optics 2013* (Optical Society of America, 2013), paper JW2A.79.
20. C. Gierl, T. Gruendl, P. Debernardi, K. Zogal, C. Grasse, H. A. Davani, G. Böhm, S. Jatta, F. Küppers, P. Meißner, and M. C. Amann, Opt. Express **19**, 17336 (2011).

6.3 PAPER [C]

Pedro Martín-Mateos, Borja Jerez and Pablo Acedo, "Dual electro-optic optical frequency combs for multiheterodyne molecular dispersion spectroscopy," Opt. Express 23(16), 21149-21158 (2015)

OSA, Optics Express

Published: 08/15

2013 Impact Factor: 3.525

Dual electro-optic optical frequency combs for multiheterodyne molecular dispersion spectroscopy

Pedro Martín-Mateos,* Borja Jerez, and Pablo Acedo

Departamento de Tecnología Electrónica, Universidad Carlos III de Madrid, C/ Butarque 15, 28911 Leganés, Madrid, Spain

*pmmateos@ing.uc3m.es

Abstract: In this paper, a multiheterodyne architecture for molecular dispersion spectroscopy based on a coherent dual-comb source generated using a single continuous wave laser and electro-optic modulators is presented and validated. The phase-sensitive scheme greatly simplifies previous dual-comb implementations by the use of an electro-optic dual comb and by phase-locking all the signal generators of the setup eliminating, in this way, the necessity of any reference optical path currently mandatory in absorption-based instruments. The architecture is immune to the classical baseline and normalization problems of absorption-based analyzers and provides an output linearly dependent on the gas concentration. In addition, the simultaneous parallel multi-wavelength measurement approach has the ability to deliver an improved output bandwidth (measurement speed) over gas analyzers based on tunable lasers.

©2015 Optical Society of America

OCIS codes: (280.4788) Optical sensing and sensors; (230.2090) Electro-optical devices; (120.6200) Spectrometers and spectroscopic instrumentation; (300.6310) Spectroscopy, heterodyne.

References and links

1. D. Roschdestwensky, "Anomale dispersion im natriumdampf," Ann. Phys. **344**(12), 307–345 (1912).
2. P. van de Weijer and R. M. M. Cremers, "Hook method: improvement and simplification of the experimental setup," Appl. Opt. **22**(22), 3500–3502 (1983).
3. E. Kindel, M. Kettlitz, C. Schimke, and H. Schöpp, "Application of the hook method and emission spectroscopy for the determination of radial density and temperature profiles in high-pressure mercury discharges," J. Phys. D Appl. Phys. **31**(11), 1352–1361 (1998).
4. R. Gross, R. Chodzko, E. Turner, and J. Coffer, "Measurements of the anomalous dispersion of HF in absorption," IEEE J. Quantum Electron. **16**(7), 795–798 (1980).
5. A. B. Duval and A. I. McIntosh, "Measurement of oscillator strength by tunable laser interferometry," J. Phys. D Appl. Phys. **13**(9), 1617–1624 (1980).
6. S. Marchetti and R. Simili, "Measurement of the refractive index dispersion around an absorbing line," Opt. Commun. **249**(1–3), 37–41 (2005).
7. A. J. Kemp, J. R. Birch, and M. N. Afsar, "The refractive index of water vapour: a comparison of measurement and theory," Infrared Phys. **18**(5–6), 827–833 (1978).
8. J. R. Birch and M. N. Afsar, "The rotation spectrum of methyl alcohol vapour between 8 and 50 cm^{-1}," Spectrochim. Acta, Part A **35**(6), 669–672 (1979).
9. J. R. Birch, "Recent progress in dispersive fourier transform spectrometry," Proc. SPIE **0289**, 362–384 (1981).
10. G. C. Bjorklund, "Frequency-modulation spectroscopy: a new method for measuring weak absorptions and dispersions," Opt. Lett. **5**(1), 15–17 (1980).
11. J. A. Silver, "Frequency-modulation spectroscopy for trace species detection: theory and comparison among experimental methods," Appl. Opt. **31**(6), 707–717 (1992).
12. M. Gehrtz, G. C. Bjorklund, and E. A. Whittaker, "Quantum-limited laser frequency-modulation spectroscopy," J. Opt. Soc. Am. B **2**(9), 1510–1526 (1985).
13. G. Wysocki and D. Weidmann, "Molecular dispersion spectroscopy for chemical sensing using chirped mid-infrared quantum cascade laser," Opt. Express **18**(25), 26123–26140 (2010).
14. M. Nikodem and G. Wysocki, "Chirped laser dispersion spectroscopy for remote open-path trace-gas sensing," Sensors (Basel) **12**(12), 16466–16481 (2012).
15. P. Martín-Mateos and P. Acedo, "Heterodyne phase-sensitive detection for calibration-free molecular dispersion spectroscopy," Opt. Express **22**(12), 15143–15153 (2014).

16. E. Baumann, F. R. Giorgetta, W. C. Swann, A. M. Zolot, I. Coddington, and N. R. Newbury, "Spectroscopy of the methane ν_3 band with an accurate midinfrared coherent dual-comb spectrometer," Phys. Rev. A **84**(6), 062513 (2011).
17. T. Rosenband, D. B. Hume, P. O. Schmidt, C. W. Chou, A. Brusch, L. Lorini, W. H. Oskay, R. E. Drullinger, T. M. Fortier, J. E. Stalnaker, S. A. Diddams, W. C. Swann, N. R. Newbury, W. M. Itano, D. J. Wineland, and J. C. Bergquist, "Frequency ratio of Al^+ and Hg^+ single-ion optical clocks; metrology at the 17th decimal place," Science **319**(5871), 1808–1812 (2008).
18. M. Niering, R. Holzwarth, J. Reichert, P. Pokasov, T. Udem, M. Weitz, T. W. Hansch, P. Lemonde, G. Santarelli, M. Abgrall, P. Laurent, C. Salomon, and A. Clairon, "Measurement of the hydrogen 1S- 2S transition frequency by phase coherent comparison with a microwave cesium fountain clock," Phys. Rev. Lett. **84**(24), 5496–5499 (2000).
19. S. Schiller, "Spectrometry with frequency combs," Opt. Lett. **27**(9), 766–768 (2002).
20. F. Keilmann, C. Gohle, and R. Holzwarth, "Time-domain mid-infrared frequency-comb spectrometer," Opt. Lett. **29**(13), 1542–1544 (2004).
21. I. Coddington, W. C. Swann, and N. R. Newbury, "Coherent dual-comb spectroscopy at high signal-to-noise ratio," Phys. Rev. A **82**(4), 043817 (2010).
22. M. J. Thorpe, K. D. Moll, R. J. Jones, B. Safdi, and J. Ye, "Broadband cavity ringdown spectroscopy for sensitive and rapid molecular detection," Science **311**(5767), 1595–1599 (2006).
23. B. Bernhardt, A. Ozawa, P. Jacquet, M. Jacquey, Y. Kobayashi, T. Udem, R. Holzwarth, G. Guelachvili, T. W. Hänsch, and N. Picqué, "Cavity-enhanced dual-comb spectroscopy," Nat. Photonics **4**(1), 55–57 (2010).
24. A. Schliesser, M. Brehm, F. Keilmann, and D. van der Weide, "Frequency-comb infrared spectrometer for rapid, remote chemical sensing," Opt. Express **13**(22), 9029–9038 (2005).
25. B. R. Washburn, W. C. Swann, and N. R. Newbury, "Response dynamics of the frequency comb output from a femtosecond fiber laser," Opt. Express **13**(26), 10622–10633 (2005).
26. T. Sakamoto, T. Kawanishi, and M. Izutsu, "Widely wavelength-tunable ultra-flat frequency comb generation using conventional dual-drive Mach-Zehnder modulator," Electron. Lett. **43**(19), 1039 (2007).
27. D. A. Long, A. J. Fleisher, K. O. Douglass, S. E. Maxwell, K. Bielska, J. T. Hodges, and D. F. Plusquellic, "Multiheterodyne spectroscopy with optical frequency combs generated from a continuous-wave laser," Opt. Lett. **39**(9), 2688–2690 (2014).
28. P. Martin-Mateos, M. Ruiz-Llata, J. Posada-Roman, and P. Acedo, "Dual comb architecture for fast spectroscopic measurements and spectral characterization," IEEE Photonics Technol. Lett. **27**(12), 1309–1312 (2015).
29. D. P. Blair and P. H. Sydenham, "Phase sensitive detection as a means to recover signals buried in noise," J. Phys. Educ. **8**(8), 621–627 (1975).
30. P. Martin-Mateos, S. Crespo-Garcia, M. Ruiz-Llata, J. R. Lopez-Fernandez, J. L. Jorcano, M. Del Rio, F. Larcher, and P. Acedo, "Remote diffuse reflectance spectroscopy sensor for tissue engineering monitoring based on blind signal separation," Biomed. Opt. Express **5**(9), 3231–3237 (2014).
31. J. Irby, R. Murray, P. Acedo, and H. Lamela, "A two-color interferometer using a frequency doubled diode pumped laser for electron density measurements," Rev. Sci. Instrum. **70**(1), 699–702 (1999).
32. N. R. Newbury, I. Coddington, and W. Swann, "Sensitivity of coherent dual-comb spectroscopy," Opt. Express **18**(8), 7929–7945 (2010).
33. G. Plant, M. Nikodem, D. M. Sonnenfroh, and G. Wysocki, "Chirped laser dispersion spectroscopy for remote sensing of methane at 1.65μm - analysis of system performance," in *CLEO:2013* OSA Technical Digest Series (Optical Society of America, 2013), paper JW2A.79.
34. P. Martin-Mateos, B. Jerez, and P. Acedo, "Heterodyne architecture for tunable laser chirped dispersion spectroscopy using optical processing," Opt. Lett. **39**(9), 2611–2613 (2014).

1. Introduction

Molecular dispersion spectroscopic methods are based on detecting the variations in the index of refraction of a gas sample that occur in the vicinity of molecular transitions. Therefore, only the phase shift introduced in an optical signal by the spectral feature is analyzed (unlike most techniques that use a measurement of absorption). Dispersion spectroscopy is a well-established approach and different methods have been demonstrated, from the Roschdestwensky hook method [1] and its variants [2–6], to Dispersive Fourier Transform Spectrometry [7–9] and Frequency Modulation Spectroscopy [10–12]. More recently, Chirped Laser Dispersion Spectroscopy (CLaDS) [13,14] and Heterodyne Phase-Sensitive Dispersion Spectroscopy (HPSDS) [15] have also been demonstrated for the measurement of dispersive features. These two later techniques present distinctive characteristics that make them very well suited to be used in gas analyzers. The main benefit of these approaches is the inherent immunity to baseline and normalization problems that results in robustness to optical power fluctuations. Therefore, these sensors are insensitive to fast power fluctuations caused by particles in suspension partially blocking the optical path of the sensor and to atmospheric turbulences or pointing instabilities (on the contrary, the normalization problem is a highly

limiting factor of absorption-based methods). Besides this, the dependency between gas concentration and the change in the index of refraction is linear (as opposed to the exponential dependency between concentration and optical absorption), enabling dispersion based methods to have a better dynamic range in comparison with absorption techniques.

Both CLaDS and HPSDS are based on monochromatic tunable laser sources that are swept over the spectral line of interest. The phase shift induced in the optical wave by the change in the index of refraction associated to the molecular transition is then detected, following different procedures, to estimate the dispersion profile and the concentration of the gas. Therefore, the dispersed optical spectrum can be characterized continuously throughout the tuning range of the laser source. Nonetheless, the sweep time of the laser and the corresponding integration times in detection imply a limit in the speed of operation of the gas analyzers based on these techniques. Such limitations might be overcome by employing a multi-tone Optical Frequency Comb (OFC) source. Even though OFCs can only perform measurement at discrete wavelengths, these points can be continuously monitored achieving in this way higher speeds of operation.

OFC sources provide an optical spectrum which consists of evenly spaced narrow linewidth modes. Passively mode-locked lasers can generate OFCs with tens of thousands of individual frequency components [16] that are spread over a spectral range of more than an octave. Furthermore, the frequency of each of the teeth of an actively stabilized or monitored comb can be referenced to a frequency standard being possible to achieve frequency accuracies far beyond the reach of any other optical spectroscopic method [17]. This combination of large bandwidth and high spectral accuracy and resolution has revolutionized the field of high-precision optical metrology [18]. Although different detection schemes for OFCs have been proposed, dual-comb detection [19–23] allows one-to-one mapping each mode of the measurement OFC into the radio-frequency (RF) domain by heterodyning with a second (reference) local oscillator (LO) comb. The resulting RF comb can therefore be electronically acquired and processed to obtain the amplitude and the (optical) phase of each tooth of the original comb.

Even tough, wideband OFCs based on Ti:sapphire [24] or Er-doped fiber [25] lasers have shown unequal potential and extraordinary capabilities, the performance, complexity and cost of these setups usually exceed the requirements of most practical applications. On the contrary, the narrow bandwidth of simple OFCs generated by electro-optic modulation of a continuous wave laser [26] is more appropriate for gas analysis and monitoring. Dual comb systems based on electro-optic OFCs present several advantages over conventional schemes, like removing the need of comb synchronization and the self-compensation of amplitude and phase fluctuations of the laser. Single laser electro-optic dual combs spectrometers have already been demonstrated [27,28] for trace gas sensing.

In this paper, a new multiheterodyne architecture based on a coherent dual-comb source generated by electro-optic modulation of a single continuous wave laser source for molecular dispersion spectroscopy is presented. This phase-sensitive scheme takes advantage of the high coherence between the repetition rates of the two OFCs and the clock used for the acquisition hardware (through phase-locking all the RF oscillators involved in the scheme) to eliminate the necessity of the reference optical path currently present in all architectures based on electro-optic dual-comb sources and thus greatly simplifying previous setups [27,28]. On top of that, and as it was previously said, since comb sources allow the parallel characterization of multiple spectral points simultaneously, the operation speed achievable by a multiheterodyne analyzer could improve by several orders of magnitude the output data rate of current tunable laser based gas detectors.

2. Molecular dispersion spectroscopy with a dual comb source using multiheterodyne detection

The basic phase-sensitive architecture of the setup for dispersion based gas analysis is shown in Fig. 1. It is a simplified version of a basic dual comb spectroscopic setup in which the reference optical path has been removed. Instead, a reference phase measurement is obtained

through a calibration process that takes advantage of the high coherence between the repetition frequencies of the RF oscillators needed to fix the repetition frequency of the combs and the sampling frequency of the acquisition hardware, as all the RF oscillators involved in the set-up are phase-locked (see below).

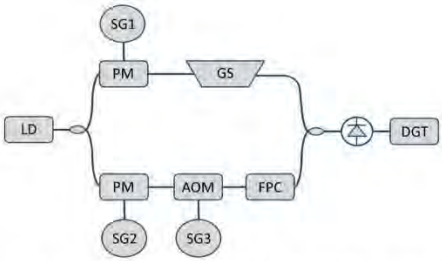

Fig. 1. Basic scheme of the dual-comb multiheterodyne dispersion gas analyzer. LD, Laser diode; PM, Electro-optic phase modulator; GS, Gas sample; AOM, Acousto-optic modulator, SG1, Signal generator at frequency f_{PM1}; SG2, Signal generator at frequency f_{PM2}; SG3, Signal generator at frequency f_{AOM}; FPC, Fiber polarization controller; DGT, Digitization..

2.1 Principles of operation

As it was previously stated, the sensor architecture has been developed for molecular dispersion spectroscopy and, consequently, only the measurement of optical dispersion (and not absorption) is used to estimate the concentration of the target gas. In fact, the detection scheme proposed in this paper has been designed to isolate the phase of each teeth of the comb independently of its amplitude. The main advantages of this approach, as presented in the introduction, are the inherent solution to the baseline and normalization problems and the extended dynamic range.

The profile of the index of refraction in the vicinity of a molecular transition of center f_c (it is worthwhile to note that the peak to peak difference of the refractive index is directly proportional to the concentration of gas) has the shape shown in Fig. 2(a). Therefore, the speed at which a monochromatic light propagates through the gas is a function of its wavelength. Thus, after propagation over a certain distance, the phase shift induced in the optical wave by the molecular sample will be given by:

$$\varphi_{f_0} = \frac{2\pi f_0 L}{c}\left[n\left(f_0\right)-1\right] \tag{1}$$

where f_0 is the frequency of the optical signal, L the distance travelled through the gas, c the speed of light in vacuum and $n\left(f_0\right)$ the index of refraction at f_0. Therefore, there is a direct dependency between the phase shift induced in the optical wave and the value of the index of refraction. The effects of absorption are as inherent as the effects of dispersion to spectral lines and, therefore, the optical wave will not only be dispersed but will also suffer from absorption. However, the proposed detection setup is immune to optical intensity variations and therefore the effect of absorption has been overlooked in this section.

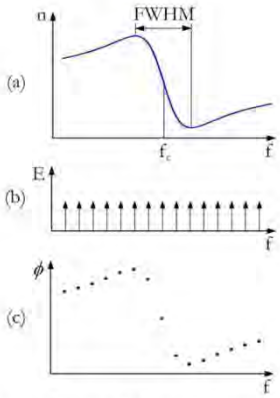

Fig. 2. (a) Profile of the index of refraction of a molecular transition line. (b) Spectrum of an ideal optical frequency comb. (c) Phase shifts induced in the teeth of the comb as a result of the propagation through a gaseous sample.

The first phase modulator of Fig. 1 (upper branch) generates an ideal OFC in which the modes are described by:

$$E_n = A\cos\left(2\pi\left(f_c + n f_{PM1}\right)t\right) \tag{2}$$

where A is the amplitude of the nth mode (that is assumed to be equal for all the teeth), f_c the central optical frequency of the comb, n = -N, -N + 1,…N the mode number and f_{PM1} the repetition frequency. When this ideal OFC, that have a spectrum like the one shown in Fig. 2(b), travels through a gas sample, the changes in the index of refraction induce an optical phase shift in the modes of the comb that is a function of their frequency and have the spectral profile shown in Fig. 2(c). Therefore, a phase term must be added to the previous expression:

$$E_n = A\cos\left(2\pi\left(f_c + n f_{PM1}\right)t - \varphi_n\right) \tag{3}$$

being φ_n (the phase of the nth mode) equal to:

$$\varphi_n = \frac{2\pi\left(f_c + n f_{PM1}\right)L}{c}\left[n\left(f_c + n f_{PM1}\right) - 1\right] \tag{4}$$

On the other hand, the LO comb (lower branch of Fig. 1) can be described as:

$$E_{n_{LO}} = A\cos\left(2\pi\left(f_c - f_{AOM} + n f_{PM2}\right)t\right) \tag{5}$$

where f_{AOM} is the frequency of the signal driving the acousto-optic modulator (AOM) and f_{PM2} the repetition frequency of the LO. The AOM is introduced in the spectrometer to shift the optical frequency of the LO comb in order to ensure the unambiguous one to one mapping between the optical and RF combs after heterodyning [27]. For illustration, the spectra of the measurement and LO combs are shown in Fig. 3.

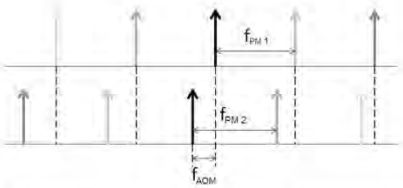

Fig. 3. Ideal optical spectrum of the measurement and LO combs generated by the setup of Fig. 1.

When the measurement comb is heterodyned with the LO on a square law detector, the phase shifts will be unequivocally mapped into the RF domain:

$$I_n \propto \cos\left(2\pi\left(f_{AOM} + n\left(f_{PM1} - f_{PM2}\right)\right)t - \varphi_n\right) \tag{6}$$

being I_n the corresponding photocurrent for each mode. The measurement comb has been, therefore, shifted in frequency from the optical domain to the RF domain (only the lower frequency beat notes are given in Eq. (6)). This RF comb can be acquired and processed to extract the value of phase at each frequency recovering from them the dispersion profile of the sample. A multi-channel lock-in parallel scheme has been proposed for the detection of the phase of the different teeth of the RF comb [29,30]. Apart from its improved isolation to noise and interference in comparison with other detection methods, the parallel multiple channel lock-in arrangement can operate at high speed generating fast output data rates. As it was previously said, the proposed detection setup is immune to optical intensity variations and therefore the effects of the different amplitudes of the teeth and absorption can be neglected.

2.2 Extracting Optical Phase Information: Requirements for phase coherence signal generators

From Eq. (6), the frequency of each one of the teeth of the RF comb generated by the dual comb setup is given by:

$$f_n = f_{AOM} + n\left(f_{PM1} - f_{PM2}\right) \tag{7}$$

where, as it was previously said, f_{AOM} is the frequency of the signal driving the AOM, f_{PM1} the repetition frequency of the first comb (equal to the modulation frequency of the first phase modulator (PM)) and f_{PM2} the repetition frequency of the local oscillator comb (equal to the modulation frequency of the second PM).

The proposed architecture is designed to obtain the optical phase shifts induced in the optical modes to infer the amount of a certain analyte. To achieve this objective, the electronic phases associated to the different teeth of the RF comb of Eq. (6) must replicate the optical phase of the different optical modes, and what it is most important, must be phase-coherent with the sampling frequency and the reference frequencies used in detection. These requirements are achieved in the proposed architecture by locking in phase all the oscillators involved in the set-up. A similar approach has been used for example for phase recovery in two-color heterodyne interferometry [31].

2.3 High speed spectroscopic measurements: Comb configuration and integration times in detection

Previous electro-optic dual OFCs implementations have been demonstrated for semi-static measurements in which the integration times were in the order of tens of seconds [27]. In front of this, the architecture here proposed is devised to provide fast operation, but before

that several considerations must be taken into account in terms of dual OFCs configuration (repetition frequencies) and integration times adjustments.

The minimum integration time for a digital lock-in amplifier used for the phase recovery of the different signals described in Eq. (6) is equal to the repetition period of the RF comb. In fact, phase acquisition and detection is greatly simplified if the integration time is adjusted to a value equal to a multiple of the repetition period of the mentioned RF comb:

$$t_{\text{int}} = n\frac{1}{f_{PM2} - f_{PM1}} \tag{8}$$

By fullfiling this condition, when the phase of a particular tooth of the comb is to be measured, the ceros of the filters of the corresponding channel of the digital lock-in amplifier are placed exactly at the position of the rest of the modes of the comb eliminating inter-channel interference (equal integration times are used in all the channels of the lock-in amplifier).

The integration time given by Eq. (8) is inversely proportional to the difference between the repetition frequencies of the optical combs (that are equal to the frequencies of the signals driving the modulators f_{PM1} and f_{PM2}). Therefore, if high speed operation is required, the separation between the repetition frequencies of the optical combs must be increased. The upper limit for this separation is, nevertheless, related to the number of optical modes of the comb (N_m) and the modulation frequency of the AOM f_{AOM}:

$$\left(f_{PM2} - f_{PM1}\right)_{\max} = \frac{2f_{AOM}}{N_m} \tag{9}$$

This limit, nevertheless, will usually be further restricted by the maximum RF bandwidth available or the characteristics of the acquisition hardware (maximum sampling frequency). It must be noted that the separation between the repetition frequencies has no effect whatsoever on the optical resolution of the comb that is only affected by the absolute value of f_{PM1}. In the same way, the spectral coverage will also be dependent on f_{PM1} and the number of teeth.

In sum, if high output data rates are targeted, the separation between the teeth of the RF comb has to be adjusted to a point close to its maximum. In this way, the pulse repetition period and hence the required integration time is minimized.

2.4 Phase calibration procedure

The multiheterodyne dual-comb architecture of Fig. 1 is a dispersion-based characterization system that, as a difference with previous schemes, does not need a reference optical path (a second interferometer) to obtain a reference measurement for the normalization of the spectrum [27]. For this purpose, there are two key aspects that are crucial in the setup: the use of phase-locked signal generators for the generation of the combs and signal digitization (sampling clock), and that only the phase (and not the amplitude) of the teeth of the comb is measured. The first point ensures that the phase coherence between the optical teeth and the acquisition system is maintained during the operation of the spectrometer. Therefore, even though the amplitude of the modes of the comb can be affected by many factors, the phases of the optical teeth are constant with time. Only variations in the index of refraction of the medium will induce phase shifts that, in what it is the second consideration, can be measured by the detection system to recover the changing dispersion profile of the sample.

As proven by Eq. (6) the phases of the teeth of the RF comb are independent of the wavelength of emission of the laser. Therefore, and having into account the previous points, a laser wavelength step can be introduced to obtain a reference phase measurement for normalization. In this way, the reference phases can be measured in a spectral region far from any absorption feature (constant value of the refractive index) before retuning the laser again into the vicinity of the molecular transition of interest for monitoring the concentration of gas.

2. 5 Multiheterodyne electro-optic dual comb System architecture

A detailed scheme of the dual-comb architecture for molecular dispersion spectroscopy presented in this paper is shown in Fig. 4. The light of a continuous wave laser source is divided in two fibers that are connected to the two modulators that generate the measurement and LO combs. As a point of reference, a regular spectrum of an OFC generated by the setup is shown at the bottom left part of Fig. 4. The measurement comb is collimated into a gas cell and launched again into fiber for the combination with the LO comb. An AOM is positioned in the LO branch to shift the optical frequency of the LO comb ensuring, as it was previously said, the unambiguous one to one mapping of the measurement comb from the optical to the RF domain. An added advantage of the use of the AOM is that the resultant RF comb is centered at the modulation frequency of the AOM reducing the influence of Flicker noise and therefore improving the SNR of the sensor. After polarization matching, the two combs are combined on a single fiber and detected on a photodiode. As previously justified, to ensure phase coherence between the teeth of the combs all the signal generators must be phase-locked to a common reference oscillator. When the wavelength of the laser is tuned to the vicinity of an absorption line the modes of the measurement OFC are dispersed by variations in the index of refraction of the molecular sample and, thus, when the comb is heterodyned with the LO on the photodetector, the induced phase shifts in each optical tooth are mapped into RF comb. Also a typical RF comb has been included for illustration in the bottom right corner of Fig. 4. The RF comb is band-pass filtered to remove lower and higher harmonics and synchronously sampled. Finally, a multi-channel phase-sensitive lock-in detection scheme measures the phase of each of the teeth of the comb.

The spectra of the optical and RF combs that are included in Fig. 4 show that the amplitudes of the teeth of the combs (unlike the phase) are not constant. Moreover, these amplitudes and the overall distribution of optical intensity are highly influenced by many factors like the power with which the modulators are driven or the temperature of the modulators. Therefore, absorption based setups include a reference optical path to compensate from these changes. The dispersion-based spectrometer here presented takes advantage of the phase coherence between optical modes to remove this reference path simplifying the optical design of the setup and increasing its robustness.

3. Experimental validation

The dispersion dual OFC based gas analyzer has been experimentally validated by measuring the ro-vibrational transition of HCN at 1544.51 nm. A HCN gas cell (HCN-13-H(5.5)-100-FCAPC, Wavelength References Inc., Oregon, USA) with a path length of 55 mm and a pressure of 100 Torr was used in the tests. The architecture was implemented using Discrete Mode laser (EP 1550-DM-HAA, Eblana Photonics Ltd., Dublin, Ireland) and two Lithium Niobate electro-optical phase modulators (PM-5S4-10-PFA-PFA-UV, EOSPACE Inc., Washington, USA) for the generation of the two OFCs. The operation range of these modulators goes from DC to 10 GHz. The measurement OFC is then collimated into the HCN cell and propagates through the gas for 55 mm before being again launched into a fiber. On the other hand, the LO comb is shifted in frequency by the AOM (T-M040-0.5C8J-3-F2S, Gooch and Housego PLC, Ilminster, United Kingdom) and polarization matched (FPC030, Thorlabs Inc., New Jersey, USA) before the combination with the measurement comb. The optical combined signal is detected by an amplified InGaAs photodetector (PDA10CF, Thorlabs Inc., New Jersey, USA) and the resulting RF comb band pass filtered (SIF-40 + , Mini-Circuits Inc., New York, USA) and digitized by a 14-bit acquisition board (PDA14, Signatec Inc., California, USA). A Holzworth HS9004A (Holzworth Instrumentation Inc., Colorado, USA) 4 channel phase coherent synthesizer was used for the generation of the modulation signals of the acousto-optic and phase modulators and the acquisition clock. The phase of each of the teeth of the comb is measured, after acquisition, by a digital 99 channel parallel lock-in amplifier implemented in Matlab (MathWorks Inc, Massachusetts, USA) with

fully configurable reference frequencies, integration times and data output rates. More details of this parallel phase-sensitive detection scheme have been given elsewhere [28].

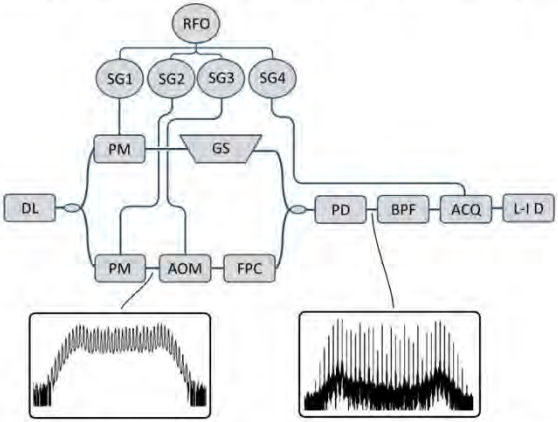

Fig. 4. Detailed block diagram of the dual-comb multiheterodyne dispersion gas analyzer. RFO, Reference frequency oscillator; SG1, Signal generator at frequency f_{PM1} ; SG2, Signal generator at frequency f_{PM2} ; SG3, Signal generator at frequency f_{AOM}; SG3, Signal generator for the acquisition clock; LD, Laser diode; PM, Electro-optic phase modulator; GS, Gas sample; AOM, Acousto-optic modulator; FPC, Fiber polarization controller; PD, Photodiode; BPF, Band-pass filter; ACQ, Acquisition hardware; L-I D, Multi-channel lock-in detector. As a reference, the typical spectrum of the optical (bottom left) and a RF (bottom right) combs generated by the setup are shown for repetition frequencies of 8 GHz and 100 kHz respectively. The spectral coverage of the OFCs is roughly 2.6 nm.

In this experimental validation, the output power of the laser was adjusted to approximately 2 mW acting over its temperature to get the emission wavelength roughly in the center of the absorption feature. The modulation frequencies of the PMs were 500 MHz and 500.1 MHz resulting in a RF repetition frequency of 100 kHz. The modulators were driven with the amplified modulation signals (with a power of around 30 dBm) to generate combs with a spectral coverage of 25 GHz (200 pm). The setup takes advantage of the distortion introduced by the power amplifiers (at power levels that are close to the maximum power output) in the signals driving the phase modulators to produce extra harmonics that allow the obtaining of a flatter comb spectrum when compared to pure sinusoidal signal excitation of the modulators. The 40 MHz signal that drives the AOM was amplified to a level of 20 dBm generating a RF comb centered at 40 MHz and with over 50 spectral components separated 100 kHz. After band pass filtering the output of the photodetector, the RF signal is synchronously subsampled at 36 MS/s generating a frequency-shifted comb centered at 4 MHz while maintaining the repetition frequency. The phases extracted by the digital multi-channel lock-in amplifier are box-smoothed to filter out multiplicative phase noise [32].

The results of one of spectral measurements are shown in Fig. 5 for an integration time of 10 ms together with the fit of the data. The available data output rate of this demonstration is therefore 100 measurements per second, however, this figure could be greatly improved by the use of sliding window integrating algorithms. The average SNR of the dispersion-based gas analyzer is 35 dB*Hz$^{-1/2}$ calculated as the ratio of the peak to peak phase and the average standard deviation in phase of the teeth of the comb. For this SNR an estimated detection limit of 17.5 ppm*m/Hz$^{1/2}$ is obtained for HCN and the extrapolation of the results to the stronger

absorption features of methane in the 1650 nm region will result in a resolution of approximately 1 ppm*m/Hz$^{1/2}$. This value is slightly better than the resolutions obtained by classical and optical heterodyne CLaDS sensors (2.7 ppm*m/Hz$^{1/2}$ [33] and 6.43 ppm*m/Hz$^{1/2}$ [34] respectively) and also improves the resolution in the detection of methane of the first HPSDS demonstration (11.7 ppm*m/Hz$^{1/2}$ [15]).

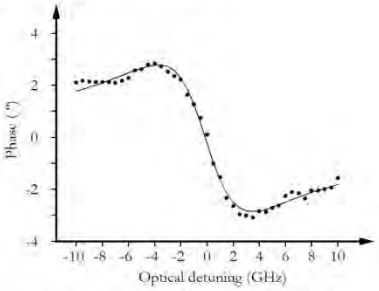

Fig. 5. Phase shift induced in the teeth of the measurement OFC by the spectral feature as a function of the optical detuning (dots). The continuous line represents the fit of the results.

5. Conclusions

In this paper a multiheterodyne architecture based on a coherent dual-comb source for molecular dispersion spectroscopy has been presented and experimentally validated. The analyzer is capable of high speed operation and uses the measurement of optical dispersion to estimate the concentration of gas. Therefore, it is immune to the classical baseline and normalization problems of absorption-based analyzers and provides a linear relationship between gas concentration and the output signal. Since the multiheterodyne approach allows the simultaneous characterization of multiple spectral points, the operation speed achievable by the presented analyzer could improve by several orders of magnitude the output data rate of current tunable laser based gas detectors.

The dual-comb source is generated by the electro-optic modulation of a single continuous wave laser. Even though the spectral coverage of these combs is smaller than the coverage of comb generated by passively mode-lock lasers, these synthesizers offer numerous advantages. The main point in favour is that the complexity in the implementation of the dual OFC system is translated from the optical to the electrical domain, where there is a great number of tools and techniques available. This results in a huge reduction of the complexity and cost of the setups and ease of configuration and operation. The power of the spectral components is also higher resulting in increased sensitivities. On top of that, the phase-sensitive scheme takes advantage of the phase coherence between the repetition rates of the two combs and the acquisition hardware to eliminate any reference optical path used by current electro-optic dual-comb architectures.

The performance of the dispersion analyzer has been experimentally validated using the spectral line of HCN at approximately 1544.51 nm. With a setup configured for providing a good spectral resolution in the measurement of the narrow spectral feature, the analyzer was able to obtain a high SNR for integration times of 10 ms. The estimated detection limit in the analysis of HCN of this first demonstration is 17.5 ppm*m/Hz$^{1/2}$. Finally, it is important to note that this scheme can also be used for the spectral characterization of optical components and fiber sensors interrogation.

6.4 PAPER [D]

Pedro Martín-Mateos, Marta Ruiz-Llata, Julio Posada-Roman and Pablo Acedo, "Dual-comb architecture for fast spectroscopic measurements and spectral characterization," IEEE Photonics Technol. Lett. 27(12), 1309-1312 (2015)

IEEE, Photonics Technology Letters

Published: 04/2015

2013 Impact Factor: 2.176

Dual-Comb Architecture for Fast Spectroscopic Measurements and Spectral Characterization

Pedro Martin-Mateos, Marta Ruiz-Llata, Julio Posada-Roman, and Pablo Acedo, *Member, IEEE*

***Abstract*— Optical frequency combs (OFCs) generated through the modulation of continuous-wave lasers offer higher power per component, simple comb spacing control, and lower complexity and cost than traditional OFCs. By these reasons, they are an interesting optical source for spectrometers. In this letter, a dual-comb architecture based on two OFCs generated from the same laser using optical phase modulators is presented. The system features a new placement for the spectroscopic sample that increases the versatility, robustness, and stability of the instrument without requiring any reconfiguration for carrying out different types of measurement. Besides this, a self-referenced detection setup based on digital phase sensitive multitone detection improves the SNR of the previous approaches offering more flexibility in its configuration and high data output rate. The proposed architecture is validated by measuring a ro-vibrational absorption feature of HCN at 1544.51 nm and characterizing the spectral response of a fiber-coupled Fabry–Perot filter.**

***Index Terms*— Optical frequency comb, heterodyne detection, optical mixing, fast spectroscopy.**

I. Introduction

DUAL-COMB spectroscopy is a technique that allows mapping each tooth of an Optical Frequency Comb (OFC) into the radio-frequency (RF) domain, where many signal processing methods are readily available. It consists on the heterodyning of two OFCs with slightly different repetition rates and it was proposed by Schiller in 2002 [1] and first demonstrated by Keilmann et al. [2] two years later. In the most extended configuration, one of the combs is sent through the sample under test and then combined with a second comb, known as the local oscillator (LO), to generate a RF comb (when the optical signals impinge on a square law photodetector). Generally, the resultant periodic interferogram is digitized and the subsequent Fourier transformation yields the amplitudes and the phases of each of the components of the measurement OFC (relative to the LO). The full accuracy and resolution of the combs has been probed with dual-comb spectroscopy [3] and many demonstrations [4]–[10] illustrate the potential of this technique. However, most of the existing OFCs are only capable of maintaining its performance in laboratory environments under well controlled conditions. Although Sinclair [11] have recently presented a fiber-laser comb that can be operated under vibration with Hz-level linewidths and femtosecond-level timing jitter for field measurements, the use of classical dual-comb spectroscopy out of the laboratory remains a challenging task.

In situations where the ultra-wide bandwidth of traditional OFCs based on solid-state or fiber lasers is not required, an interesting alternative are the combs generated through the modulation of continuous wave lasers. They offer considerable advantages like higher power of the spectral components, simple comb spacing control and far lower complexity and cost. Besides this, in its application to dual-comb spectroscopy, the possibility of generating the two combs from a single laser removes the need of synchronization and, in addition, amplitude and phase fluctuations of the laser are self-compensated [12] making possible the implementation of high stability and robust spectrometers.

In this Letter, a general purpose, compact and robust spectroscopic characterization system with a dual-comb source based on OFCs generated using a single laser and optical phase modulators is presented. The instrument is able to perform high-speed continuous spectral measurements using only commercially available components. As a main difference with conventional setups, the location of the gas sample (or the optical device under test) has been taken out from the interferometric branches and a reference optical path has been added. This, as will be justified later, endows the system with multi-purpose operation and gives a robust performance independently of the sample or device optical path length. Moreover, the use electro-optical phase modulators instead of amplitude modulators allows to increase the number of optical modes of the OFC. Even though the flatness of the comb is deteriorated, the number of modes generated is roughly doubled for the same power coupled to the RF inputs of the modulators. In addition, the system was equipped with Phase sensitive Lock-in detection providing an improved SNR and high configuration flexibility [13]. This detection technique has been extensively used in spectroscopic applications [14]–[17] and is well suited for dual-comb spectroscopy since the phase sensitive scheme rejects phase noise improving the SNR in 3 dBs [14] and also offers much more flexibility in the configuration of the combs and the data output rate. In earlier dual-comb spectroscopic systems based on OFCs generated from a single laser diode and external modulators, a conventional detection scheme in which the detected signal was digitized, averaged, and Fourier transformed was preferred [12]. Nevertheless, the fact that the number of optical modes is limited to a few hundreds

Manuscript received March 3, 2015; revised March 25, 2015; accepted April 6, 2015. Date of publication April 8, 2015; date of current version June 1, 2015.

The authors are with the Department of Electronics Technology, Universidad Carlos III de Madrid, Madrid 28911, Spain (e-mail: pmmateos@ing.uc3m.es; mruizl@ing.uc3m.es; jposada@ing.uc3m.es; pag@ing.uc3m.es).

Color versions of one or more of the figures in this letter are available online at http://ieeexplore.ieee.org.

Digital Object Identifier 10.1109/LPT.2015.2421276

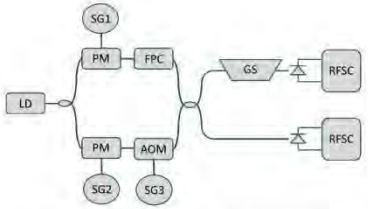

Fig. 1. Block diagram of the dual-comb spectrometer presented in this Letter. LD, Laser Diode; PM, Electro-optic phase modulator; FPC, Fiber Polarization Controller; AOM, Acousto-Optic Modulator, SG1, Signal Generator at frequency f_{PM1}; SG2, Signal Generator at frequency f_{PM2}; SG3, Signal Generator at frequency f_{AOM}; GS, Gas Sample; RFSC, Radio Frequency Signal Conditioning.

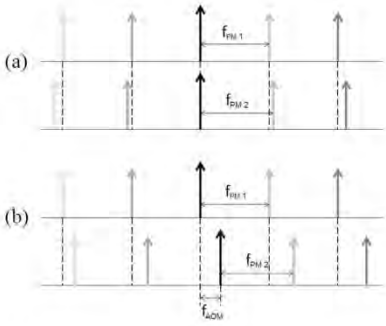

Fig. 2. Optical spectra of the OFCs. (a) Spectra of two OFCs generated using phase modulators excited with slightly different modulation frequencies f_{PM1} and f_{PM2}. If these two combs are heterodyned on a photodiode, the frequencies of the resultant beat notes are an average of the beat notes of the lower and upper sidebands. Therefore, it is not possible to unambiguously differentiate between different teeth of the combs. (b) When an AOM is included in the optical path of the second phase modulator, an optical frequency shift equal to f_{AOM} is introduced. This allows the unequivocal mapping of each tooth of the OFCs into the radio-frequency domain. The central beat note has a frequency equal to f_{AOM}, and the rest of modes are located at higher and lower frequencies.

at maximum indicates that lock-in detection technique is the proper choice given its robustness to noise and interference, and better dynamic response (speed).

II. Dual-Comb Setup for Spectroscopy and Spectral Characterization

The architecture of the proposed optical characterization setup is presented in Fig. 1. The optical power of a laser is split (50:50) in two optical paths, where two phase modulators generate OFCs with slightly different spacing. One of the combs is shifted in frequency using an acousto-optic modulator (AOM) and, after polarization matching, the two OFCs are combined. The resultant dual-comb optical signal is then divided in two optical paths, one that travels through the sample/device to be characterized and is subsequently detected (square law detector), and a second one to be used as a reference output that is directly heterodyned as well on a square law photodetector (Fig.1). The resultant RF combs (measurement and reference) are band pass filtered and digitized by the acquisition hardware. Multi-tone parallel phase sensitive detection is performed to obtain the amplitude and the phase of the spectral component of each RF comb.

When a dual comb that is obtained from one laser using modulators with slightly different spacing is heterodyned on a photodiode, the frequencies of the resultant beat notes (RF comb) are an average of the beat notes of the lower and upper sidebands (see Fig. 2(a)). These RF modes have frequencies equal to $n^*(f_{PM2} - f_{PM1})$ where $n = 1, 2,\ldots N$ is the mode number, f_{PM1} is the modulation frequency of the first comb and f_{PM2} the modulation frequency of the second comb. Therefore, to eliminate this mode averaging, an acousto-optic modulator has to be included in one of the branches of the scheme to ensure that each spectral feature of the comb is individually mapped into the RF domain (as previously proposed by Long et al. in [12]). A representation of the spectra of the two combs with the frequency shift introduced by the AOM is shown in Fig.2 (b). A further advantage of this approach is that the signal of interest is now centered at the modulation frequency of the AOM, f_{AOM}, reducing the influence of noise and hence improving the SNR of the spectrometer.

It is worthwhile to note at this point the importance of the shift in the position of the optical sample or device under test. In previous implementations, the sample was located in one of the branches of the interferometer [12]. Nevertheless, in the architecture presented in this Letter, the sample has been taken out of its traditional location and relocated after the optical combination at the output of what can be considered the dual-comb source. This results in a far more robust spectral characterization architecture given that this change in position of the sample make the instrument insensitive not only to the optical path length but also to variations in the index of refraction usually caused by temperature fluctuations. On top of that, the setup allows the characterization of fiber coupled optical components independently of the optical fiber length. In the classical configuration, when analyzing a fiber coupled component or a gas cell, the length of the fiber introduces a difference in the optical path lengths of the branches of the interferometer that, if it is not compensated, will be reflected in an increase of the noise of the system due to the deterioration of the isolation to the phase noise of the laser. This problem can be worsened in the analysis of dynamic optical devices that might even introduce stability problems in the setup.

The resultant robustness and stability of the spectral characterization architecture together with the improved noise isolation behavior of the lock-in detection method enables high speed operation, being possible to configure integration times in the order of microseconds keeping high SNRs.

III. Experimental Results

The experimental validation of the presented multi-purpose measurement architecture was done through an analysis of the ro-vibrational transition line of HCN at 1544.51 nm and the

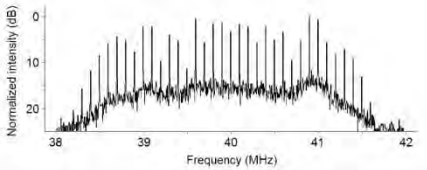

Fig. 3. Fourier transformation of the digitized reference RF comb for an acquisition time of 1 ms.

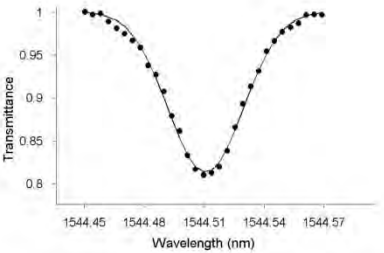

Fig. 4. Measurement of the ro-vibrational transition of HCN in the vicinity of 1544.51 nm (dots). The continuous line represents the Voigt fit of the results. An absorbance smaller than 0.2 is measured at the center of the spectral line with a linewidth slightly higher than 7 GHz.

characterization of the spectral response of a fiber coupled Fabry-Perot optical tunable filter. The setup was implemented using a Discrete Mode laser (EP 1550-DM-HAA, Eblana Photonics Ltd., Dublin, Ireland) and two Lithium Niobate electro-optical phase modulators (LN65S-FC, Thorlabs Inc., New Jersey, USA) with a frequency range from DC to 10 GHz. In the two sets of measurements carried out, the modulation signals of frequencies 500 MHz and 500.1 MHz are amplified to a level of around 30 dBm before being feed to the RF input of the phase modulators. The AOM (T-M040-0.5C8J-3-F2S, Gooch and Housego PLC, Ilminster, United Kingdom) was operated at 40 MHz with an excitation power of 20 dBm and a FPC030 (Thorlabs Inc., New Jersey, USA) manual fiber polarization controller made possible the control of the polarization state of the optical beams before being combined. Two InGaAs transimpedance amplified photodetectors (PDA10CF, Thorlabs Inc., New Jersey, USA) were employed in the detection. The resultant RF OFCs were, hence, centered at 40 MHz with a repetition rate of 100 kHz and a number of beat note modes generated of around 40 (for illustration, in Fig. 3 an example of the Fourier transformation of one of the generated reference RF combs is shown). Nevertheless, with the present setup it is possible to obtain almost 100 modes (almost twice the number of modes that can be obtained with amplitude modulators in the same operational conditions) despite of the simplicity of the OFC generators, in which only one general purpose phase modulator has been employed. It must be noted, that extra modulators or pulse shaping techniques can be employed to strongly increase the number of RF modes if necessary [18]. The RF combs were band pass filtered (SIF-40+, Mini-Circuits Inc., New York, USA) before being synchronously subsampled using a 14-Bit waveform digitizer board (PDA14, Signatec Inc., California, USA). A dual parallel 99 channels digital lock-in amplifier was implemented using Matlab (MathWorks Inc, Massachusetts, USA) in which the reference frequencies and the integration times of each channel are fully configurable as well as the data output rate (it is worth noting that it is trivial to increase the number of channels). The lock-in amplifier follows a classical design in which the digitized input is distributed between the 99 channels and multiplied separately by the in phase and quadrature signals corresponding to each of the teeth of the comb. The results of the multiplications are then averaged over the complete integration time (equivalent to a low pass filtering) to obtain the in-phase and quadrature terms and, from them, the amplitude and phase of each tooth is determined. Finally, the ratio between the amplitudes of each RF mode of the measurement and reference detectors is calculated to obtain the transmittance of the sample. This procedure protects the measurement from drifts in the amplitude of the modes of the optical combs that can be produced by many different factors.

The performance of the spectroscopic characterization setup was first validated through the measurement of one of the spectral lines of HCN in the 1543 nm region. For this, a reference HCN gas cell (HCN-13-H(5.5)-100-FCAPC, Wavelength References Inc., Oregon, USA) with a pressure of 100 Torr and an optical path length of 5.5 cm was used. The results of the measurements are shown in Fig. 4 where each of the dots represent the value of the ratio between the amplitudes of the measurement and reference RF combs. A peak absorption of 0.86 dB is found at the center wavelength together with a linewidth of around 7 GHz as expected. An integration time of 100 μs was employed in all the channels of the digital lock-in amplifier for a data output rate of 10000 measurements per second, demonstrating the high-speed spectroscopic measurement capacities of the system. In these conditions, the equivalent SNR is roughly equal to 75 dB*Hz$^{-1/2}$, calculated as the mean of the division between the standard deviation and the average value for the ratios of the beat notes of the RF frequency combs.

The system was subsequently connected to a fiber coupled FP tunable optical filter (FFP-TF2, Micron Optics Inc., Atlanta, USA) for the characterization of its spectral response. The results of such measurements are shown in Fig. 5 and from them, it is possible to obtain the optical characteristics of the filter resulting in insertion losses of 0.96 dB and a full width at half maximum of approximately 3 GHz. Also in this occasion, an integration time of 100 μs was employed in all the channels of the lock-in amplifier. In this experiment, the obtained equivalent SNR is equal to 70.5 dB*Hz$^{-1/2}$, calculated in the same conditions as before.

It should be emphasized that no reconfiguration of the system was performed whatsoever between the two measurements probing the ability of the scheme for characterizing different types of samples (and/or optical devices) without

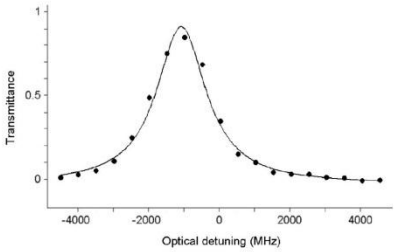

Fig. 5. Results of the characterization of the spectral response of the FFP-TF2 optical filter (dots). The continuous line represent the Lorentzian fit of the results. A transmittance of 0.8 is obtained at the central wavelength and the full width at half maximum is close to 3 GHz.

affecting the performance of the dual OFC architecture. Moreover, no temperature stabilization of the set-up, or special vibration-isolation techniques were needed in any case.

IV. Conclusion

A compact and low-cost dual-comb architecture for spectroscopy and spectral characterization of optical devices based on dual-OFCs generated from a single laser using only commercially available components has been presented and demonstrated. This system takes advantage of the higher power of the spectral components (which is reflected in higher SNRs in detection) and simple comb configuration (the repetition rate is controlled by the RF frequencies used to feed the phase modulators) of these kind of optical sources. The complexity and cost of the systems is far lower than the traditional OFCs based on Ti:sapphire or fiber lasers, as just a continuous wave laser and an electro-optical phase modulators are required to generate the combs. Using a new placement for the sample or device under test out of the interferometric branches, the versatility, robustness and stability of the instrument are increased. The spectrometer also features a multi-channel lock-in detection scheme that improves the SNR in 3 dBs and offers extreme flexibility in the configuration of the data output rate, allowing for high-speed measurements. In the experimental validation of the system, a molecular absorption line and a FP optical filter have been characterized with an output rate of 10000 measurements per second, resulting in a design capable of high speed measurements whereas keeping a high SNR value.

References

[1] S. Schiller, "Spectrometry with frequency combs," *Opt. Lett.*, vol. 27, no. 9, pp. 766–768, 2002.

[2] F. Keilmann, C. Gohle, and R. Holzwarth, "Time-domain mid-infrared frequency-comb spectrometer," *Opt. Lett.*, vol. 29, no. 13, pp. 1542–1544, 2004.

[3] E. Baumann, F. R. Giorgetta, W. C. Swann, A. M. Zolot, I. Coddington, and N. R. Newbury, "Spectroscopy of the methane ν_3 band with an accurate midinfrared coherent dual-comb spectrometer," *Phys. Rev. A*, vol. 84, no. 6, 2011, Art. ID 062513.

[4] A. M. Zolot *et al.*, "Direct-comb molecular spectroscopy with accurate, resolved comb teeth over 43 THz," *Opt. Lett.*, vol. 37, no. 4, pp. 638–640, 2012.

[5] B. Bernhardt *et al.*, "Mid-infrared dual-comb spectroscopy with 2.4 μm Cr^{2+}:ZnSe femtosecond lasers," *Appl. Phys. B*, vol. 100, no. 1, pp. 3–8, 2010.

[6] B. Bernhardt *et al.*, "Cavity-enhanced dual-comb spectroscopy," *Nature Photon.*, vol. 4, no. 1, pp. 55–57, 2009.

[7] I. Coddington, W. C. Swann, L. Nenadovic, and N. R. Newbury, "Rapid and precise absolute distance measurements at long range," *Nature Photon.*, vol. 3, no. 6, pp. 351–356, 2009.

[8] I. Coddington, W. C. Swann, and N. R. Newbury, "Coherent dual-comb spectroscopy at high signal-to-noise ratio," *Phys. Rev. A*, vol. 82, no. 4, pp. 043817-1–043817-13, 2010.

[9] A. Schliesser, M. Brehm, F. Keilmann, and D. W. van der Weide, "Frequency-comb infrared spectrometer for rapid, remote chemical sensing," *Opt. Exp.*, vol. 13, no. 22, pp. 9029–9038, 2005.

[10] T. Ideguchi, A. Poisson, G. Guelachvili, N. Picqué, and T. W. Hänsch, "Adaptive real-time dual-comb spectroscopy," *Nature Commun.*, vol. 5, p. 3375, Feb. 2014.

[11] L. C. Sinclair *et al.*, "Operation of an optically coherent frequency comb outside the metrology lab," *Opt. Exp.*, vol. 22, no. 6, pp. 6996–7006, 2014.

[12] D. A. Long *et al.*, "Multiheterodyne spectroscopy with optical frequency combs generated from a continuous-wave laser," *Opt. Lett.*, vol. 39, no. 9, pp. 2688–2690, 2014.

[13] D. P. Blair and P. H. Sydenham, "Phase sensitive detection as a means to recover signals buried in noise," *J. Phys. E, Sci. Instrum.*, vol. 8, no. 8, pp. 621–627, 1975.

[14] E. D. Diebold, B. W. Buckley, D. R. Gossett, and B. Jalali, "Digitally synthesized beat frequency multiplexing for sub-millisecond fluorescence microscopy," *Nature Photon.*, vol. 7, no. 10, pp. 806–810, 2013.

[15] M. Ruiz-Llata, P. Martín-Mateos, J. R. López, and P. Acedo, "Remote optical sensor for real-time residual salt monitoring on road surfaces," *Sens. Actuators B, Chem.*, vol. 191, pp. 371–376, Feb. 2014.

[16] P. Martín-Mateos *et al.*, "Portable, non-contact, diffuse reflectance spectroscopy system for early skin implants assessment," in *Proc. Conf. Biomed. Opt.*, 2014, pp. 1–3, paper BS3A.40.

[17] P. Martín-Mateos and P. Acedo, "Heterodyne phase-sensitive detection for calibration-free molecular dispersion spectroscopy," *Opt. Exp.*, vol. 22, no. 12, pp. 15143–15153, 2014.

[18] R. Wu, V. Torres-Company, D. E. Leaird, and A. M. Weiner, "Supercontinuum-based 10-GHz flat-topped optical frequency comb generation," *Opt. Exp.*, vol. 21, no. 5, pp. 6045–6052, 2013.

6.5 PAPER [E]

Pedro Martín-Mateos, Sergio Crespo-Garcia, Marta Ruiz-Llata, José Ramón Lopez-Fernandez, José Luis Jorcano, Marcela Del Rio, Fernando Larcher, and Pablo Acedo, "Remote diffuse reflectance spectroscopy sensor for tissue engineering monitoring based on blind signal separation," Biomed. Opt. Express 5(9), 3231-3237 (2014)

OSA, Biomedical Optics Express

Published: 08/2014

2013 Impact Factor: 3.497

Remote Diffuse Reflectance Spectroscopy sensor for tissue engineering monitoring based on Blind Signal Separation

Pedro Martín-Mateos,[1] Sergio Crespo-Garcia,[2] Marta Ruiz-Llata,[1] José Ramón Lopez-Fernandez,[1] José Luis Jorcano,[2,3] Marcela Del Rio,[2,3] Fernando Larcher[2,3] and Pablo Acedo[1,*]

[1] *Department of Electronics Technology, Universidad Carlos III de Madrid, Leganes, Madrid 28911, Spain*
[2] *Epithelial Biomedicine Division, CIEMAT, Avenida Complutense 40, Madrid 28040, Spain and Centro de Investigación Biomédica en Red de Enfermedades Raras (CIBERER), Madrid, Spain*
[3] *Department of Bioengineering, Universidad Carlos III de Madrid, Leganes, Madrid 28911, Spain*
*pag@ing.uc3m.es

Abstract: In this study the first results on evaluation and assessment of grafted bioengineered skin substitutes using an optical Diffuse Reflectance Spectroscopy (DRS) system with a remote optical probe are shown. The proposed system is able to detect early vascularization of skin substitutes expressing the Vascular Endothelial Growth Factor (VEGF) protein compared to normal grafts, even though devitalized skin is used to protect the grafts. Given the particularities of the biological problem, data analysis is performed using two Blind Signal Separation (BSS) methods: Principal Component Analysis (PCA) and Independent Component Analysis (ICA). These preliminary results are the first step towards point-of-care diagnostics for skin implants early assessment.

2014 Optical Society of America

OCIS codes: (170.6935) Tissue characterization; (170.6510) Spectroscopy, tissue diagnostics.

References and links

1. S. MacNeil, "Progress and opportunities for tissue-engineered skin," Nature **445**(7130), 874–80 (2007).
2. M. J. Escamez, M. García, F. Larcher, A. Meana, E. Munoz, J. L. Jorcano, and M. Del Río, "An In Vivo Model of Wound Healing in Genetically Modified Skin-Humanized Mice," J. Invest. Dermatol. **123**(6), 1182–1191 (2004).
3. L. Martínez-Santamaría, S. Guerrero-Aspizua, and M. Del Río, "Skin bioengineering: preclinical and clinical applications," Actas Dermosifiliogr. **103**(1), 5–11 (2012).
4. A. Vogel, V. V Chernomordik, J. D. Riley, M. Hassan, F. Amyot, B. Dasgeb, S. G. Demos, R. Pursley, R. F. Little, R. Yarchoan, Y. Tao, and A. H. Gandjbakhche, "Using noninvasive multispectral imaging to quantitatively assess tissue vasculature," J. Biomed. Opt. **12**(5), 051604 (2011).
5. A. Eguizabal, A. M. Laughney, P. B. García-Allende, V. Krishnaswamy, W. A. Wells, K. D. Paulsen, B. W. Pogue, J. M. Lopez-Higuera, and O. M. Conde, "Direct identification of breast cancer pathologies using blind separation of label-free localized reflectance measurements," Biomed. Opt. Express **4**(7), 1104–1118 (2013).
6. J. M. Kainerstorfer, M. Ehler, F. Amyot, M. Hassan, S. G. Demos, V. Chernomordik, C. K. Hitzenberger, A. H. Gandjbakhche, and J. D. Riley, "Principal component model of multispectral data for near real-time skin chromophore mapping," J. Biomed. Opt. **15**(4), 046007 (2010).
7. A. Hyvärinen and E. Oja, "Independent component analysis: algorithms and applications," Neural Networks **13**(4–5), 411–430 (2000).
8. J. Chen and X. Z. Wang, "A new approach to near-infrared spectral data analysis using independent component analysis," J. Chem. Inf. Comput. Sci. **41**(4), 992–1001 (2000).
9. A. Croitor Sava, D.M. Sima, M.C. Martinez-Bisbal, B. Celda, and S.Van Huffel, "Non-negative blind source separation techniques for tumor tissue typing using HR-MAS signals," in Proceedings of IEEE Conference on Engineering in Medicine and Biology Society (EMBC) (IEEE, 2010) pp. 3658-3661.
10. A. Hyvärinen, "Fast and robust fixed-point algorithms for Independent Component Analysis," IEEE Trans. on Neural Networks **10**(3), 626-634 (1999).

1. Introduction

Bioengineered skin substitutes appeared to solve one of the main problems in the treatment of extensive burns as it is the need for early coverage. This technology overcomes surface limitations of traditional skin grafts and it is an important help reducing the pain and potential complications during the recovery process [1]. Although robust bioengineered skin has been developed, an ideal substitute for human skin has not been achieved yet, and more tests are required to improve its performance and expand its field of application. Researchers from the Regenerative Medicine Unit of the Epithelial Biomedicine Division based at the Centro de Investigaciones Energéticas, Medioambientales y Tecnológicas (CIEMAT), Madrid, Spain have developed a humanized mouse model suitable to the study of bioengineered skin engraftment. This model has probed its validity as a preclinical platform for evaluating tissue regeneration, faithfully reproducing the functional and structural characteristics of the human wound healing process [2].

Skin regeneration tests are performed extracting skin from the back of an immunodeficient mouse and replacing it with the bioengineered skin substitute. Then, the extracted mouse skin is devitalized (by several cycles of freezing and thawing) and placed over the implant to ensure its protection during the engraftment process [3]. However, although in this manner the grafted tissue is protected, engraftment cannot readily be assessed as it is covered by the abovementioned devitalized skin.

Current implementations of optical techniques for noninvasive characterization of tissue cannot be used due to the presence of the protective devitalized skin on top of the engraftment. Besides this, such protection gets dehydrated with the pass of the days changing its optical characteristics. Only after this devitalized skin slough off, approximately three weeks after grafting, the graft recovery state can be confirmed.

In this study the first results on angiogenesis evaluation and assessment of bioengineered skin substitutes using a portable Diffuse Reflectance Spectroscopy (DRS) system [4] with a non-contact optical probe are shown. The analysis of the measured reflectances at different wavelengths is performed using two Blind Signal Separation (BSS) methods: Principal Component Analysis (PCA) and Independent Component Analysis (ICA). The proposed sensor is able to assess early enhanced vascularization of skin grafts expressing the Vascular Endothelial Growth Factor (VEGF) protein compared to normal grafts through a protective devitalized skin with an important change of its optical characteristics during time. These preliminary results are the first step towards a point-of-care diagnostics for skin implants early assessment.

2. Materials and methods

2.1 Experimental protocol

All experimental procedures involving this paper were approved by the Animal Experimental Ethical Committee (IACUC-CEEA) of CIEMAT as part of the project "Molecular, genetic and cellular bases of skin diseases: development of experimental models humanized and innovative therapeutic procedures". Four skin humanized mice were employed in the study carried out in the Epithelial Biomedicine Division in CIEMAT, Madrid, Spain. Two of the mice were grafted with a normal bioengineered skin for control, while in the other two grafts the keratinocytes of the bioengineered skins were made to overexpress VEGF protein. Vascularization is expected to appear earlier and in higher proportion in the VEGF-expressing grafted mice and the aim of this work is to study the viability of noninvasively and remotely measure this difference. The mice with VEGF-expressing grafts were labelled as VEGF1 and VEGF2 and the control mice as CTL1 and CTL2.

A control point was selected to be exclusively used to quantify the consistency of the measurements of the sensor; this point was located at the nape of the mouse. All the measurements to monitor the evolution of the bioengineered skin were carried out in the

centre of the grafts. A photograph taken to a mouse is shown in Fig. 1 a) where the locations of the control and measurement points are presented. In this picture it is possible to see the devitalized skin avoiding direct optical access to the graft; dehydration, wrinkles, and non-uniform shape are evident several days after engraftment. A detail of the remote optical head performing a measurement on a fresh engraftment (few minutes after surgery) is presented in Fig. 1 b). It is important to note the appearance of the devitalized skin on top of the graft. Comparison with Fig. 1a) shows the clear degradation of the covering and the change on its optical characteristics during the evolution of the experiment.

Measurements were performed on anesthetized mice on days 0, 2 and 6 after grafting and were followed by biopsies on day 7. To ensure the consistency of the data acquisition, three measurements were performed and averaged in each location.

a) b)

Fig. 1. a) Photograph of a mouse several days after engraftment. Note the devitalized skin on top on the engraftment, avoiding direct optical access to it. b) Detail of the optical remote probe performing a measurement on a fresh engraftment.

2.2 Sensor design

The block diagram of the sensor is shown in Fig. 2. In the architecture of the instrument it is possible to differentiate between the electronic and optical subsystems. As mentioned in the introduction, as a part of the optical system, a non-contact remote optical probe is to be used in this study. It was decided to cover all the wavelength range of the therapeutic window and the sensor was equipped with four different laser diodes with 532 nm, 635 nm, 850 nm and 1064 nm (PD-LD Inc., New Jersey, USA) wavelengths. The light of the four lasers is combined in a multimode fiber by means of optical couplers to carry the light to a fiber collimator (F220FC-780, Thorlabs Inc., New Jersey, USA) that is used for illumination of the area of interest. The measurement head is completed by a silicon photodiode (FDS100, Thorlabs Inc., New Jersey, USA) and two polarizers (LPVIS050-MP, Thorlabs Inc., New Jersey, USA) attached to the collimator and the photodetector to eliminate the effect of the Fresnell reflection in the surface of the tissue.

The four lasers are amplitude modulated at four different frequencies (3800, 4500, 5100 and 6000 Hz respectively) and the single photodiode is used to simultaneously measure all the signals. This is done taking advantage of parallel lock-in detection implemented on a multipurpose Field Programmable Gate Array (FPGA) (Cyclone III, Altera Corporation, California, USA) based system that embedded a four channel lock-in amplifier. With the exception of the laser diode drivers and the photodetector amplification stage, all the electronic subsystem is implemented into the FPGA. This multi-channel design was developed in the Electronic Technology Department of the Universidad Carlos III de Madrid (Spain). A Nios II Embedded Processor is used to control the lock-in amplifiers and to generate the modulation and control signals. By means of a RS-232 interface, the instrument

is connected to a PC where a Graphic User Interface (GUI) allows the control of the different parameters, the triggering of measurements, and data saving.

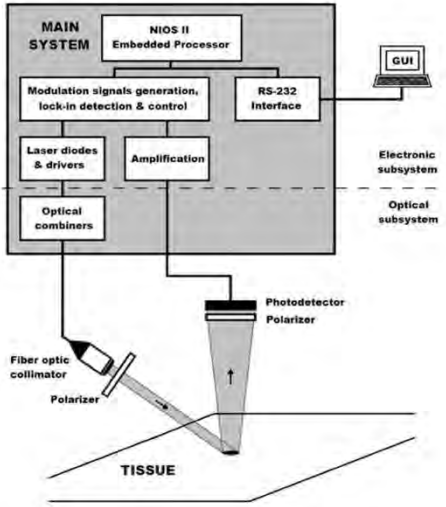

Fig. 2. Block diagram of the sensor.

2.3 Diffuse reflectance data analysis

The presence of the devitalized skin and the evolution of its optical characteristics (as shown in Fig. 1a) and b)) make standard reflectance spectrum analysis procedures like analytical models for the propagation of light in tissue or Monte-Carlo simulations difficult to apply. Likewise, it is not possible to extract valuable information from the direct analysis of the values of reflectances at the different wavelengths, given that these values are affected by many factors, like the distance from the optical head to the tissue or the movements of the mouse during the measurements. In this situation, different BSS techniques offer a better performance. In the biological problem addressed by this paper, BSS methods allow us to recover the spectral shape of several contributors (like the devitalized skin or hemoglobin) from the measurement of their mixes, relying only on the assumption of mutual independence between such contributors. There are several BSS methods each having particular characteristics, for this study PCA and ICA have been selected.

PCA has recently been evaluated to classify multispectral noncontact diffuse reflectance data both for imaging reconstruction [5] and real time evaluation of quantitative blood concentrations [6]. This technique linearly transforms data into an orthogonal coordinate system whose axes correspond to the principal components. The new coordinates of the data are the linear combination of the initial data. Each succeeding principal component is calculated in a way in which accounts for the largest possible variance, being possible to reduce the dimensionality of the data by exploiting any existing redundancy of information.

Principal components and coordinates have been calculated applying the Singular Value Decomposition algorithm.

On the other hand, ICA [7] can separate the spectra of a series of constituents from the measurements of their mixtures and, besides this, estimate the concentration of the different constituents. This method has also been previously employed to classify spectroscopic data [8] and also in biomedical applications [9]. ICA calculations have been performed using the Fixed Point Algorithm for ICA from Hyvärinen [10].

In this study, PCA and ICA calculations have been made using Matlab (MathWorks Inc, Massachusetts, USA).

3. Results and discussion

3.1 Results of the biopsies

The results of the histology of the tissues extracted from the engraftments on day 7 (after measurements were performed on days 2 and 6) are shown in Fig. 3, two sections of the a) control and b) VEGF-expressing grafts are presented. The analysis confirmed that the amount of vascularization in the VEGF-expressing grafts was bigger than that of the control grafts while the rest of the skin structure is similar.

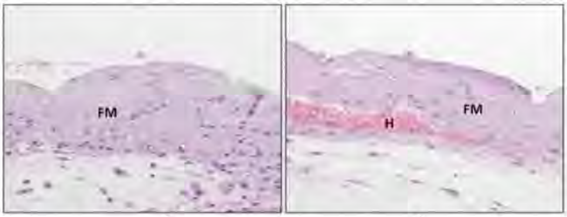

a) b)

Fig. 3. Histological appearance of engrafted bioengineered skins seven days after grafting. a) Control graft. b) VEGF-producing graft. Note the hemorrhagic blood vessels (H) invading the fibrin dermal matrix (FM).

3.2 PCA analysis

PCA has been directly applied to the reflectance values at each wavelength for the four mice on the measurements carried out on days 2 and 6. The high values of variance (92% and 98% on day 2 and 6 respectively) obtained for the first principal component lead to the conclusion that only the coordinates of each mouse for this first component are relevant in the separation between graft types. Besides this, the first principal component was found to be practically equal on both days, with a mean difference of 3.2%. This invariability in the principal components with time was also found by Kanierstorfer et al. [6] in a skin chromophore mapping study.

On day 6 there is a clear difference between coordinates for the first principal component of the mice from each group as shown in Fig. 4 a). This difference is well in agreement with the histological study previously presented where significant differences in vascularization levels were obtained. As it was said before, due to the small value of variance explained the rest of components, their coordinates are not relevant in the separation. The results of the PCA analysis showed that separation on day 2 is not possible mainly because not enough time has passed for any significant change to appear in the grafts. The evolution of the coordinates for the first principal component from day 2 to day 6 is shown in Fig. 5 a).

3.3 ICA analysis

The ICA method was, as before, applied to the reflectance values measured at each wavelength for the four mice on days 2 and 6. Three constituent components together with the estimation of their concentrations were obtained for each day. The concentrations of the three constituent components obtained for day 6 are shown in Fig. 4 b). It is possible to see how the concentrations for the first constituent component (CC1) are clearly separable for the two types of grafts, with values of 0.043 and 0.041 for the VEGF-expressing grafts and 0.123 and 0.102 for the control grafts. The concentrations of the rest of constituent components are not distinguishable for the different groups and hence, given the results of the histology, it is possible to conclude that the concentration of CC1 is related to the level of vascularization. As in the case of the PCA analysis, as shown in Fig. 5 b), there is no possible differentiation between VEGF-expressing and control grafts on day 2, but in day 6 such differentiation is obvious.

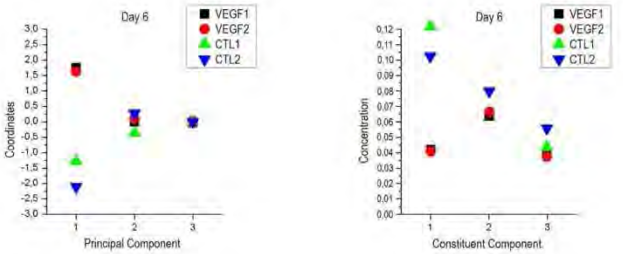

Fig. 4. a) PCA coordinates for each engraftment on day 6. Note the clear differentiation between graft types for the first principal component. b) Concentration obtained in the ICA analysis for the three constituent components. It is possible to clearly differentiate between graft types for the constituent component 1.

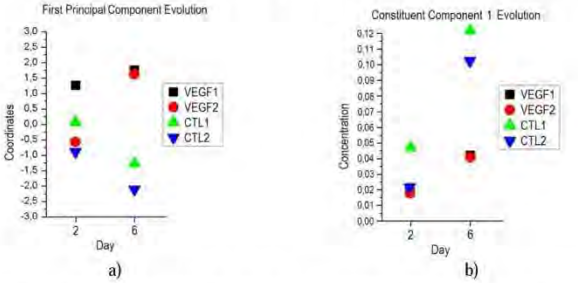

Fig. 5. a) Evolution of the coordinates of the first principal component of the PCA analysis for each mouse for days 2 and 6. b) Evolution of the concentration for the constituent component 1 obtained in the ICA analysis for days 2 and 6.

4. Conclusions

In this work the design of a DRS system that uses a remote optical probe to assess and evaluate the evolution of bioengineered skin substitutes covered by a devitalized skin has been described. Since the particularities of the biological problem addressed make difficult the application of standard spectroscopic procedures, the classification of the reflected spectra was done taking advantage of Blind Signal Separation. Spectroscopic data was analyzed using PCA and ICA being possible to differentiate, in both cases, between the early vascularization of skin substitute grafts expressing the VEGF protein and normal grafts. These preliminary results are the first step towards a point-of-care diagnostics for early skin engraftment assessment.

7. Appendix I: Comparison of the implementation of open and closed path gas analyzers

As previously presented in chapter 2, there are two distinctive approaches for the design and implementation of gas sensors: open and closed path analyzers. Whereas open path instruments perform the measurement in the mass of gas surrounding the sensor, closed path sensors need a pump to fill with a gas sample the optical cavity in which the measurements are taken. Two examples of implementations of each of the architectures (of sensors designed by the same manufacturer (LI-COR, Inc., Nebraska, USA)) are shown below.

A picture of the LI-840A CO_2 closed path analyzer without the housing cover can be found in Fig. 7-1, it is possible to see the optical cavity on top of the sensor enclosure and the two tubes that are necessary to take the air into and out of the sensor. The laser and the photodetector would be located respectively at each end of the cavity creating an optical path with its same length. To operate this setup a pump must be connected to the air intake.

Fig. 7-1. Interior of a closed path LI-840A CO_2 analyzer (LI-COR, Inc., Nebraska, USA).

In Fig. 7-2 a photograph of a LI-7500A CO_2/H_2O analyzer is shown together with the schematic of its main components. In contrast to the closed path sensor, these analyzers do not take advantage of any closed optical cavity as such and the laser light travels through open space. In the schematic of the LI-7500A it is possible to see the locations of the

illuminating source and the detector, and the optical path followed by the laser beam. Therefore, it these systems it is not necessary to take a sample of the gas and the measurement is performed directly in the volume of gas surrounding the sensor.

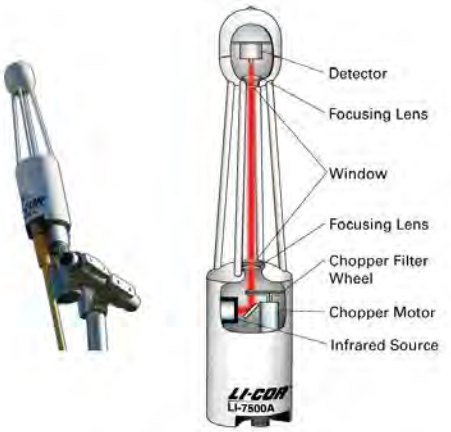

Fig. 7-2. Open path LI-7500A CO_2/H_2O analyzer (LI-COR, Inc., Nebraska, USA). At left there is a photograph of the sensor installed on a measurement station and at the right it is possible to find its basic components scheme.

8. Appendix II: Dispersion measurement in the W band for the estimation of glucose concentration in water solutions

Throughout this dissertation dispersion-based spectroscopic techniques have been used to overcome the limitations associated to the measurement of absorption. Even though the main field of application has been gas analysis and monitoring, the changes in the index of refraction can be used to estimate the characteristics of other optical media [57,58]. An example of the use of dispersion for the estimation of the concentration of metabolites in water is detailed in this appendix. In the next sections, a full feasibility study designed to test the possibility of detecting glucose in water solutions, through the measurement of dispersion using mm-wave spectroscopy in the W-band (75 – 110 GHz), is conducted.

The tests presented in this appendix are part of the work carried out in collaboration with the Ultrakurzzeitspektroskopie und Terahertz-Physik group of the Johann Wolfgang Goethe Universität. The author wants to thank professors Hartmut Roskos and Viktor Krozer for providing the opportunity of working together with their group and for the interesting discussions and, also, to Fabian Dornuf and Bernhard Hils for their great ideas and invaluable work.

The appendix begins with an introduction to the standard current blood glucose measurement sensors and to the new emerging research lines. The setup developed for the analysis is later presented and the results obtained are discussed. The last section presents the conclusions extracted from the feasibility study.

8.1 CURRENT GLUCOSE MEASUREMENT & NEW RESEARCH LINES

The monitoring of blood glucose is well established today, nevertheless, standard procedures are based on invasive methods that require to obtain full blood drops. The assessment of the level of glucose in a blood drop is performed taking advantage of an enzymatic reaction. Coarsely speaking, an enzyme is a macromolecular compound that accelerates chemical reactions. In particular, it was in 1962 when Clark and

Lyons [151] proposed the use of the glucose oxidase enzyme (GOx), that catalyses the oxidation of glucose to gluconolactone and hydrogen peroxide, for glucose monitoring. This approach employed an oxygen electrode [152] to generate an electronic current that is proportional to the concentration of glucose. From that point, enzyme-based detection systems for glucose monitoring have been importantly developed.

Three generations of enzymatic blood glucose monitoring systems have been proposed. The first generation, to which the sensor presented by Clark and Lyons belong, employs the consumption of oxygen or the release of hydrogen peroxide to determine the glucose concentration. The second generation is based on the direct transfer of electrons to electrochemically monitored redox dyes [153–155] and the third generation on direct transfer of electrons to electrodes [156–158]. There is a good number of references in which the basics of enzymatic blood glucose sensors are thoroughly reviewed and detailed [159–165].

The determination of the level of blood glucose using enzymatic methods is sufficiently accurate and inexpensive, nevertheless, these methods present many deficiencies (that are particularly important in the care of diabetes mellitus) that must be addressed. These issues have been examined in depth elsewhere [166] and potentially affect every aspect of the measurement in what could lead to wrong therapies. Briefly, the accuracy of the sensors is limited by manufacturing inconsistencies, by variations of the environmental conditions or incorrect patient handling and operation. On top of that, besides the negative effects on patient comfort, the need for a finger prick to obtain a blood drop might potentially give rise to infections. In addition, this measurements are based on consumables and have proved difficult for continuous monitoring [167]. Thus, there is a clear need for new non-invasive glucose monitoring techniques.

There are currently a few different non-invasive glucose blood assessment methods under research and development programs and some of them will be briefly reviewed below. In the same line that the spectroscopic techniques presented in previous chapters, NIR spectral measurements have been proposed for the estimation of the level of glucose [168–170]. Nevertheless, the absorption of glucose in this range is considerably small and this introduces accuracy errors that, at the moment, are in excess of specifications.

Mid-infrared (MIR) spectroscopy shares the same principles with NIR spectroscopy (but with a frequency range going from 3 to 8 μm) and has the

added advantage of stronger absorption features that simplify signal detection, even though this also limits the penetration depth. Even though in the literature the illumination source of choice is very often a Quantum Cascade laser, there are different approaches in respect to light detection. While traditional cooled mercury cadmium telluride detectors were successfully employed for the estimation of glucose concentration in biological fluids in-vitro [171], photoacoustic sensing techniques [172] have yielded better performances [173–175].

Between the photonic techniques it is also noteworthy to cite the recent works on fluorescence-based glucose sensors [176,177] and dual-wavelength optical polarimetry [178]. Also widely extended methods like optical coherence tomography [179,180] or Raman spectroscopy [181] have been employed. Apart from these techniques, different options analyzed in reasonable depth can be found in a recent review paper by So et al. [182].

Even though some of these approaches have validated the feasibility of a non-invasive monitoring of glucose, there are still accuracy and reliability issues that must be addressed. In the same way, more studies are required to establish a map of dependencies with parameters like the influence of different blood component in the assessment of the glucose content.

Apart from the research lines previously presented, there are new methods that are starting to emerge; one of them is millimeter-wave (mm-wave) spectroscopy. This method allows far deeper penetration depths than most of the other existing techniques and promises to have the advantage of being able to monitor glucose levels in blood at stand-off. Mm-wave spectroscopy has already probed its validity in the range between 500 MHz and 20 GHz for the detection of glucose in blood plasma [183] and in the range between 27 GHz and 40 GHz for the monitoring of glucose in anesthetized rats [184]. Nevertheless, there is only a small number of demonstration and mm-wave spectroscopic techniques are not well established yet.

The work presented in this appendix is intended to be a systematic study of the possibility of using mm-wave frequencies in the W-band (75 – 110 GHz) for glucose measurements. Besides this, a dispersion based technique has been proposed with the idea of overcoming common difficulties presented by absorption based methods in mind.

8.2 GLUCOSE DETECTION IN WATER SOLUTIONS IN THE W-BAND

8.2.1 Description of the setup

Measurements of dispersion in the mm-wave range for frequencies between 75 and 110 GHz have been carried out for solutions of glucose in water in different concentrations. The measurement setup is based on active frequency multipliers that are capable of shifting the frequency of an input signal from a few GHz to the W-band. The detection of the high frequency waves is performed in a similar way: the frequency of a reference signal is multiplied and then heterodyned with the detected wave. This results in an intermediate frequency signal that carries the same information (amplitude and phase) than the W-band signal.

The architecture of the instrument implementd for the study presented in this section is shown in Fig. 8-1. The output signal of a generator (SG1 in Fig. 8-1) is directly connected to the input of an AFM6-110 Active Frequency Multiplier (Radiometer Physics GmbH, Meckenheim, Germany). The AFM6-110 has a multiplication factor equal to 6 and an output frequency range that goes from 75 to 110 GHz, therefore the input signal must be in the range within 12.5 and 18.3 GHz. The output of the multiplier is coupled to a WR10 waveguide that is connected to a directional coupler, this coupler split the signal into two WR10 waveguides. Whereas one of the resultant signals is used as a reference, the other is sent through the glucose solution. A glass cuvette with an optical path length of 1 mm (Hellma Analytics GmbH, Müllheim, Germany) was located between two straight cuts in the WR10 waveguide, without having direct contact between the walls of the cuvette and the waveguides edges. The cuvette was filled with the different solutions of glucose in water. Two HMR-110-6 W-band receivers (Radiometer Physics GmbH, Meckenheim, Germany) were used to detect the signal transmitted through the solution and the reference. Apart from the main W-band input, the receivers have a second local oscillator input in which a second signal generator is connected. The frequency of the oscillator signal must be equal to the frequency of the signal feed to the Active Frequency Multiplier but with the addition of an offset that allows the shift of the W-band input signal to an intermediate frequency. The offset must be adjusted for the intermediate frequency to lie in the range between 5 and 1000 MHz. The intermediate frequency signal from both the measurement and reference detectors are digitized taking advantage of a

Handyscope HS4-10 acquisition card (TiePie engineering, Sneek, Nederland).

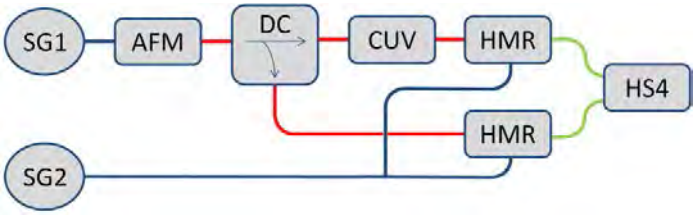

Fig. 8-1. Architecture of the dispersion measurement setup. SG, Signal Generator; AFM, Active Frequency Multiplier; DC, Directional Coupler; CUV, Cuvette; HMR, W-Band Receiver; HS4, Acquisition Hardware. The blue wires represent base band signals (12.5 – 18.5 GHz), the red wires high frequency signals (75 – 111 GHz) and the green wires the intermediate frequency signals (9 MHz).

All the samples (glucose solutions) were characterized by sweeping the frequency and local oscillator signals (SG1 and SG2 respectively in Fig. 8-1) between 12.5 GHz and 18.5 GHz in steps of 500 MHz. Therefore, the W-band signals generated for the measurement of dispersion ranged from 75 GHz to 111 GHz in steps of 3 GHz. The offset between the generators was 1.5 MHz resulting in an intermediate frequency of 9 MHz. The two intermediate frequency signals where directly oversampled at 10 MHz by an acquisition card and processed using LabView. A two channels lock-in amplifier program was implemented to yield in real time the phase difference between the signal transmitted through the sample and the reference. The presence of glucose in the solution leads to changes in the refractive index of the sample, which introduces a shift in the phase of the mm-wave signals. This shift was recorded by the setup and used to study the feasibility of glucose detection through the measurement of dispersion.

The solutions were prepared by dissolving different amounts of glucose in distilled water for concentrations of 0 mg/dL, 1000 mg/dL, 5000 mg/dL and 10000 mg/dL. Several measurements were taken for each concentration and the resultant phases at each frequency averaged to obtain the mean values and the standard deviations.

8.2.2 Analysis of results and discussion

The presence of glucose in water solutions introduces variations in the value of the permittivity of the sample and the speed at which electromagnetic waves propagate through the medium changes in accordance. This change in the speed of propagation will induce a phase difference between the signal travelling through the sample and the reference signal that has been measured for the different concentrations previously specified.

The first step in the characterization of the solutions of glucose is the measurement of the phases that appear when there is only distilled water in the cuvette. These phases will be considered as the zero value and any variations induced by the presence of glucose will be given as increments or decrements with respect to this reference.

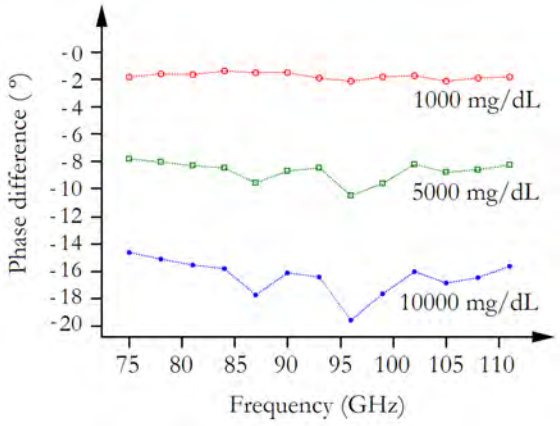

Fig. 8-2. Phase difference between the solutions of glucose in water for 1000 mg/dL, 5000 mg/dL and 10000 mg/dL with respect to distilled water.

The phase shifts induced by the different solutions of glucose as a function of the frequency are shown in Fig. 8-2. The dependency between phase difference at a function of the frequency and glucose concentration results obvious. The higher the amount of glucose in the solutions, the higher the phase different at each frequency. This reduction in the phase difference is induced by a decrease of the real part of the permitivity of the

sample related to the amount of glucose in the medium. This decrease in the value of the refractive index in the W-band produced by the increasing amount of glucose is consistent with the data previously published in the literature [182–184].

It is worthwhile to note that the maximum sensitivity of the setup (maximum phase difference in the results of Fig. 8-2) is obtained at 96 GHz and, therefore, this frequency point has been used for a correlation analysis between the induced phase difference and glucose concentration. The results of this analysis are shown in Fig. 8-3 together with the linear fit of the measurements. A value of the coefficient of determination equal to 0.9983 gives an indication of the linear relationship between phase shift and glucose concentration. This linear behavior is a typical feature of dispersion spectroscopy methods. From the linear fitting of the data the sensitivity of the setup is -1.98 °/g/dL.

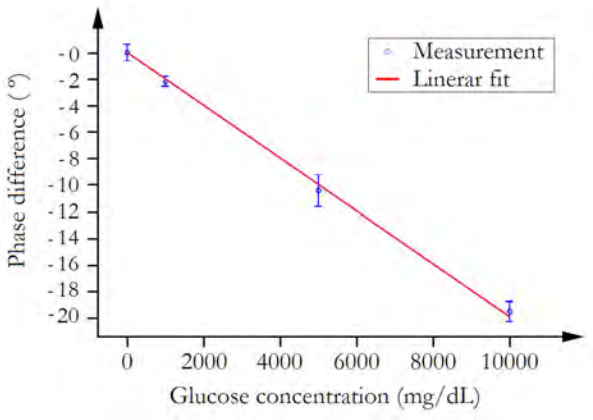

Fig. 8-3. Phase shift induced in a signal at 96 GHz as a function of the concentration of glucose in water solutions. Error bars represent the standard deviation in the measurement of the phase difference.

8.3 CONCLUSIONS

Even though the estimation of the level of blood glucose is well established today, standard procedures are based on invasive approaches in which an enzymatic method is exploited to measure the amount of glucose on a drop of blood from the patient. These techniques are sufficiently accurate and inexpensive but suffer from problems like the sensitivity of the sensors to different factors that can alter the measurement, the need for a finger prick and the difficulties for continuous monitoring.

There are currently several promising non-invasive measurement methods under development that have probed their feasibility for blood glucose detection, but nevertheless, there are still accuracy and reliability problems that must be addressed. One of the newest approaches is based on mm-wave spectroscopy that has already validated its capabilities for detecting glucose in the 500 MHz to 20 GHz and the 27 GHz to 40 GHz spectral ranges. However, the limited number of demonstration makes mm-wave spectroscopic techniques to not be well established yet.

In this appendix, the architecture of an instrument for the measurement of dispersion in the W-band (75 – 110 GHz) associated to the glucose concentration in water solutions have been presented. The results indicate that phase shifts induced by increasing concentrations of glucose are directly related to the value of concentration. Besides this, the linearity of this relation has been proved, this guarantee the high dynamic range of the setup. It is, therefore, possible to conclude that the measurement of dispersion can be used, not only for the analysis of molecular samples but also, for the characterization of targets in liquid or solid phase.

9. Appendix III: The inverse problem

The forward problem was defined in chapter 1 as the procedure to calculate the back scattered spectrum from the optical characteristics of a tissue. Between others, the RTE and, its approximate solution, the PDE provide the mathematical means to perform this calculation. Nevertheless, any spectroscopic system is designed to solve exactly the opposite problem, that is to assess the optical characteristics of a tissue (μ_s' and μ_a) from the diffusely reflected optical spectrum.

The performance of an instrument will be mainly given by the efficiency of the method used for the assessment of the optical properties of the medium from the back reflected spectral measurement. Different approaches and techniques to address the inverse problem have been proposed, from analytical to numerical or experimental models. Some of the most relevant methods will be briefly reviewed below.

The first and most obvious approach to the solution of the inverse problem is to employ a solution of the previously introduced PDE. As an example, Eq. (9-1) corresponds to the solution of the PDE (presented by Farrel et al. [130]) for a semi-infinite medium where the light emitter and the detector are separated by a distance ρ.

$$\mathrm{R}(\mu_a(\lambda), \mu_s'(\lambda), \rho) = \frac{\mu_s'}{4\pi(\mu_s' + \mu_a)}\left[z_0\left(\mu_{eff} + \frac{1}{\tilde{r}_1}\right)\frac{e^{-\mu_{eff}\tilde{r}_1}}{\tilde{r}_1{}^2} + (z_0 + 2z_b)\left(\mu_{eff} + \frac{1}{\tilde{r}_2}\right)\frac{e^{-\mu_{eff}\tilde{r}_2}}{\tilde{r}_2{}^2}\right] \quad (9\text{-}1)$$

being $\mathrm{R}(\mu_a(\lambda), \mu_s'(\lambda), \rho)$ the diffuse reflectance, $\mu_a(\lambda)$ the absorption coefficient, $\mu_s'(\lambda)$ the reduced scattering coefficient and ρ is the distance between the emitter and the detector. The rest of parameters are obtained as follows:

$$z_0 = \frac{1}{\mu_s' + \mu_a} \quad (9\text{-}2)$$

$$\mu_{eff} = [3\mu_a(\mu_a + \mu_s')]^{1/2} \tag{9-3}$$

$$\tilde{r}_1 = (z_0{}^2 + \rho^2)^{1/2} \tag{9-4}$$

$$\tilde{r}_2 = [(z_0 + 2z_b)^2 + \rho^2] \tag{9-5}$$

and finally z_b allows to define different boundary conditions. If Eqs. (9-1 – 9-5) are analyzed, it is possible to conclude that the diffuse reflectance is exclusively a function of $\mu_a(\lambda)$ and $\mu_s'(\lambda)$ (besides the distance between emitter and receiver ρ and the boundary conditions defined by z_b). Therefore, a system of coupled equations can be stated for measurements of reflectance at several wavelengths. The solution to this system of equations yields the optical characteristics of the medium (as will be presented later, further assumptions are needed).

In another paper, Gandjbakhche and Weiss [131] presented a different approach, a solution of the random-walk expression for the diffuse reflectance that is shown in Eq. (9-6). The expression corresponds to the reflectance of a semi-infinite medium with absorbing boundary and no index mismatch in which the illumination and detection of light is performed over the same spot.

$$\mathrm{R}(\mu) = \frac{e^{-2\mu}}{\sqrt{24\mu}}\left[1 - e^{-\sqrt{24\mu}}\right] \tag{9-6}$$

where $\mathrm{R}(\mu)$ is the diffuse reflectance and $\mu = (\mu_a/\mu_s')$ is the ratio between absorption and reduced scattering coefficients. Eq. (9-6) has been further simplified by Vogel et al. [118] considering reasonable values of the optical coefficients of tissues in the red and near-infrared spectral range resulting in Eq. (9-7):

$$\mathrm{R}(\mu) = 1.06 - 1.45\mu^{0.35} \tag{9-7}$$

again μ is equal to the ratio between absorption and reduced scattering coefficients, and as before, a system of coupled equations can be stated taking advantage of measurements of the reflectance at various wavelengths to obtain the optical characteristics of the medium. Nevertheless, as in the

case of Eq. (9-1), independently of the approach employed in any continuous wave DRS system there exists cross talk between the absorption and scattering coefficients [185] and therefore it is not possible to uniquely separate absorption and scattering contributions. Fortunately, the objective of a DRS sensor for biomedical applications is not the determination of the optical coefficients of the tissue, but the determination of the tissue structure and composition (calibration).

In different publications it has been proved that a continuous wave DRS system can uniquely reconstruct chromophore concentrations in tissues [186,187]. For this purpose several assumptions must be made. Firstly, the reduced absorption coefficient must be approximated for a simplified Mie scattering behaviour:

$$\mu_s'(\lambda) = a\lambda^{-b} \tag{9-8}$$

where a and b are parameters related to the size, the refractive index, and the concentration of scatters as well as the refractive index of the surrounding medium. Second, the absorption coefficient must be expressed as:

$$\mu_a(\lambda) = \sum_i \varepsilon_i(\lambda) c_i \tag{9-9}$$

where c_i is the concentration and $\varepsilon_i(\lambda)$ is the extinction coefficient of the ith chromophore at wavelength λ. It must be noted that the extinction coefficients of the chromophores present in biological tissues, like hemoglobin, melanin, lipids and water, are well-known. The concentration of these analytes in the tissues may be used to diagnose disease and to monitor changes in various conditions [118].

Another widely used approach to the inverse problem, completely different from the previously presented analytical methods however closely related to the PDE, is the Monte Carlo (MC) method [132,133]. MC computational methods are based on random simulations that are repeated in huge numbers allowing to find solutions to various problems. In this particular case, the path followed by millions of photons is traced in its travel through a tissue with predefined characteristics, this enables the obtaining of a simulated diffuse back reflected spectrum for any given scenario.

The MC method is not only a mechanism for solving the inverse problem but it is also a powerful tool for the evaluation of the performance of a diffusion model for different physical geometries [134], the study of the wavelength dependence of the penetration depth and the sampling volume of the detected light or the analysis the contribution to the spectrum of the different layers of the skin [188] and different chromophores.

Also in a completely different line a lookup table (LUT) based model for the determination of the optical characteristics of a turbid media has been proposed [189]. This method is based on experimental measurements of the diffuse reflectance spectrum of reference samples with known optical properties. It is then possible to map the reflectance to the absorption and reduced scattering coefficients creating a matrix that is interpolated to obtain a complete LUT for the determination of the optical characteristics of an arbitrary tissue [190].

A much simpler method based on the use of ratios between the backscattered intensities at different wavelengths has also been successfully proved for the detection and monitoring of diseased tissue [123].

The methods previously presented have been validated through extensive tests and many different experiments achieving remarkably good performances. Nevertheless, there are situations in which the applicability of these approaches is difficult. For example, in the case of solutions to the PDE, in some experiments the assumptions that ensure the accuracy of the approximation may not be guaranteed. On top of that, not in every situation it is possible to unequivocally verify that these assumptions are fulfilled. In the same way, some measurement scenarios are too complex (if fact most of the biological scenarios are too complex) to present an optical behavior that can be accurately assessed by MC methods. Approximations must always be made and, as before, it is quite a hard task to precisely evaluate the effects and the influence of those approximations on the results. The performance of both the LUT and the ratios based approaches relies almost exclusively on the calibration process. Therefore, these techniques are very sensitive to the conditions in which this calibration is performed and its efficiency can be easily affected by external factors.

In cases in which the effectiveness of one of these classical methods cannot be guaranteed, Blind signal separation (BSS) techniques can be an alternative to re-establish the performance of a DRS instrument. Even though there are many approaches, generally speaking BSS methods allow to separate the results of an observation into constituent signals.

10. REFERENCES

1. A. Marandi, C. W. Rudy, V. G. Plotnichenko, E. M. Dianov, K. L. Vodopyanov, and R. L. Byer, "Mid-infrared supercontinuum generation in tapered chalcogenide fiber for producing octave-spanning frequency comb around 3 μm.," Opt. Express **20**, 24218–25 (2012).

2. B. Kuyken, T. Ideguchi, S. Holzner, M. Yan, T. W. Hänsch, J. Van Campenhout, P. Verheyen, S. Coen, F. Leo, R. Baets, G. Roelkens, and N. Picqué, "An octave-spanning mid-infrared frequency comb generated in a silicon nanophotonic wire waveguide.," Nat. Commun. **6**, 6310 (2015).

3. R. D. L. Kronig, "On the theory of dispersion of x-rays," J. Opt. Soc. Am. **12**, 547 (1926).

4. H. A. Kramers, "La diffusion de la lumiere par les atomes," Atti del Congr. Internazionale dei Fis. **2**, 545–557 (1927).

5. L. S. Rothman, I. E. Gordon, Y. Babikov, A. Barbe, D. C. Benner, P. F. Bernath, M. Birk, L. Bizzocchi, V. Boudon, L. R. Brown, A. Campargue, K. Chance, L. H. Coudert, V. M. Devi, B. J. Drouin, A. Fayt, J.-M. Flaud, R. R. Gamache, J. Harrison, J.-M. Hartmann, C. Hill, J. T. Hodges, D. Jacquemart, A. Jolly, J. Lamouroux, R. J. LeRoy, G. Li, D. Long, C. J. Mackie, S. T. Massie, S. Mikhailenko, H. S. P. Müller, O. V. Naumenko, A. V. Nikitin, J. Orphal, V. I. Perevalov, A. Perrin, E. R. Polovtseva, C. Richard, M. A. H. Smith, E. Starikova, K. Sung, S. A. Tashkun, J. Tennyson, G. C. Toon, V. G. Tyuterev, and G. Wagner, "The HITRAN 2012 Molecular Spectroscopic Database," J. Quant. Spectrosc. Radiat. Transf. (2013).

6. T. Durduran, R. Choe, W. B. Baker, and A. G. Yodh, "Diffuse optics for tissue monitoring and tomography," Reports Prog. Phys. **73**, 076701 (2010).

7. A. J. Welch and M. J. C. van Gemert, *Optical-Thermal Response of Laser-Irradiated Tissue* (Springer Science & Business Media, 2011).

8. V. Tuchin, *Tissue Optics: Light Scattering Methods and Instruments for Medical Diagnosis*, 2nd Editio (SPIE Press, 2007).

9. J. A. Garcia-Souto, P. Martin-Mateos, J. E. Posada, P. Acedo, and D. A. Jackson, "Evaluation of a 1540nm VCSEL for fibre Bragg gratings interrogation in dynamic measurement applications," in *OFS2014 23rd International Conference on Optical Fiber Sensors* (International Society for Optics and Photonics, 2014), p. 91573A.

10. C. Gierl, T. Gruendl, P. Debernardi, K. Zogal, C. Grasse, H. A. Davani, G. Böhm, S. Jatta, F. Küppers, P. Meissner, and M.-C. Amann, "Surface micromachined tunable 1.55 μm-VCSEL with 102 nm continuous single-mode tuning.," Opt. Express **19**, 17336–43 (2011).

11. J. Reid, J. Shewchun, B. K. Garside, and E. A. Ballik, "High sensitivity pollution detection employing tunable diode lasers.," Appl. Opt. **17**, 300–7 (1978).

12. F. Slemr, G. W. Harris, D. R. Hastie, G. I. Mackay, and H. I. Schiff, "Measurement of gas phase hydrogen peroxide in air by tunable diode laser absorption spectroscopy," J. Geophys. Res. **91**, 5371 (1986).

13. M. Lengden, R. Cunningham, and W. Johnstone, "Tuneable diode laser gas analyser for methane measurements on a large scale solid oxide fuel cell," J. Power Sources **196**, 8406–8408 (2011).

14. B. Lins, P. Zinn, R. Engelbrecht, and B. Schmauss, "Simulation-based comparison of noise effects in wavelength modulation spectroscopy and direct absorption TDLAS," Appl. Phys. B **100**, 367–376 (2010).

15. J. Reid, M. El-Sherbiny, B. K. Garside, and E. A. Ballik, "Sensitivity limits of a tunable diode laser spectrometer, with application to the detection of NO(2) at the 100-ppt level.," Appl. Opt. **19**, 3349–53 (1980).

16. H. I. Schiff, D. R. Hastie, G. I. Mackay, T. Iguchi, and B. A. Ridley, "Tunable diode laser systems for measuring trace gases intropospheric air.," Environ. Sci. Technol. **17**, 352A–64A (1983).

17. J. A. Silver, "Frequency-modulation spectroscopy for trace species detection: theory and comparison among experimental methods.," Appl. Opt. **31**, 707–17 (1992).

18. G. Peach, "Theory of the pressure broadening and shift of spectral lines," Adv. Phys. **30**, 367–474 (2006).

19. J. Hodgkinson and R. P. Tatam, "Optical gas sensing: a review," Meas. Sci. Technol. **24**, 012004 (2013).

20. G. C. Bjorklund, "Frequency-modulation spectroscopy: a new method for measuring weak absorptions and dispersions," Opt. Lett. **5**, 15 (1980).

21. W. Lenth, "Optical heterodyne spectroscopy with frequency- and amplitude-modulated semiconductor lasers," Opt. Lett. **8**, 575 (1983).

22. P. Werle, P., "Spectroscopic trace gas analysis using semiconductor diode lasers," Spectrochim. Acta. A **52**, 805 – 822 (1996).

23. M. Gehrtz, G. C. Bjorklund, and E. A. Whittaker, "Quantum-limited laser frequency-modulation spectroscopy," J. Opt. Soc. Am. B **2**, 1510 (1985).

24. D. E. Cooper and T. F. Gallagher, "Double frequency modulation spectroscopy: high modulation frequency with low-bandwidth detectors," Appl. Opt. **24**, 1327 (1985).

25. G. R. Janik, C. B. Carlisle, and T. F. Gallagher, "Two-tone frequency-modulation spectroscopy," J. Opt. Soc. Am. B **3**, 1070 (1986).

26. D. E. Cooper and J. P. Watjen, "Two-tone optical heterodyne spectroscopy with a tunable lead-salt diode laser," Opt. Lett. **11**, 606 (1986).

27. P. Malara, M. F. Witinski, G. Gagliardi, and P. De Natale, "Two-tone frequency-modulation spectroscopy in off-axis cavity.," Opt. Lett. **38**, 4625–8 (2013).

28. D. T. Cassidy and J. Reid, "Atmospheric pressure monitoring of trace gases using tunable diode lasers.," Appl. Opt. **21**, 1185–90 (1982).

29. K. Uehara and H. Tai, "Remote detection of methane with a 1.66-microm diode laser.," Appl. Opt. **31**, 809–14 (1992).

30. T. Iseki, H. Tai, and K. Kimura, "A portable remote methane sensor using a tunable diode laser," Meas. Sci. Technol. **11**, 594–602 (2000).

31. G. B. Rieker, J. B. Jeffries, and R. K. Hanson, "Calibration-free wavelength-modulation spectroscopy for measurements of gas temperature and concentration in harsh environments.," Appl. Opt. **48**, 5546–60 (2009).

32. J. R. P. Bain, W. Johnstone, K. Ruxton, G. Stewart, M. Lengden, and K. Duffin, "Recovery of Absolute Gas Absorption Line Shapes Using Tunable Diode Laser Spectroscopy With Wavelength Modulation—Part 2: Experimental Investigation," J. Light. Technol. **29**, 987–996 (2011).

33. K. Sun, X. Chao, R. Sur, C. S. Goldenstein, J. B. Jeffries, and R. K. Hanson, "Analysis of calibration-free wavelength-scanned wavelength modulation spectroscopy for practical gas sensing using tunable diode lasers," Meas. Sci. Technol. **24**, 125203 (2013).

34. V. Hasson, A. J. D. Farmer, and R. W. Nicholls, "Application of dispersion techniques to molecular band intensity measurements. I. Principles of "fringe shift" and "fringe slope" band analysis procedures," J. Phys. B At. Mol. Phys. **5**, 1241–1247 (1972).

35. M Crance, P Juncar and J Pinard, "A new method for measuring relative oscillator strengths using a CW dye laser," J. Phys. B At. Mol. Phys. **8**, 2461 (1975).

36. A. B. Duval and A. I. McIntosh, "Measurement of oscillator strength by tunable laser interferometry," J. Phys. D. Appl. Phys. **13**, 1617–1624 (1980).

37. S. Marchetti and R. Simili, "Measurement of the refractive index dispersion around an absorbing line," Opt. Commun. **249**, 37–41 (2005).

38. J. J. Moschella, R. C. Hazelton, and M. D. Keitz, "Resonant, heterodyne laser interferometer for state density measurements in atoms and ions," Rev. Sci. Instrum. **77**, 093108 (2006).

39. J. Ye, L.-S. Ma, and J. L. Hall, "Ultrasensitive detections in atomic and molecular physics: demonstration in molecular overtone spectroscopy," J. Opt. Soc. Am. B **15**, 6 (1998).

40. B. M. Siller, M. W. Porambo, A. A. Mills, and B. J. McCall, "Noise immune cavity enhanced optical heterodyne velocity modulation spectroscopy.," Opt. Express **19**, 24822–7 (2011).

41. A. Foltynowicz, W. Ma, and O. Axner, "Characterization of fiber-laser-based sub-Doppler NICE-OHMS for quantitative trace gas detection.," Opt. Express **16**, 14689–702 (2008).

42. P. Ehlers, I. Silander, J. Wang, A. Foltynowicz, and O. Axner, "Fiber-laser-based noise-immune cavity-enhanced optical heterodyne molecular spectrometry incorporating an optical circulator.," Opt. Lett. **39**, 279–82 (2014).

43. A. Foltynowicz, F. M. Schmidt, W. Ma, and O. Axner, "Noise-immune cavity-enhanced optical heterodyne molecular spectroscopy: Current status and future potential," Appl. Phys. B **92**, 313–326 (2008).

44. G. Wysocki and D. Weidmann, "Molecular dispersion spectroscopy for chemical sensing using chirped mid-infrared quantum cascade laser.," Opt. Express **18**, 26123–40 (2010).

45. P. R. Griffiths and J. A. De Haseth, *Fourier Transform Infrared Spectrometry*, 2nd Editio (John Wiley & Sons, Inc., 2007).

46. P. Hermann, A. Hoehl, G. Ulrich, C. Fleischmann, A. Hermelink, B. Kästner, P. Patoka, A. Hornemann, B. Beckhoff, E. Rühl, and G. Ulm, "Characterization of semiconductor materials using synchrotron radiation-based near-field infrared microscopy and nano-FTIR spectroscopy.," Opt. Express **22**, 17948–58 (2014).

47. Y. Liu, W. R. Windham, K. C. Lawrence, and B. Park, "Simple Algorithms for the Classification of Visible/Near-Infrared and

Hyperspectral Imaging Spectra of Chicken Skins, Feces, and Fecal Contaminated Skins," Appl. Spectrosc. **57**, 1609–1612 (2003).

48. Q. Chen, J. Cai, X. Wan, and J. Zhao, "Application of linear/non-linear classification algorithms in discrimination of pork storage time using Fourier transform near infrared (FT-NIR) spectroscopy," LWT - Food Sci. Technol. **44**, 2053–2058 (2011).

49. C. J. Cochrane and J. Blacksberg, "A Fast Classification Scheme in Raman Spectroscopy for the Identification of Mineral Mixtures Using a Large Database With Correlated Predictors," IEEE Trans. Geosci. Remote Sens. **53**, 4259–4274 (2015).

50. M. E. Keating, H. Nawaz, F. Bonnier, and H. J. Byrne, "Multivariate statistical methodologies applied in biomedical Raman spectroscopy: assessing the validity of partial least squares regression using simulated model datasets.," Analyst **140**, 2482–92 (2015).

51. Y. J. Kim, S. Kim, J. W. Kim, and G. Yoon, "Data preprocessing and partial least squares regression analysis for reagentless determination of hemoglobin concentrations using conventional and total transmission spectroscopy.," J. Biomed. Opt. **6**, 177–82 (2001).

52. X.-X. Zhang, J.-H. Yin, Z.-H. Mao, and Y. Xia, "Discrimination of healthy and osteoarthritic articular cartilages by Fourier transform infrared imaging and partial least squares-discriminant analysis.," J. Biomed. Opt. **20**, 60501 (2015).

53. M. Nikodem and G. Wysocki, "Chirped laser dispersion spectroscopy for remote open-path trace-gas sensing.," Sensors **12**, 16466–81 (2012).

54. M. Nikodem, D. Weidmann, and G. Wysocki, "Chirped laser dispersion spectroscopy with harmonic detection of molecular spectra," Appl. Phys. B **109**, 477–483 (2012).

55. M. Detto, J. Verfaillie, F. Anderson, L. Xu, and D. Baldocchi, "Comparing laser-based open- and closed-path gas analyzers to measure methane fluxes using the eddy covariance method," Agric. For. Meteorol. **151**, 1312–1324 (2011).

56. P. Martín-Mateos and P. Acedo, "Heterodyne phase-sensitive detection for calibration-free molecular dispersion spectroscopy.," Opt. Express **22**, 15143–53 (2014).

57. J. Karle, "Some developments in anomalous dispersion for the structural investigation of macromolecular systems in biology," Int. J. Quantum Chem. **18**, 357–367 (2009).

58. W. A. Hendrickson, J. L. Smith, R. P. Phizackerley, and E. A. Merritt, "Crystallographic structure analysis of lamprey hemoglobin from anomalous dispersion of synchrotron radiation," Proteins Struct. Funct. Genet. **4**, 77–88 (1988).

59. K. Franz, D. Weidmann, and G. Wysocki, "High Dynamic Range Laser Dispersion Spectroscopy of Saturated Absorption Lines," in *Conference on Lasers and Electro-Optics 2010* (OSA, 2010), p. CMJ4.

60. M. Nikodem, D. Weidmann, C. Smith, and G. Wysocki, "Signal-to-noise ratio in chirped laser dispersion spectroscopy.," Opt. Express **20**, 644–53 (2012).

61. G. Plant, M. Nikodem, D. M. Sonnenfroh, and G. Wysocki, "Chirped Laser Dispersion Spectroscopy for Remote Sensing of Methane at 1.65μm - Analysis of System Performance," in *CLEO: 2013* (OSA, 2013), p. JW2A.79.

62. M. Nikodem, G. Plant, Z. Wang, P. Prucnal, and G. Wysocki, "Chirped lasers dispersion spectroscopy implemented with single- and dual-sideband electro-optical modulators.," Opt. Express **21**, 14649–55 (2013).

63. S. Schiller, "Spectrometry with frequency combs," Opt. Lett. **27**, 766 (2002).

64. F. Keilmann, C. Gohle, and R. Holzwarth, "Time-domain mid-infrared frequency-comb spectrometer," Opt. Lett. **29**, 1542 (2004).

65. L. C. Sinclair, I. Coddington, W. C. Swann, G. B. Rieker, A. Hati, K. Iwakuni, and N. R. Newbury, "Operation of an optically coherent frequency comb outside the metrology lab.," Opt. Express **22**, 6996–7006 (2014).

66. T. Udem, J. Reichert, R. Holzwarth, and T. W. Hänsch, "Accurate measurement of large optical frequency differences with a mode-locked laser," Opt. Lett. **24**, 881 (1999).

67. M. Niering, R. Holzwarth, J. Reichert, P. Pokasov, T. Udem, M. Weitz, T. Hansch, P. Lemonde, G. Santarelli, M. Abgrall, P. Laurent, C. Salomon, and A. Clairon, "Measurement of the hydrogen 1S- 2S transition frequency by phase coherent comparison with a microwave cesium fountain clock," Phys. Rev. Lett. **84**, 5496–9 (2000).

68. S. A. Diddams, D. J. Jones, L.-S. Ma, S. T. Cundiff, and J. L. Hall, "Optical frequency measurement across a 104-THz gap with a femtosecond laser frequency comb," Opt. Lett. **25**, 186 (2000).

69. J. Stenger, C. Tamm, N. Haverkamp, S. Weyers, and H. R. Telle, "Absolute frequency measurement of the 435.5-nm (171)Yb+-clock transition with a Kerr-lens mode-locked femtosecond laser," Opt. Lett. **26**, 1589 (2001).

70. S. A. Diddams, D. J. Jones, S. T. Cundiff, J. L. Hall, J. K. Ranka, R. S. Windeler, and A. J. Stent, "A direct rf to optical frequency measurement with a femtosecond laser comb spanning 300 THz," in *Quantum Electronics and Laser Science Conference* (Optical Society of America, 2000), p. QWF2.

71. S. A. Diddams, "The evolving optical frequency comb," J. Opt. Soc. Am. B **27**, B51 (2010).

72. T. Udem, R. Holzwarth, and T. W. Hänsch, "Optical frequency metrology.," Nature **416**, 233–7 (2002).

73. T. Udem and F. Riehle, "Frequency Combs applications and optical frequency standards," (2007).

74. A. Foltynowicz, P. Masłowski, T. Ban, F. Adler, K. C. Cossel, T. C. Briles, and J. Ye, "Optical frequency comb spectroscopy.," Faraday Discuss. **150**, 23–31(2011).

75. G. B. Rieker, F. R. Giorgetta, W. C. Swann, J. Kofler, A. M. Zolot, L. C. Sinclair, E. Baumann, C. Cromer, G. Petron, C. Sweeney, P. P. Tans, I. Coddington, and N. R. Newbury, "Frequency-comb-based remote

sensing of greenhouse gases over kilometer air paths," Optica **1**, 290 (2014).

76. A. Bartels and H. Kurz, "Generation of a broadband continuum by a Ti:sapphire femtosecond oscillator with a 1-GHz repetition rate.," Opt. Lett. **27**, 1839–41 (2002).

77. N. R. Newbury, "Searching for applications with a fine-tooth comb," Nat. Photonics **5**, 186–188 (2011).

78. J. Reichert, M. Niering, R. Holzwarth, M. Weitz, T. Udem, and T. Hänsch, "Phase Coherent Vacuum-Ultraviolet to Radio Frequency Comparison with a Mode-Locked Laser," Phys. Rev. Lett. **84**, 3232–3235 (2000).

79. A. Poppe, R. Holzwarth, A. Apolonski, G. Tempea, C. Spielmann, T. W. Hänsch, and F. Krausz, "Few-cycle optical waveform synthesis," Appl. Phys. B **72**, 373–376 (2001).

80. J. Reichert, R. Holzwarth, T. Udem, and T. W. Hänsch, "Measuring the frequency of light with mode-locked lasers," Opt. Commun. **172**, 59–68 (1999).

81. A. Marian, "United Time-Frequency Spectroscopy for Dynamics and Global Structure," Science **306**, 2063–2068 (2004).

82. V. Gerginov, C. E. Tanner, S. A. Diddams, A. Bartels, and L. Hollberg, "High-resolution spectroscopy with a femtosecond laser frequency comb," Opt. Lett. **30**, 1734 (2005).

83. S. Yefet and A. Pe'er, "A Review of Cavity Design for Kerr Lens Mode-Locked Solid-State Lasers," Appl. Sci. **3**, 694–724 (2013).

84. D. E. Spence, P. N. Kean, and W. Sibbett, "60-fsec pulse generation from a self-mode-locked Ti:sapphire laser," Opt. Lett. **16**, 42 (1991).

85. M. S. Kirchner, T. M. Fortier, A. Bartels, and S. A. Diddams, "A low-threshold self-referenced Ti:Sapphire optical frequency comb," Opt. Express **14**, 9531 (2006).

86. Z. Volynskaya, A. S. Haka, K. L. Bechtel, M. Fitzmaurice, R. Shenk, N. Wang, J. Nazemi, R. R. Dasari, and M. S. Feld, "Diagnosing breast cancer using diffuse reflectance spectroscopy and intrinsic fluorescence spectroscopy.," J. Biomed. Opt. **13**, 024012 (2011).

87. J. C. Knight, T. A. Birks, P. S. J. Russell, and D. M. Atkin, "All-silica single-mode optical fiber with photonic crystal cladding," Opt. Lett. **21**, 1547 (1996).

88. J. K. Ranka, R. S. Windeler, and A. J. Stentz, "Visible continuum generation in air-silica microstructure optical fibers with anomalous dispersion at 800 nm," Opt. Lett. **25**, 25 (2000).

89. B. R. Washburn, S. A. Diddams, N. R. Newbury, J. W. Nicholson, M. F. Yan, and C. G. Jrgensen, "Phase-locked, erbium-fiber-laser-based frequency comb in the near infrared," Opt. Lett. **29**, 250 (2004).

90. N. R. Newbury and W. C. Swann, "Low-noise fiber-laser frequency combs," J. Opt. Soc. Am. B **24**, 1756 (2007).

91. Y. Kim, S. Kim, Y.-J. Kim, H. Hussein, and S.-W. Kim, "Er-doped fiber frequency comb with mHz relative linewidth," Opt. Express **17**, 11972 (2009).

92. I. Coddington, W. C. Swann, and N. R. Newbury, "Coherent dual-comb spectroscopy at high signal-to-noise ratio," Phys. Rev. A **82**, 043817 (2010).

93. C. Gohle, B. Stein, A. Schliesser, T. Udem, and T. Hänsch, "Frequency Comb Vernier Spectroscopy for Broadband, High-Resolution, High-Sensitivity Absorption and Dispersion Spectra," Phys. Rev. Lett. **99**, 263902 (2007).

94. M. J. Thorpe, D. Balslev-Clausen, M. S. Kirchner, and J. Ye, "Cavity-enhanced optical frequency comb spectroscopy: application to human breath analysis," Opt. Express **16**, 2387 (2008).

95. S. Xiao and A. Weiner, "2-D wavelength demultiplexer with potential for ≥ 1000 channels in the C-band.," Opt. Express **12**, 2895–902 (2004).

96. S. A. Diddams, L. Hollberg, and V. Mbele, "Molecular fingerprinting with the resolved modes of a femtosecond laser frequency comb.," Nature **445**, 627–30 (2007).

97. E. Baumann, F. R. Giorgetta, W. C. Swann, A. M. Zolot, I. Coddington, and N. R. Newbury, "Spectroscopy of the methane ν3 band with an accurate midinfrared coherent dual-comb spectrometer," Phys. Rev. A **84**, 062513 (2011).

98. R. W. P. Drever, J. L. Hall, F. V. Kowalski, J. Hough, G. M. Ford, A. J. Munley, and H. Ward, "Laser phase and frequency stabilization using an optical resonator," Appl. Phys. B Photophysics Laser Chem. **31**, 97–105 (1983).

99. B. Bernhardt, E. Sorokin, P. Jacquet, R. Thon, T. Becker, I. T. Sorokina, N. Picqué, and T. W. Hänsch, "Mid-infrared dual-comb spectroscopy with 2.4 μm Cr2+:ZnSe femtosecond lasers," Appl. Phys. B **100**, 3–8 (2010).

100. B. Bernhardt, A. Ozawa, P. Jacquet, M. Jacquey, Y. Kobayashi, T. Udem, R. Holzwarth, G. Guelachvili, T. W. Hänsch, and N. Picqué, "Cavity-enhanced dual-comb spectroscopy," Nat. Photonics **4**, 55–57 (2009).

101. I. Coddington, W. C. Swann, L. Nenadovic, and N. R. Newbury, "Rapid and precise absolute distance measurements at long range," Nat. Photonics **3**, 351–356 (2009).

102. A. Schliesser, M. Brehm, F. Keilmann, and D. W. van der Weide, "Frequency-comb infrared spectrometer for rapid, remote chemical sensing," Opt. Express **13**, 9029 (2005).

103. A. M. Zolot, F. R. Giorgetta, E. Baumann, J. W. Nicholson, W. C. Swann, I. Coddington, and N. R. Newbury, "Direct-comb molecular spectroscopy with accurate, resolved comb teeth over 43 THz.," Opt. Lett. **37**, 638–40 (2012).

104. G. Villares, A. Hugi, S. Blaser, and J. Faist, "Dual-comb spectroscopy based on quantum-cascade-laser frequency combs.," Nat. Commun. **5**, 5192 (2014).

105. J. Mandon, G. Guelachvili, and N. Picqué, "Fourier transform spectroscopy with a laser frequency comb," Nat. Photonics **3**, 99–102 (2009).

106. S. P. Davis, M. C. Abrams, and J. W. Brault, *Fourier Transform Spectrometry* (Elsevier Inc., 2001).

107. T. Sakamoto, T. Kawanishi, and M. Izutsu, "Widely wavelength-tunable ultra-flat frequency comb generation using conventional dual-drive Mach-Zehnder modulator," Electron. Lett. **43**, 1039 (2007).

108. R. Yang, F. Pollinger, K. Meiners-Hagen, J. Tan, and H. Bosse, "Heterodyne multi-wavelength absolute interferometry based on a cavity-enhanced electro-optic frequency comb pair.," Opt. Lett. **39**, 5834–7 (2014).

109. K. Aoki, A. Kondo, T. Ejiri, Y. Iwata, A. Hamajima, T. Mori, Y. Mizuno, M. Imaeda, Y. Kozuka, O. Mitomi, and M. Minakata, "High-speed and low-driving-Voltage thin-sheet X-cut LiNbO/sub 3/ Modulator with laminated low-dielectric-constant adhesive," IEEE Photonics Technol. Lett. **17**, 2077–2079 (2005).

110. M. Sugiyama, M. Doi, S. Taniguchi, T. Nakazawa, and H. Onaka, "Driver-less 40 Gb/s LiNbO3 Modulator with Sub-1 V Drive Voltage - OSA Trends in Optics and Photonics," in *Optical Fiber Communications Conference*, A. Sawchuk, ed. (Optical Society of America, 2002), Vol. 70, p. FB6.

111. R. Wu, V. Torres-Company, D. E. Leaird, and A. M. Weiner, "Supercontinuum-based 10-GHz flat-topped optical frequency comb generation.," Opt. Express **21**, 6045–52 (2013).

112. T. Ideguchi, A. Poisson, G. Guelachvili, N. Picqué, and T. W. Hänsch, "Adaptive real-time dual-comb spectroscopy.," Nat. Commun. **5**, 3375 (2014).

113. D. A. Long, A. J. Fleisher, K. O. Douglass, S. E. Maxwell, K. Bielska, J. T. Hodges, and D. F. Plusquellic, "Multiheterodyne spectroscopy with optical frequency combs generated from a continuous-wave laser.," Opt. Lett. **39**, 2688–90 (2014).

114. P. Martín-Mateos, B. Jerez, and P. Acedo, "Heterodyne architecture for tunable laser chirped dispersion spectroscopy using optical processing," Opt. Lett. **39**, 1–3 (2014).

115. A. Yodh and B. Chance, "Spectroscopy and Imaging with Diffusing Light," Phys. Today **48**, 34 (1995).

116. J. L. Sandell and T. C. Zhu, "A review of in-vivo optical properties of human tissues and its impact on PDT.," J. Biophotonics **4**, 773–87 (2011).

117. S.-H. Tseng, P. Bargo, A. Durkin, and N. Kollias, "Chromophore concentrations, absorption and scattering properties of human skin in-vivo.," Opt. Express **17**, 14599–617 (2009).

118. A. Vogel, V. V Chernomordik, J. D. Riley, M. Hassan, F. Amyot, B. Dasgeb, S. G. Demos, R. Pursley, R. F. Little, R. Yarchoan, Y. Tao, and A. H. Gandjbakhche, "Using noninvasive multispectral imaging to quantitatively assess tissue vasculature.," J. Biomed. Opt. **12**, 051604 (2011).

119. I. Nishidate, N. Tanaka, T. Kawase, T. Maeda, T. Yuasa, Y. Aizu, T. Yuasa, and K. Niizeki, "Noninvasive imaging of human skin hemodynamics using a digital red-green-blue camera.," J. Biomed. Opt. **16**, 086012 (2011).

120. K. Gurley, Y. Shang, and G. Yu, "Noninvasive optical quantification of absolute blood flow, blood oxygenation, and oxygen consumption rate in exercising skeletal muscle," J. Biomed. Opt. **17**, 0750101 (2012).

121. S.-H. Tseng, C.-K. Hsu, J. Yu-Yun Lee, S.-Y. Tzeng, W.-R. Chen, and Y.-K. Liaw, "Noninvasive evaluation of collagen and hemoglobin contents and scattering property of in vivo keloid scars and normal skin using diffuse reflectance spectroscopy: pilot study.," J. Biomed. Opt. **17**, 077005 (2012).

122. R. Nachabe, B. H. W. Hendriks, A. E. Desjardins, M. van der Voort, M. B. van der Mark, and H. J. C. M. Sterenborg, "Estimation of lipid and water concentrations in scattering media with diffuse optical spectroscopy from 900 to 1600 nm," J. Biomed. Opt. **15**, 037015 (2010).

123. P. C. Sekhar, J. Betsy, J. Presanthila, and N. Subhash, "Discrimination of periodontal diseases using diffuse reflectance spectral intensity ratios.," J. Biomed. Opt. **17**, 027001 (2012).

124. R. H. Wilson, M. Chandra, L.-C. Chen, W. R. Lloyd, J. Scheiman, D. Simeone, J. Purdy, B. McKenna, and M.-A. Mycek, "Photon-tissue interaction model enables quantitative optical analysis of human pancreatic tissues.," Opt. Express **18**, 21612–21 (2010).

125. L. Khaodhiar, T. Dinh, K. T. Schomacker, S. V Panasyuk, J. E. Freeman, R. Lew, T. Vo, A. A. Panasyuk, C. Lima, J. M. Giurini, T. E. Lyons, and A. Veves, "The use of medical hyperspectral technology to evaluate microcirculatory changes in diabetic foot ulcers and to predict clinical outcomes.," Diabetes Care **30**, 903–10 (2007).

126. D. Yudovsky, A. Nouvong, K. Schomacker, and L. Pilon, "Monitoring temporal development and healing of diabetic foot ulceration using hyperspectral imaging.," J. Biophotonics **4**, 565–76 (2011).

127. V. Prabhu, S. B. S. Rao, S. Chandra, P. Kumar, L. Rao, V. Guddattu, K. Satyamoorthy, and K. K. Mahato, "Spectroscopic and histological evaluation of wound healing progression following Low Level Laser Therapy (LLLT).," J. Biophotonics **5**, 168–84 (2012).

128. A. Garcia-Uribe, E. B. Smith, J. Zou, M. Duvic, V. Prieto, and L. V Wang, "In-vivo characterization of optical properties of pigmented skin lesions including melanoma using oblique incidence diffuse reflectance spectrometry.," J. Biomed. Opt. **16**, 020501 (2011).

129. I. Kuzmina, I. Diebele, D. Jakovels, J. Spigulis, L. Valeine, J. Kapostinsh, and A. Berzina, "Towards noncontact skin melanoma selection by multispectral imaging analysis.," J. Biomed. Opt. **16**, 060502 (2011).

130. T. J. Farrell, M. S. Patterson, and B. Wilson, "A diffusion theory model of spatially resolved, steady-state diffuse reflectance for the noninvasive determination of tissue optical properties in vivo.," Med. Phys. **19**, 879–88 (1992).

131. A. H. Gandjbakhche and G. H. Weiss, "V: Random Walk and Diffusion-Like Models of Photon Migration in Turbid Media," **34**, 333–402 (1995).

132. C. Zhu and Q. Liu, "Review of Monte Carlo modeling of light transport in tissues.," J. Biomed. Opt. **18**, 50902 (2013).

133. R. Hennessy, S. L. Lim, M. K. Markey, and J. W. Tunnell, "Monte Carlo lookup table-based inverse model for extracting optical properties from tissue-simulating phantoms using diffuse reflectance spectroscopy.," J. Biomed. Opt. **18**, 037003 (2013).

134. S.-H. Tseng and M.-F. Hou, "Efficient determination of the epidermal optical properties using a diffusion model-based approach: Monte Carlo studies.," J. Biomed. Opt. **16**, 087007 (2011).

135. A. Hyvärinen and E. Oja, "Independent component analysis: algorithms and applications," Neural Networks **13**, 411–430 (2000).

136. J.-F. Cardoso, "Blind signal separation: statistical principles," Proc. IEEE **86**, 2009–2025 (1998).

137. K. Pearson, "On lines and planes of closest fit to systems of points in space," Philos. Mag. Ser. 6 **2**, 559–572 (1901).

138. A. Hyvärinen, "Fast and robust fixed-point algorithms for independent component analysis.," IEEE Trans. Neural Netw. **10**, 626–34 (1999).

139. A. Eguizabal, A. M. Laughney, P. B. García-Allende, V. Krishnaswamy, W. A. Wells, K. D. Paulsen, B. W. Pogue, J. M. Lopez-Higuera, and O. M. Conde, "Direct identification of breast cancer pathologies using blind separation of label-free localized reflectance measurements.," Biomed. Opt. Express **4**, 1104–18 (2013).

140. J. A. M. Bispo, E. E. de Sousa Vieira, L. Silveira, and A. B. Fernandes, "Correlating the amount of urea, creatinine, and glucose in urine from patients with diabetes mellitus and hypertension with the risk of developing renal lesions by means of Raman spectroscopy and principal component analysis.," J. Biomed. Opt. **18**, 87004 (2013).

141. A. Croitor Sava, D. M. Sima, M. C. Martinez-Bisbal, B. Celda, and S. Van Huffel, "Non-negative blind source separation techniques for tumor tissue typing using HR-MAS signals.," Conf. Proc. IEEE Eng. Med. Biol. Soc. **2010**, 3658–61 (2010).

142. J. Chen and X. Z. Wang, "A new approach to near-infrared spectral data analysis using independent component analysis.," J. Chem. Inf. Comput. Sci. **41**, 992–1001 (n.d.).

143. S. MacNeil, "Progress and opportunities for tissue-engineered skin.," Nature **445**, 874–80 (2007).

144. L. Martínez-Santamaría, S. Guerrero-Aspizua, and M. Del Río, "Skin bioengineering: preclinical and clinical applications.," Actas Dermosifiliogr. **103**, 5–11 (2012).

145. M. Carretero, M. J. Escámez, F. Prada, I. Mirones, M. García, A. Holguín, B. Duarte, O. Podhajcer, J. L. Jorcano, F. Larcher, and M. Del Río, "Skin gene therapy for acquired and inherited disorders.," Histol. Histopathol. **21**, 1233–47 (2006).

146. M. J. Escámez, M. Carretero, M. García, L. Martínez-Santamaría, I. Mirones, B. Duarte, A. Holguín, E. García, V. García, A. Meana, J. L. Jorcano, F. Larcher, and M. Del Río, "Assessment of optimal virus-mediated growth factor gene delivery for human cutaneous wound healing enhancement.," J. Invest. Dermatol. **128**, 1565–75 (2008).

147. M. J. Leahy, J. G. Enfield, N. T. Clancy, J. O'Doherty, P. McNamara, and G. E. Nilsson, "Biophotonic methods in microcirculation imaging," Med. Laser Appl. **22**, 105–126 (2007).

148. A. Ishimaru, "Diffusion of light in turbid material.," Appl. Opt. **28**, 2210–5 (1989).

149. D. de F. T. da Silva, B. de C. Vidal, D. M. Zezell, T. M. T. Zorn, S. C. Núñez, and M. S. Ribeiro, "Collagen birefringence in skin repair in response to red polarized-laser therapy.," J. Biomed. Opt. **11**, 024002 (2006).

150. J. M. Kainerstorfer, M. Ehler, F. Amyot, M. Hassan, S. G. Demos, V. Chernomordik, C. K. Hitzenberger, A. H. Gandjbakhche, and J. D.

Riley, "Principal component model of multispectral data for near real-time skin chromophore mapping.," J. Biomed. Opt. **15**, 046007 (2010).

151. L. C. Clark and C. Lyons, "Electrode systems for continuous monitoring in cardiovascular surgery.," Ann. N. Y. Acad. Sci. **102**, 29–45 (1962).

152. L. C. Clark, R. Wolf, D. Granger, and Z. Taylor, "Continuous recording of blood oxygen tensions by polarography.," J. Appl. Physiol. **6**, 189–93 (1953).

153. Y. Degani and A. Heller, "Direct electrical communication between chemically modified enzymes and metal electrodes. I. Electron transfer from glucose oxidase to metal electrodes via electron relays, bound covalently to the enzyme," J. Phys. Chem. **91**, 1285–1289 (1987).

154. M. V. Pishko, I. Katakis, S.-E. Lindquist, L. Ye, B. A. Gregg, and A. Heller, "Direct Electrical Communication between Graphite Electrodes and Surface Adsorbed Glucose Oxidase/Redox Polymer Complexes," Angew. Chemie Int. Ed. English **29**, 82–84 (1990).

155. B. Palys, A. Bokun, and J. Rogalski, "Poly-o-phenylenediamine as redox mediator for laccase," Electrochim. Acta **52**, 7075–7082 (2007).

156. A. R. Vijayakumar, E. Csöregi, A. Heller, and L. Gorton, "Alcohol biosensors based on coupled oxidase-peroxidase systems," Anal. Chim. Acta **327**, 223–234 (1996).

157. G. Wohlfahrt, S. Witt, J. Hendle, D. Schomburg, H. M. Kalisz, and H. J. Hecht, "1.8 and 1.9 A resolution structures of the Penicillium amagasakiense and Aspergillus niger glucose oxidases as a basis for modelling substrate complexes.," Acta Crystallogr. D. Biol. Crystallogr. **55**, 969–77 (1999).

158. O. Courjean, F. Gao, and N. Mano, "Deglycosylation of Glucose Oxidase for Direct and Efficient Glucose Electrooxidation on a Glassy Carbon Electrode," Angew. Chemie **121**, 6011–6013 (2009).

159. N. Moodley, U. Ngxamngxa, M. J. Turzyniecka, and T. S. Pillay, "Historical perspectives in clinical pathology: a history of glucose measurement.," J. Clin. Pathol. **68**, 258–264 (2015).

160. C. F. Blanford, "The birth of protein electrochemistry," Chem. Commun. **49**, 11130 (2013).

161. A. Sols and G. De La Fuente, "Glucose oxidase as an analytic reagent.," Rev. española Fisiol. **13**, 231–45 (1957).

162. F. Heinz and T. W. Beushausen, "A new enzymatic method for the determination of glucose.," J. Clin. Chem. Clin. Biochem. **19**, 977–8 (1981).

163. B. Z. Cavari and G. Phelps, "Sensitive enzymatic assay for glucose determination in natural waters.," Appl. Environ. Microbiol. **33**, 1237–43 (1977).

164. A. E. Cass, G. Davis, G. D. Francis, H. A. Hill, W. J. Aston, I. J. Higgins, E. V Plotkin, L. D. Scott, and A. P. Turner, "Ferrocene-mediated enzyme electrode for amperometric determination of glucose.," Anal. Chem. **56**, 667–71 (1984).

165. S. Ferri, K. Kojima, and K. Sode, "Review of glucose oxidases and glucose dehydrogenases: a bird's eye view of glucose sensing enzymes.," J. Diabetes Sci. Technol. **5**, 1068–76 (2011).

166. B. H. Ginsberg, "Factors affecting blood glucose monitoring: sources of errors in measurement.," J. Diabetes Sci. Technol. **3**, 903–13 (2009).

167. S. Vaddiraju, D. J. Burgess, I. Tomazos, F. C. Jain, and F. Papadimitrakopoulos, "Technologies for continuous glucose monitoring: current problems and future promises.," J. Diabetes Sci. Technol. **4**, 1540–62 (2010).

168. H. Heise, A. Bittner, and R. Marbach, "Clinical chemistry and near infrared spectroscopy: technology for non-invasive glucose monitoring," J. Near Infrared Spectrosc. **6**, 349 (1998).

169. H. M. Heise and R. Marbach, "Human oral mucosa studies with varying blood glucose concentration by non-invasive ATR-FT-IR-spectroscopy.," Cell. Mol. Biol. (Noisy-le-grand). **44**, 899–912 (1998).

170. M. A. Arnold and G. W. Small, "Noninvasive glucose sensing.," Anal. Chem. **77**, 5429–39 (2005).

171. A. P. M. Michel, S. Liakat, K. Bors, and C. F. Gmachl, "In vivo measurement of mid-infrared light scattering from human skin.," Biomed. Opt. Express **4**, 520–30 (2013).

172. A. C. Tam, "Applications of photoacoustic sensing techniques," Rev. Mod. Phys. **58**, 381–431 (1986).

173. H. von Lilienfeld-Toal, M. Weidenmüller, A. Xhelaj, and W. Mäntele, "A novel approach to non-invasive glucose measurement by mid-infrared spectroscopy: The combination of quantum cascade lasers (QCL) and photoacoustic detection," Vib. Spectrosc. **38**, 209–215 (2005).

174. J. Kottmann, J. M. Rey, J. Luginbühl, E. Reichmann, and M. W. Sigrist, "Glucose sensing in human epidermis using mid-infrared photoacoustic detection," Biomed. Opt. Express **3**, 667 (2012).

175. M. A. Pleitez, T. Lieblein, A. Bauer, O. Hertzberg, H. von Lilienfeld-Toal, and W. Mäntele, "In vivo noninvasive monitoring of glucose concentration in human epidermis by mid-infrared pulsed photoacoustic spectroscopy.," Anal. Chem. **85**, 1013–20 (2013).

176. J. C. Pickup, F. Hussain, N. D. Evans, O. J. Rolinski, and D. J. S. Birch, "Fluorescence-based glucose sensors.," Biosens. Bioelectron. **20**, 2555–65 (2005).

177. Y. J. Heo, H. Shibata, T. Okitsu, T. Kawanishi, and S. Takeuchi, "Long-term in vivo glucose monitoring using fluorescent hydrogel fibers.," Proc. Natl. Acad. Sci. U. S. A. **108**, 13399–403 (2011).

178. B. H. Malik and G. L. Coté, "Real-time, closed-loop dual-wavelength optical polarimetry for glucose monitoring.," J. Biomed. Opt. **15**, 017002 (2010).

179. R. O. Esenaliev, K. V Larin, I. V Larina, and M. Motamedi, "Noninvasive monitoring of glucose concentration with optical coherence tomography.," Opt. Lett. **26**, 992–4 (2001).

180. V. V Sapozhnikova, D. Prough, R. V Kuranov, I. Cicenaite, and R. O. Esenaliev, "Influence of osmolytes on in vivo glucose monitoring using

optical coherence tomography.," Exp. Biol. Med. (Maywood). **231**, 1323–32 (2006).

181. A. M. K. Enejder, T. G. Scecina, J. Oh, M. Hunter, W.-C. Shih, S. Sasic, G. L. Horowitz, and M. S. Feld, "Raman spectroscopy for noninvasive glucose measurements.," J. Biomed. Opt. **10**, 031114.

182. C.-F. So, K.-S. Choi, T. K. Wong, and J. W. Chung, "Recent advances in noninvasive glucose monitoring.," Med. Devices. **5**, 45–52 (2012).

183. E. Topsakal, T. Karacolak, and E. C. Moreland, "Glucose-dependent dielectric properties of blood plasma," in *2011 XXXth URSI General Assembly and Scientific Symposium* (IEEE, 2011), pp. 1–4.

184. P. H. Siegel, Y. Lee, and V. Pikov, "Millimeter-wave non-invasive monitoring of glucose in anesthetized rats," in *2014 39th International Conference on Infrared, Millimeter, and Terahertz Waves (IRMMW-THz)* (IEEE, 2014), pp. 1–2.

185. S. R. Arridge and W. R. B. Lionheart, "Nonuniqueness in diffusion-based optical tomography," Opt. Lett. **23**, 882 (1998).

186. A. Corlu, T. Durduran, R. Choe, M. Schweiger, E. M. C. Hillman, S. R. Arridge, and A. G. Yodh, "Uniqueness and wavelength optimization in continuous-wave multispectral diffuse optical tomography.," Opt. Lett. **28**, 2339–41 (2003).

187. A. Corlu, R. Choe, T. Durduran, K. Lee, M. Schweiger, S. R. Arridge, E. M. C. Hillman, and A. G. Yodh, "Diffuse optical tomography with spectral constraints and wavelength optimization," Appl. Opt. **44**, 2082 (2005).

188. S. Takano and E. Okada, "Analysis of the diffuse reflectance spectra of skin due to detection system," in *Proceedings of SPIE-OSA Biomedical Optics (Optical Society of America, 2011)* (2011), Vol. 8088, p. 80881A.

189. N. Rajaram, T. H. Nguyen, and J. W. Tunnell, "Lookup table–based inverse model for determining optical properties of turbid media," J. Biomed. Opt. **13**, 050501 (2008).

190. B. S. Nichols, "Performance of a lookup table-based approach for measuring tissue optical properties with diffuse optical spectroscopy," J. Biomed. Opt. **17**, 057001 (2012).